Study of Isotope Production in Proton- and Deuteron-Induced Spallation Reactions on 93Nb and 93Zr

中野, 敬太

https://doi.org/10.15017/4060208

Study of Isotope Production in Proton- and Deuteron-Induced Spallation Reactions on ^{93}Nb and ^{93}Zr

Keita Nakano
Department of Advanced Energy Engineering Science
Interdisciplinary Graduate School of Engineering Sciences
Kyushu University

February 2020

Abstract

This thesis has three purposes: one is to investigate the target nucleus dependence of isotope-production cross sections by measuring isotope-production cross section for ^{93}Nb in p-, d-, and C-induced reactions at 113 MeV/nucleon, another is to investigate the energy dependence of isotope-production cross sections by measuring new isotope-production cross section for the long-lived fission product, ^{93}Zr, in p- and d-induced reactions at 50 MeV/nucleon, and the other is to perform benchmark tests of the latest theoretical models and of the evaluated nuclear data libraries using these two and previously measured data.

The measurement of the isotope-production cross section for ^{93}Nb in p-, d-, and C-induced reactions at 113 MeV/nucleon was performed at RIKEN RI Beam Factory using the inverse-kinematics method with the ^{93}Nb secondary beam and the secondary targets, CH_2, CD_2, and C. Particle identifications of the secondary beam and the reaction product were performed via the TOF$-B\rho-\Delta E$ method to derive the isotope-production cross sections. The measured cross sections for ^{90}Mo, ^{90}Nb, $^{88.86}$Y produced by p-induced reactions were found to be consistent with those measured by the conventional activation method. We performed benchmark tests of the reaction models INCL4.6, JQMD, and JQMD-2.0 implemented in the PHITS, of CCONE code, and of the nuclear data libraries JENDL-4.0/HE, JENDL/ImPACT-2018, TENDL-2017, and ENDF/B-VIII.0. The model calculations showed generally good agreement with the measured isotope-production cross sections for p-, d-, and C-induced reactions. It also turns out that, among the four nuclear data libraries, JENDL-4.0/HE provides the best agreement with the measured data for the p-induced reactions. We compared with the present ^{93}Nb data with the ^{93}Zr data, that were measured previously by the same inverse-kinematics method, with particular attention to the effect of neutron-shell closure on isotope production in p- and d-induced spallation reactions. The isotopic distributions of the measured production cross sections in the ^{93}Zr data showed noticeable jumps at neutron number $N = 50$ in the isotopic chains of $\Delta Z = 0$ and -1, whereas no such jump appeared in isotopic chain of $\Delta Z = 0$ in the ^{93}Nb data. From INCL4.6/GEM calculations, we found that the jump formed in the evaporation process is smeared out by the intranuclear cascade component in ^{91}Nb produced by the ^{93}Nb$(p, p2n)$ and $(d, d2n)$ reactions on ^{93}Nb. Moreover, for ^{93}Nb, the distribution of the element-production cross sections as a function of the change in proton number ΔZ is shifted to smaller ΔZ than for ^{93}Zr, because the excited Nb pre-fragments generated by the cascade process are more likely to emit protons than the excited Zr pre-fragments, due to the smaller proton-separation energies of the Nb isotopes.

The measurement of the isotope-production cross section for ^{93}Zr in p- and d-induced reactions at 50 MeV/nucleon was performed at RIKEN RI Beam Factory using the inverse-kinematics method with the ^{93}Zr secondary beam and the secondary targets, cooled gaseous H_2 and D_2. Particle identifications of the secondary beam and the reaction product were performed via the TOF$-B\rho-\Delta E$ method to derive the isotope-production cross sections. From the comparison among the measured ^{93}Zr data at 50, 105, and 209 MeV/nucleon, the broader distributions of isotope-production cross sections were seen in the higher kinetic-energy cases. Categorization of the experimental ^{93}Zr data reveals that the total incident energy of around 200 MeV can be the best choice to reduce the long-lived products for nuclear transmutation of ^{93}Zr between 50- and 200-MeV/nucleon energy range. The model calculations using INCL4.6/GEM implemented in PHITS and INCL++/ABLA07 showed overall agreement with the measured data for p- and d-induced reactions. In the PHITS calculation, however, several discrepancies were still seen as in the p- and d-induced reactions at 105 and 209 MeV/nucleon. Finally, model analysis with the INCL++/ABLA07 and INCL++/GEM was performed in order to investigate the cause of underestimation seen in the neutron-deficient region of odd-atomic number isotopes. The model analysis reveals that the reexamination of level density used in GEM is required to improve underestimation seen in the production cross sections calculated by PHITS.

Contents

List of Figures

List of Tables

1 Introduction

1.1 High-Level Radioactive Waste

Treatment of high-level radioactive waste (HLW) is a crucial issue facing nuclear-energy development. The operation of nuclear power plants produces large amounts of spent fuels (an estimated 15,260 tons stored in domestic plants alone as of September 2018 [1]). The spent fuels are stored and isolated from living areas until the radioactivity decays; then, they will be melted with nitric acid and separated into uranium, plutonium, and other ingredients during reprocessing at the Rokkasho Nuclear Fuel Reprocessing Facility, which has an annual capacity of 800 tons of spent fuels. After reprocessing, the remaining radioactive isotopes will be vitrified as HLW. In Japan, it has been decided that the vitrified HLW will be disposed of in a stable rock formation more than 300 meters underground. However, geological disposal has stagnated due to long-term radiotoxicity.

Radioactive isotopes contained in spent fuel can be categorized into two types: Minor Actinoids (MAs), which are produced by several β decay processes after neutron capture by uranium, and Fission Products (FPs), which are produced by the fission of nuclear fuels and sequential decays of fission fragments. FPs having half-lives longer than 100,000 years (*e.g.*, ^{79}Se, ^{93}Zr, ^{99}Tc, ^{107}Pd, ^{129}I, and ^{135}Cs) are called as long-lived fission products (LLFPs). These are listed in Table. 1.1, together with their half-lives, neutron capture cross sections σ_n [2], and concentrations per ton of spent fuel [3]. Figures 1.1 and 1.2 show the time dependence of the potential radiotoxicity of isotopes included in the spent fuel; it is apparent that continuous risks of radiotoxicity exist for more than one thousand years for MAs and for more than one million years for LLFPs. As mentioned above, this fact can be a major obstacles to the progress of geological disposal.

1.2 Nuclear Transmutation

Nuclear transmutation has received much attention as a possible method of shortening the effective half-lives of LLFPs and of reducing their amounts by con-

Table 1.1: List of isotopes included in spent fuel from PWR (burnup: 45 GWd/tHM) [2, 3].

Nuclide			half-life [y]	σ_n [barns]	amount [g/1tHM]
MA		^{237}Np	2.4×10^6	-	633
		^{241}Am	4.3×10^2		411
		^{243}Am	7.4×10^3		171
FP	LLFP	^{99}Tc	2.1×10^5	23.68	1052
		^{129}I	1.6×10^7	30.33	242
		^{79}Se	3.0×10^5	50.04	6
		^{93}Zr	1.5×10^6	2.24	958
		^{107}Pd	6.5×10^6	9.192	312
		^{126}Sn	2.3×10^5	0.09	31
		^{135}Cs	2.3×10^6	8.304	522
		^{90}Sr	29	0.01	635
		^{137}Cs	30	0.27	1488

verting them into short-lived and/or stable nuclei. Nuclear transmutation refers to the transformation of one nuclide into another, for example, ^{93}Zr (half-life: 1.5×10^6 years) can be transmuted into ^{92}Y (half-life: 3.5 hours) via an (n, pn) reaction. ^{92}Y then transforms into ^{92}Zr (a stable nucleus) via β decay. Another example is the transmutation of ^{107}Pd (half-life: 6.5×10^6 years) into ^{108}Pd (a stable nucleus) via neutron capture (n, γ). Stable palladium isotopes are minor metals for use in catalytic converters, fuel cells, and electronics. From these examples, nuclear transmutation is able to not only reduce half-lives and radiotoxicity, but also to recycle minor metals.

Since MAs have relatively large dose conversion factors and can be used as nuclear fuel owing to their fissionable nature, nuclear-transmutation technologies for MAs with next-generation reactors have been well-studied. Moreover, nuclear transmutation of ^{99}Tc and ^{129}I via the next-generation reactors has been proposed because they both have large σ_n as shown in Table. 1.1. Here several proposed methods for nuclear transmutation of MAs, ^{99}Tc, and ^{129}I are introduced. The first is an accelerator-driven sub-critical system (ADS), which is a combination of an accelerator and a reactor core [4, 5]. The sub-critical system is kept by the fission neutrons from the MAs surrounding a spallation target and by spallation neutrons. The spallation neutrons are generated by proton-induced reactions in the spallation target by using accelerated proton ranging from several hundred MeV to several GeV. A highly safe system can be achieved because ADS stops as soon as the proton beam does. Fast reactors are another candidate, since they can induce nuclear fission via fast neutrons [6]. This method is proceeded with

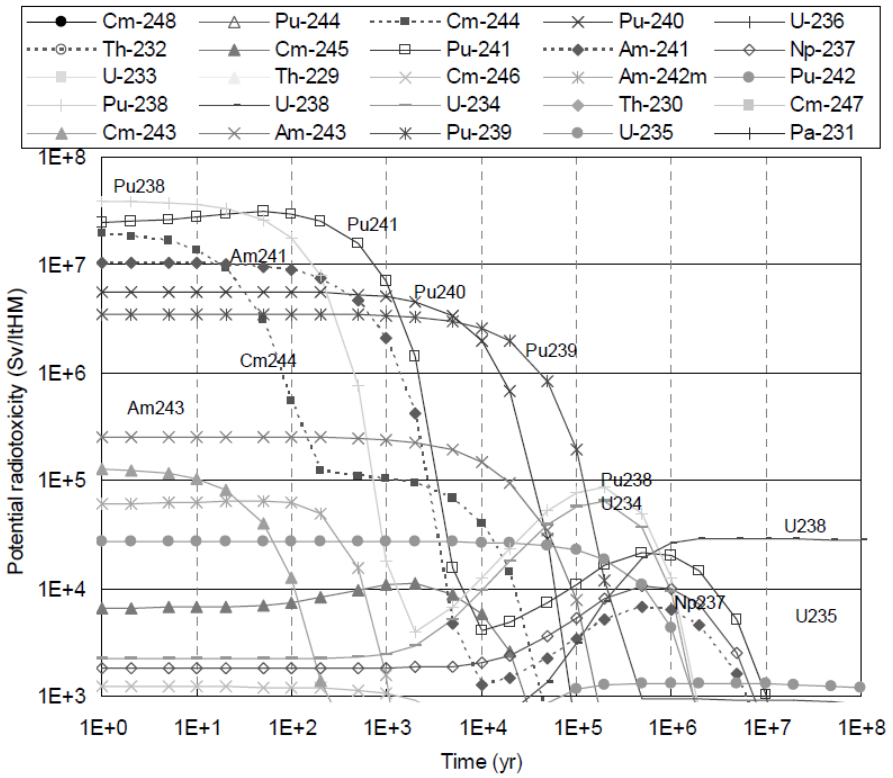

Figure 1.1: Time dependence of potential radiotoxicity of MAs included in spent fuel generated in PWR (burnup: 45 GWd/tHM, after 5 years' cooling); cited from Ref. [3].

concept review without large effect on core characteristics.

While several studies on the nuclear transmutation of FPs and LLFPs have been conducted [7, 8], no method has yet been established owing to difficulties in measuring the fundamental nuclear data of FPs and LLFPs. It should be emphasized that LLFPs are also generated in the nuclear transmutation processes of MAs.

1.3 ImPACT Program

A study on reduction and resource recycling of high-level radioactive wastes through nuclear transmutation has been conducted [9] as part of Impulsing Paradigm Change through Disruptive Technologies (ImPACT) Program. The goal of this program is to investigate the optimum nuclear-reaction paths for five LLFPs (^{79}Se, ^{93}Zr, ^{107}Pd, ^{126}Sn, and ^{135}Cs), for which there have been no options except geological disposal. Another aim of this program is to develop ecological systems for the

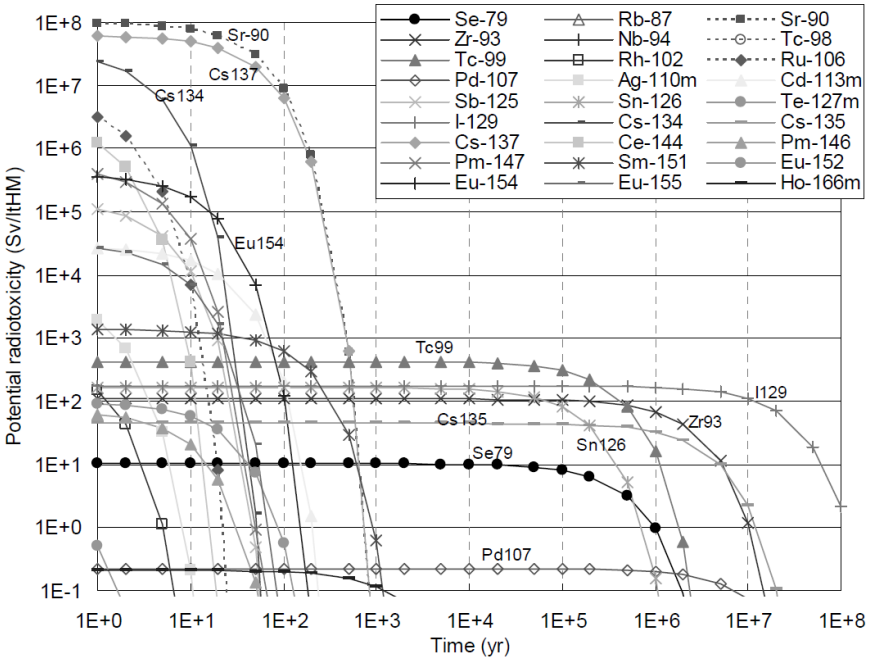

Figure 1.2: Same as Fig. 1.1, but for FPs cited from Ref. [3].

reuse of minor metals and other resources included in the recovered products. This program consists of five projects: (1) study of technologies for separating LLFPs from radioactive liquid waste; (2) measurement of fundamental nuclear data and demonstration experiments of nuclear transmutation; (3) improvement of theoretical models using the measured data; (4) development of nuclear-transmutation system and elemental technologies such as accelerators; and (5) proposal of a nuclear-transmutation concept. As a part of the project (2), we measured the fundamental nuclear data of LLFPs in various nuclear reactions such as neutron capture reaction, muon-induced reaction, and spallation reactions.

1.4 Spallation Reaction

We focus upon the spallation reactions induced by high-energy light particles such as neutrons, protons, and deuterons with accelerators as a possible candidate for the nuclear transmutation of LLFPs, due to their relatively small σ_n as shown in Table. 1.1. Study of spallation reactions is particularly significant for the nuclear transmutation of ^{93}Zr, which has a small σ_n of 2.24 barns, regardless of the large amount of 958 g/1tHM in spent fuel. In this section, a brief explanation of the spallation reaction, nuclear-data-measurement techniques of spallation reaction,

and a discussion of previous related works are presented.

1.4.1 Characteristics of Spallation Reactions

Spallation reactions refer to nuclear reactions with several secondary-particle emissions. In general, such reactions are induced by relatively high-energy particles ranging from several tens of MeV to several GeV. Spallation reactions play key roles in fields of various applications, *e.g.*, radioactive-isotope (RI) beam production [10], ADS [4, 5], and spallation-neutron sources for material science [11]. Nuclear transmutation with accelerators is a possible use of spallation reactions. Over the past few decades, numerous studies have been devoted to such reactions in an effort to understand their mechanisms and to accumulate fundamental data for such applications. The study of spallation reactions thus remains of interest from the viewpoint of fundamental physics, as well as that of applications. To understand the mechanisms, the energy spectra of emitted particles and the isotopic distributions of the remnant after the reaction are key factors. In particular, the isotope-production cross sections play a key role in the study of the optimum reaction pathway for nuclear transmutation, because the half-life distribution of the reaction products can be deduced from the isotopic distribution. More stable isotopes and less long-lived residues are ideal for the transmutation process.

1.4.2 Measurement Technique: Activation and Inverse-Kinematics Methods

The activation method is conventionally used for measurements of isotope-production cross sections. After irradiation of a target material, one can estimate the production yields of residual nuclei produced in reactions by measuring the unique γ rays that they emit. However, the production yields of stable nuclei, which play an important role in the design of nuclear-transmutation system, cannot be measured in principle. In addition, in the case of LLFPs, it may be difficult to fabricate and handle radioactive targets. Recently, the inverse-kinematics method has been used as a new measurement technique for nuclear reactions [12, 13]. In the inverse-kinematics method, the target nucleus and the incident particle are interchanged, that is, a heavy ion irradiates a light isotope such as hydrogen or deuterium. The nuclear reactions in both the inverse and direct kinematics can be assumed to be the same. Using the inverse-kinematics method, one can measure the production yields of residual nuclei over wide ranges of atomic and mass numbers, including stable nuclei, because residual nuclei are emitted in a forward direction and their yields can be measured directly using a magnetic spectrometer. An additional advantage of the inverse-kinematics method is that the manufacture of targets made

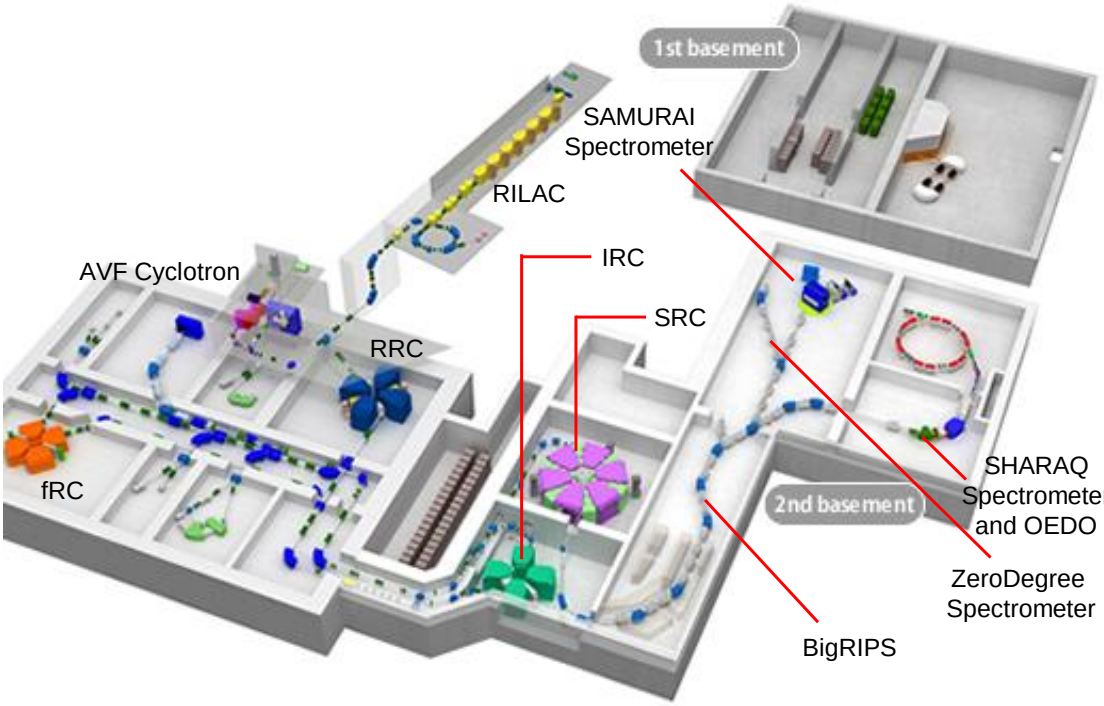

Figure 1.3: Overhead view of the RIKEN Radioactive Isotope Beam Factory (RIBF), excerpted from Ref. [18].

of rare isotopes like LLFPs is not necessary.

To measure the LLFP nuclear data using the inverse-kinematics method, an energetic beam of LLFPs is necessary instead of a radioactive target. Such an LLFP beam is available in the RIKEN Radioactive Isotope Beam Factory (RIBF). Since 2008, RIBF has provided beams of all elements up to uranium, including radioactive isotopes thanks to the progress of accelerating technology. The RIKEN RIBF consists of several accelerators (RILAC, AVF Cyclotron, RRC, fRC, IRC, and SRC), a superconducting radioactive-isotope-beam separator (BigRIPS) [14], and several spectrometers (ZeroDegree Spectrometer [14], SAMURAI Spectrometer [15], and SHARAQ Spectrometer [16] and OEDO [17]), as shown in Fig. 1.3. An accelerated primary beam such as ^{238}U or ^{136}Xe is used to bombard a primary target to generate a secondary cocktail beam via in-flight fission and/or spallation reactions. The isotopes targeted by researchers are separated and identified at BigRIPS for study of their properties. Using this beam production process, a secondary beam of unstable isotopes like LLFPs is available at RIKEN RIBF.

1.4.3 Previous Works

Numerous works on spallation reactions by measuring isotope-production cross sections have been conducted for ^{208}Pb [19, 20] using the activation method and for ^{48}Ca [12], ^{56}Fe [21–23], ^{136}Xe [24–27], ^{197}Au [28–31], ^{208}Pb [32–36], and ^{238}U [37–42] using the inverse-kinematics method. Recently, studies of spallation reactions on FPs (^{90}Sr + p, d at 185 MeV/nucleon [43] and ^{137}Cs + p, d at 185 MeV/nucleon [43]) and LLFPs (^{93}Zr + p, d at 105 [44] and 209 MeV/nucleon [45] and ^{107}Pd + p, d at 50 [46], 118, and 196 MeV/nucleon [47]) have been also conducted at RIKEN RIBF using the inverse-kinematics method as a part of ImPACT Program. In these works [43–45, 47], benchmark tests of the theoretical models implemented in the Particle and Heavy Ion Transport code System (PHITS) [48, 49] have been performed. The PHITS calculations show generally good agreement with the measured data for FPs and LLFPs; however, several discrepancies are pointed out. To confirm these discrepancies and extract insight to improve the reaction models, further systematic measurements of isotope-production cross sections over a wide energy range for various target isotopes are strongly required. In addition to the theoretical models, similar benchmark tests of evaluated nuclear data libraries such as JENDL-4.0/HE [50], TENDL-2017 [51], and ENDF/B-VIII.0 [52] are necessary for the design of various applications.

1.5 Objectives

Taking into consideration these circumstances, it is necessary to systematically accumulate more fundamental nuclear data for the design of nuclear-transmutation system, for a deeper understanding of spallation-reaction mechanisms, and to improve theoretical models and evaluated nuclear data libraries. The purposes of this work are therefore as follows:

- To investigate the target nucleus dependence of isotope-production cross sections by measuring isotope-production cross section for ^{93}Nb in p-, d-, and C-induced reactions at 113 MeV/nucleon.
- To investigate the energy dependence of isotope-production cross sections by measuring new isotope-production cross section for the LLFP ^{93}Zr in p- and d-induced reactions at 50 MeV/nucleon.
- To benchmark the latest theoretical models and the evaluated nuclear data libraries using the above-mentioned measured data.

Comparison of the isotope-production cross section between the newly measured ^{93}Nb + p, d reaction at 113 MeV/nucleon and the previously measured ^{93}Zr + p, d

reaction at 105 MeV/nucleon provides information concerning how differences in initial proton and neutron numbers affect the isotopic distributions of production cross sections. As for the second objective, intercomparison among the ^{93}Zr + p, d reactions at 50, 105, and 209 MeV/nucleon yields the energy dependence of the isotopic distribution of the production cross sections. Also, the data for ^{93}Zr can be used to discuss the optimal incident energy in nuclear transmutation from a fundamental-data point of view. In addition, these data are useful for benchmark tests of the theoretical models and the evaluated nuclear data. In particular, ^{93}Nb data enable us to benchmark the evaluated nuclear data libraries because ^{93}Nb is a stable isotope and many libraries store its data. These benchmarks provide many feed-backs and fundamental knowledge to the models and the libraries. This work may contribute to a spallation study in a relatively low energy range compared to the previous works [19–30, 32–42] as well as to a systematic transmutation study of ^{93}Zr.

This thesis is composed of four parts including this introduction. Chapter 2 is devoted to work on the ^{93}Nb + p, d, and C reactions at 113 MeV/nucleon. In Chapter 3, a study on ^{93}Zr + p and d at 50 MeV/nucleon is described, including a systematic analysis of ^{93}Zr data for the incident energy. Finally, the summary and conclusions are presented in Chapter 4.

2 Isotope Production in Proton-, Deuteron-, and Carbon-Induced Reactions on ^{93}Nb at 113 MeV/Nucleon

2.1 Introduction

As mentioned in Chapter 1, isotope-production cross sections in p- and d-induced reactions on ^{93}Zr at 105 MeV/nucleon [44] and ^{107}Pd at 118 MeV/nucleon [47] were measured using the inverse-kinematics method at the RIKEN RIBF in order to accumulate the basic data necessary for nuclear-waste transmutation as part of the ImPACT Program. Comparisons among the measured ^{93}Zr and ^{107}Pd data show noticeable jumps in the ^{93}Zr data for isotopic distributions of the measured cross sections for the production of Zr and Y chains due to the shell effect at a neutron magic number of $N = 50$. This experimental result suggests the importance of shell closure in the description of p- and d-induced spallation reactions on target nuclei near this magic number. It is worth emphasizing that the production cross sections for stable residual nuclei such as $^{90.91.92}$Zr in the isotopic chain of Zr cannot be measured by a conventional activation method. The inverse-kinematics method thus has great advantages for systematic measurements of the isotopic distributions of the production cross sections. Similar experimental data for nuclei adjacent to ^{93}Zr are required to confirm the effects of neutron-shell closure at $N = 50$ upon isotope production in p- and d-induced spallation reactions.

In the ^{93}Zr experiment, ^{93}Nb, one of the isobars with $A = 93$, was included in the secondary beam produced by the in-flight fission of ^{238}U at 345 MeV/nucleon due to interaction with a beryllium target. The proton and neutron numbers in ^{93}Nb are $Z = 41$ and $N = 52$, respectively, whereas they are $Z = 40$ and $N = 53$ in ^{93}Zr. It is interesting to see how the difference of a single nucleon in the initial proton and neutron numbers influences the isotopic distribution of the measured production cross sections. In addition, there is much experimental data related to isotope-production cross sections from the conventional activation method, because ^{93}Nb is a stable nucleus that comprises 100% of the natural niobium abundance, and nuclear data libraries up to 200 MeV are also available.

Thus, new data for ^{93}Nb provide useful checks on the consistency between the isotope-production data measured by the two difference methods. Moreover, the ^{93}Nb data can contribute to validation of the nuclear data libraries and of the reaction models used in the work on ^{93}Zr, namely, the Liége Intranuclear Cascade model version 4.6 (INCL4.6) [53] and the Generalized Evaporation Model (GEM) [54] employed in the Particle and Heavy Ion Transport code System (PHITS) [48, 49], as well as the CCONE code [55]. Moreover, isotope-production cross sections can be extracted for the ^{93}Nb + C reaction because carbon was used as a reaction target in the inverse-kinematics experiment. New data on the ^{93}Nb + C reaction can be used to benchmark the JAERI Quantum Molecular Dynamics code (JQMD) [56] implemented in PHITS, which is employed to describe the fragmentation reactions induced by heavy ions. These models and nuclear data libraries are introduced in Appendix A.

2.2 Experiment

The experiment was carried out at the RIKEN Radioactive Isotope Beam Factory (RIBF) using a cocktail beam including ^{93}Nb and ^{93}Zr secondary beams with kinetic energies of 113 and 105 MeV/nucleon, respectively. The BigRIPS RI beam separator [14] and the ZeroDegree Spectrometer (ZDS) [14] were also used in this experiment. A ^{238}U primary beam was accelerated up to 345 MeV/nucleon and used to impinge upon a 3-mm-thick ^{9}Be primary target installed at the entrance of BigRIPS. RILAC, RRC, fRC, IRC, and SRC were used to accelerate the ^{238}U primary beam. The secondary beam containing ^{93}Nb and ^{93}Zr ions was produced through in-flight fission of the ^{238}U primary beam, and then separated and identified using BigRIPS. Then, the secondary beam impinged onto the secondary targets CH_2, CD_2, and C located at the entrance of the ZDS. The residual nuclei produced by nuclear reactions with the secondary targets were also identified at ZDS in order to derive the isotope-production cross section. In this section, the basic setups of BigRIPS and ZDS, the beamline detectors, secondary targets, and the DAQ system are introduced.

2.2.1 Basic Setup and Experimental Procedure

BigRIPS and the ZDS were respectively used to analyze the incident ^{93}Nb beam and the reaction products in the present experiment. A schematic view of the beamline is presented in Fig. 2.1. BigRIPS and ZDS comprise superconducting triplet-quadrupole (STQ) magnets and dipole (D) magnets indicated by yellow and blue blocks in Fig. 2.1, respectively. Focal planes are indicated by the symbol F in which slits, degraders, beamline detectors, and targets are placed. BigRIPS

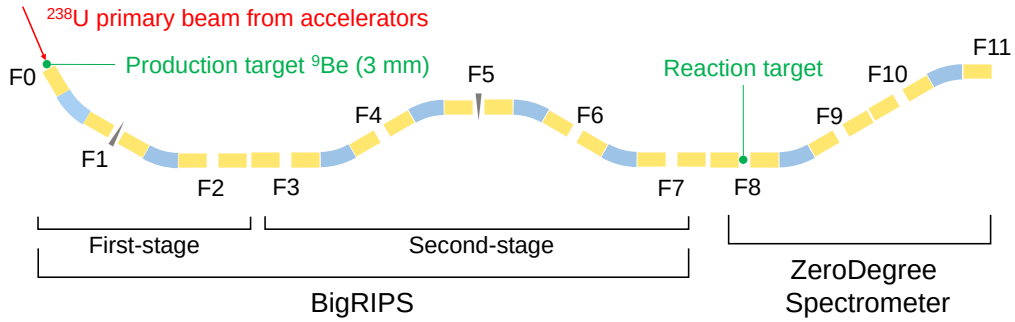

Figure 2.1: Schematic view of the BigRIPS and ZeroDegree Spectrometer used in the present experiment.

Table 2.1: Magnetic fields at each section of BigRIPS for ^{93}Zr.

Section	$B\rho$ [Tm]
F0 - F1	5.9500
F1 - F3	5.0102
F3 - F5	4.9767
F5 - F7	4.0256

has a two-stage structure: secondary beams are produced and separated in the first stage and particle identification is performed in the second stage.

Separation of the secondary beam was performed using D magnets and slits equipped at some focal planes. The secondary beams with a certain magnetic rigidity $B\rho$ were extracted by adjusting the slit aperture and the magnetic fields of the D magnets according to the following equation:

$$B\rho \propto \frac{A}{Q}\beta\gamma, \tag{2.1}$$

where A/Q is the mass-to-charge ratio of the beam nucleus, β is the relative velocity of the beam, γ is the Lorenz factor, B is the magnetic field of the D magnet, and ρ is the magnet's radius of curvature. The magnetic fields of the D magnets and the apertures of the slits were optimized for the production of ^{93}Zr, as listed in Tables. 2.1 and 2.2, respectively. In addition, the secondary beam was purified using wedge-shaped alminum energy degraders, as listed in Table. 2.2. The secondary beam lost its kinetic energy through penetration of the energy degraders. This loss depends on the horizontal positions, the atomic number Z, and β of the incident secondary beam. By being injected into another D magnet again, the beam was bent and the position downstream of the magnet depends on Z and β of the secondary beam. Thus, the secondary beam was separated by its

Table 2.2: Apertures of slits and geometries of degraders.

Focal plane	Slit [mm]	Degrader [mm, mrad]
F1	L: −1.00, R: 1.00	thickness: 5, angle: 5.986
F2	L: −10.00, R: 10.00	-
F5	L: −30.00, R: 30.00	thickness: 3.5, angle: 4.20
F7	L: −6.00, R: 6.00	-

Table 2.3: Magnetic fields at each section of ZeroDegree Spectrometer.

Reaction target	Section	$B\rho$ [Tm]				
		+3%	0%	−3%	−6%	−9%
CH_2, CD_2, C	F8 - F9	3.3943	3.2638	3.1965	3.0977	2.9988
	F9 - F11	3.3662	3.2348	3.1701	3.0721	2.9741
Empty	F8 - F9	3.7925	3.6938	3.5967	3.4988	3.4009
	F9 - F11	3.7588	3.6618	3.5647	3.4677	3.3707

Z and β using the slits.

Since F1 is the momentum-dispersive focus, at which the horizontal position of the beam depends on its momentum, the momentum acceptance of BigRIPS was determined by the aperture of the slit at F1. An aperture of ±1 mm corresponds to momentum spread of ±0.1%.

After separation, particle identification was performed in the second stage of BigRIPS using signals from beamline detectors. Then the secondary beam impinged onto the secondary target at F8. The reaction products were analyzed using ZDS via a method similar to that employed in the second stage of BigRIPS. In this experiment, ZDS was operated with achromatic mode, where the intermediate focal plane (F9) is the dispersive focus and final focal plane (F11) is achromatic. In the achromatic mode, the momentum acceptance of ZDS is limited to less than ±3%. Five different magnetic-field settings $\Delta(B\rho)/B\rho = -9\%, -6\%, -3\%, 0\%,$ and +3% were adopted to measure the wide range of mass numbers of reaction products listed in Table. 2.3. The acceptances of the neighboring settings were overlapped to avoid losing events at the edge of the acceptance as explained in Sec. 2.3.3. Note that a $B\rho$ setting of 0% corresponds to the magnetic rigidity of the ^{93}Zr beam. The typical current of the primary beam was approximately 4 enA.

Table 2.4: Beamline detectors used for particle identification.

Focal plane	Detector
F3	Plastic scintillator, double-PPAC×2
F5	double-PPAC×2
F7	Plastic scintillator, double-PPAC×2, MUSIC
F8	Plastic scintillator, double-PPAC×2
F9	double-PPAC×2
F11	Plastic scintillator, double-PPAC×2, MUSIC

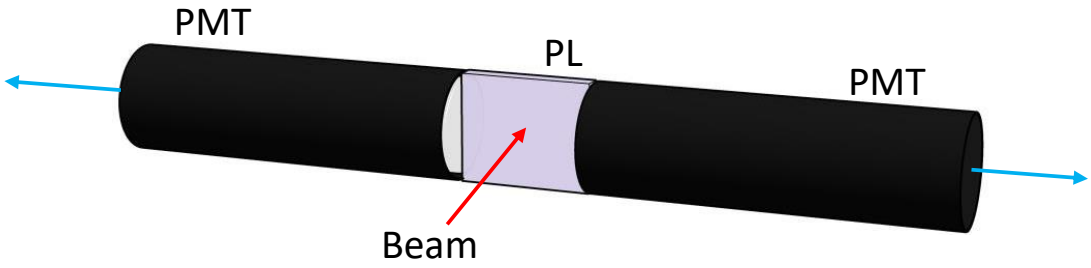

Figure 2.2: Schematic view of the plastic scintillator.

2.2.2 Beamline Detectors

In this experiment, plastic scintillators (PLs), double parallel-plate avalanche counters (double-PPACs) [57], and multisampling ionization chambers (MUSICs) [58] were used to identify the secondary beam and reaction products via the TOF$-B\rho-\Delta E$ method [59]. The detectors and their locations are summarized in Table 2.4. Here, the details of each detector and its configuration are introduced.

Plastic Scintillator

The plastic scintillators were installed at F3, F7, F8, and F11 to measure the time of flight (TOF). The plastic scintillators at F3 (F3PL) and F7 (F7PL) were combined to obtain the TOF for the secondary beam; on the other hand, F8PL and F11PL were combined to measure the TOF for the reaction products. A schematic view of the plate-shaped plastic scintillator used in the experiment is shown in Fig. 2.2. Two photomultiplier tubes (PMTs) were connected to both sides of the scintillators to determine the timing at which the beam passes through. The dimensions of the plastic scintillators are shown in Table 2.5. The signal from PMT was divided into two signals: one was fed into a charge ADC directly, the other into a constant fraction discriminator and transported to a TDC module.

Table 2.5: Dimensions of the plastic scintillators.

Focal plane	Thickness [mm]	Active area [mm^2]
F3	0.2	120(W) $\times$ 100(H)
F7	0.2	120(W) $\times$ 100(H)
F8	0.1	120(W) $\times$ 100(H)
F11	0.2	120(W) $\times$ 100(H)

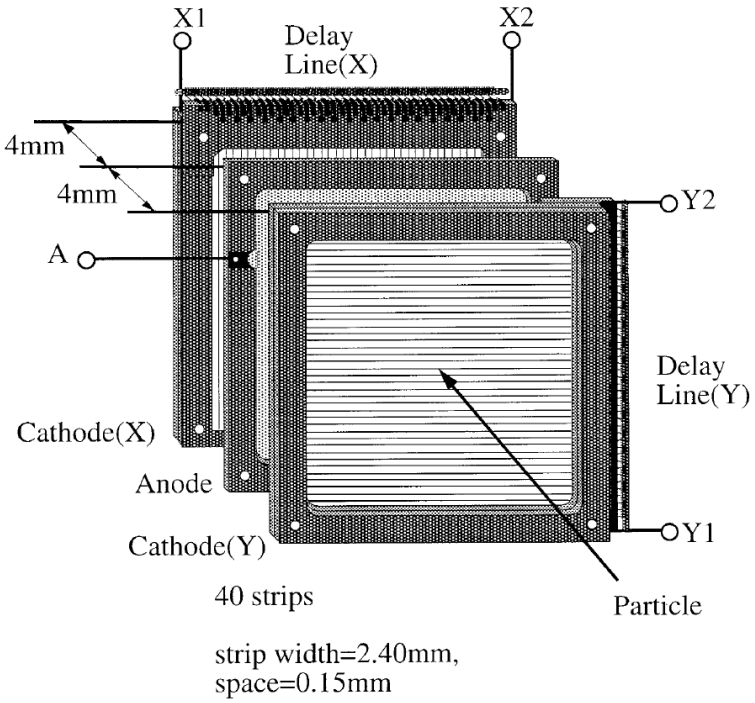

Figure 2.3: Schematic view of the PPAC, excerpted from Ref. [57].

Double-PPAC

The double-PPACs were installed at F3, F5, F7, F8, F9, and F11 for trajectory reconstruction of beam. The $B\rho$ value of the beam was deduced using the obtained trajectories, the $B\rho$ values of D magnets, and the transport matrix. A single-PPAC consists of an anode plate and two cathode plates located on both sides of the anode, as shown in Fig. 2.3 [57]. Each cathode plate has 2.40-mm-wide strips with 0.15-mm inner-strip spacing, connected to one another via a delay line. Two cathodes provide x and y positions, respectively, from the time differences of signals at both ends of the delay-lines. In the experiment, double-PPACs, each containing two single-PPACs in a box, were used to achieve high detection efficiency. In

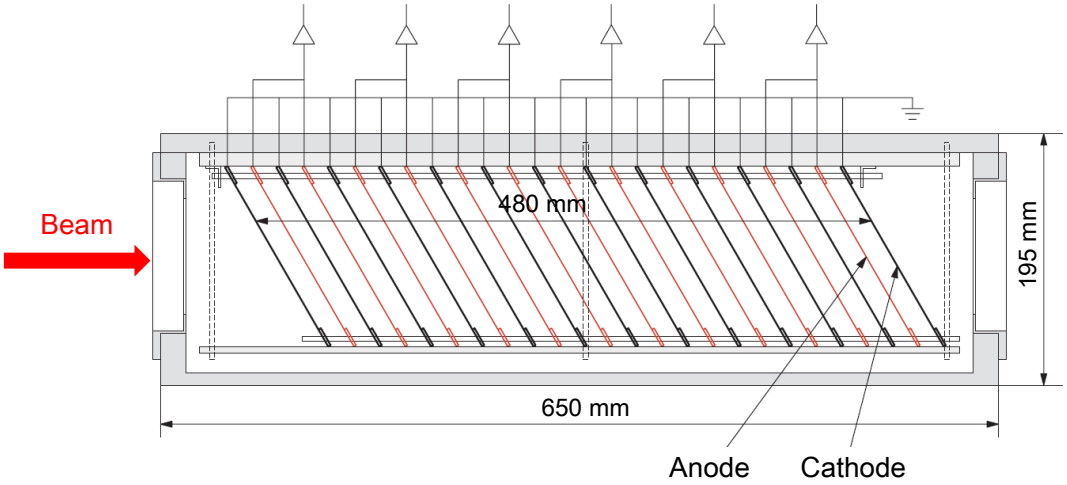

Figure 2.4: Schematic view of the MUSIC, excerpted from Ref. [58].

Table 2.6: Dimensions and geometries of the MUSICs.

Focal plane	Thickness [mm]	Aperture	Size
F7	586	Circle	232 mmϕ
F11	600	Rectangle	260(W) $\times$ 170(H) mm^2

addition, the tracks of the beams were determined using two double-PPACs at each focal plane. In the present experiment, PPACs were filled with C_3F_8 gas at a pressure of 30 Torr, and their active areas were 240(W)$\times$150(H) mm^2. The signals from the electrodes passed through a fast preamplifier. They were then amplified by a fast timing amplifier and sent to a constant fraction discriminator. Finally, the discriminated signals were transported to TDC.

Multisampling Ionization Chamber (MUSIC)

The MUSICs were installed at F7 and F11 to measure the energy loss ΔE. Each MUSIC used in the present experiment consists of 12 anode planes and 13 cathode planes with 20-mm inter-plane spacing, as shown in Fig. 2.4 [58]. They were filled with P10 gas (Ar(90%) + CH_4(10%)) at pressures of 650 Torr (F7) and 760 Torr (F11). Their active areas and geometries are given by Table 2.6. The MUSIC provided six signals that reflect the energy losses of particles in every two anodes. After passing through the preamplifier, the signals were sent to a spectroscopy amplifier, then to the charge ADC module.

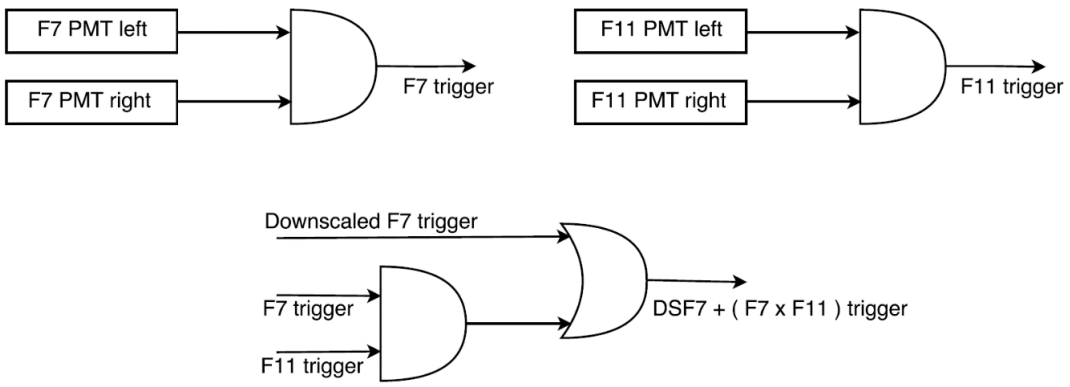

Figure 2.5: Logic circuits of triggers.

2.2.3 Secondary Targets

The secondary targets were placed at F8. In this experiment, CH_2 (179.2 mg/cm^2), CD_2 (217.8 mg/cm^2), and C (226.0 mg/cm^2) were used as secondary targets to measure the p- and d-induced reactions. The solid targets were selected because they are easy to handle. The contributions from carbon isotopes in CH_2 and CD_2 were subtracted by a carbon-target run. Their thicknesses were determined such that the energy losses of the secondary beams in each secondary target would be almost the same. An empty-frame run was also performed to subtract background events from beamline materials.

2.2.4 Trigger

In this subsection, the triggers for data acquisition are explained. These triggers were generated by a combination of signals from plastic scintillators. F7 trigger generated by the coincidence of signals from both sides of F7PL was used in the +3%, 0%, and −3% run cases. F11 trigger was also generated by the coincidence of signals from both sides of F11PL. In the −6% and −9% run cases, trigger was generated by taking the logical sum and product of the F7, F11, and 1/20-downscaled F7 (DSF7) triggers, as shown in Table 2.7. Since the incident ^{93}Nb beam without changing A and Z at the beamline materials including the secondary target does not reach to F11 in the −6% and −9% run cases, most of F7 triggered events have no signals from the detectors at the ZDS. By using sum of F7 and F11 triggers, only the events with signals from detectors at the ZDS can be extracted. In addition, DSF7 trigger was included in order to estimate the number of incident ^{93}Nb beam. Figure 2.5 shows the logic circuits of the triggers.

Table 2.7: List of triggers.

Trigger	$B\rho$ Setting
F7	+3%, 0%, −3%
DSF7 + (F7 × F11)	−6%, −9%

2.3 Data Analysis

Particle identification of the secondary beam and reaction products was performed based on the TOF$-B\rho-\Delta E$ method [59] with the following equations:

$$\mathrm{TOF} = \frac{L}{\beta c}, \tag{2.2}$$

$$\frac{A}{Q} = \frac{B\rho}{\beta\gamma}\frac{c}{m_u}, \tag{2.3}$$

$$\frac{dE}{dx} = \frac{4\pi e^4 Z^2}{m_e v^2} N z \left[\ln\frac{2m_e v^2}{I} - \ln(1-\beta^2) - \beta^2\right], \tag{2.4}$$

where L is the flight-path length, m_u the atomic mass unit, m_e the electron mass, e the electron charge, and c the velocity of light. The variable v is the velocity of the projectile in the secondary beam, and β and γ are the corresponding relativistic velocity and Lorentz factor, respectively. N, z, and I indicate the atomic density, atomic number, and mean excitation potential of the material, respectively. Additionally, some corrections to the yields of the reaction products were applied. This section focuses on analysis of the signals from the beamline detectors, the analytical procedure for particle identification, corrections to the yields, calculation of the production cross section, and uncertainty evaluation.

2.3.1 Data Analysis of Beamline Detectors

Plastic Scintillator

The plastic scintillators provided the charge output recorded by the ADC and the timing output recorded by the TDC. The charge information was used for validation of the plastic scintillator, while the timing information was used to calculate the TOF. For each plastic scintillator, two raw timing signals from the left ($T_{\mathrm{l,raw}}$) and right ($T_{\mathrm{r,raw}}$) PMTs were calibrated from the output channel to the actual timing information $T_{\mathrm{l,calib}}$ and $T_{\mathrm{r,calib}}$ using calibration parameters $c_{\mathrm{l,pla}}$

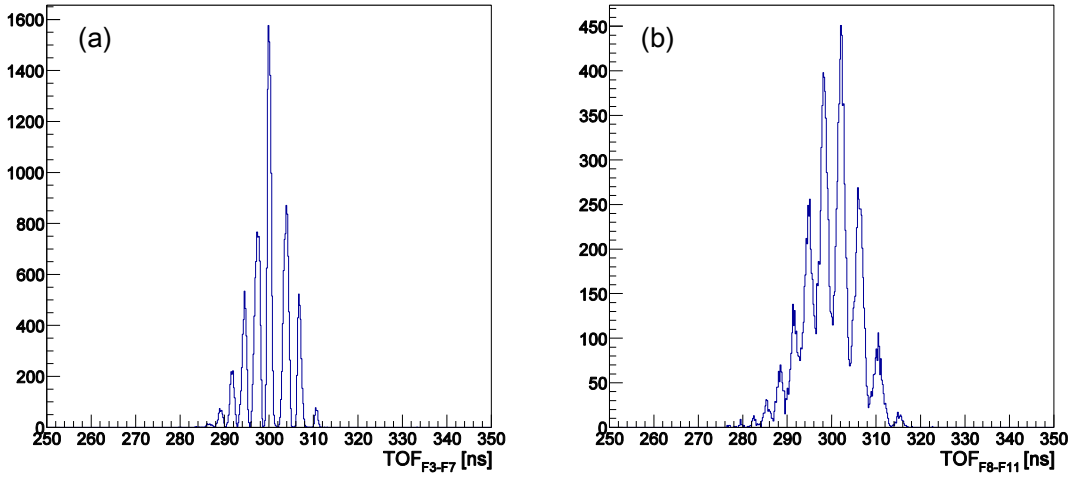

Figure 2.6: Distribution of the time-of-flight (TOF). Panels (a) and (b) respectively display the TOFs between F3 and F7 and between F8 and F11 in the CH_2 reaction target and the 0% ZDS $B\rho$ setting.

and $c_{\mathrm{r,pla}}$, respectively, and averaged as the timing at each plastic scintillator T_{pla} to cancel out the position dependence as follows:

$$T_{\mathrm{l,calib}} = c_{\mathrm{l,pla}} \times T_{\mathrm{l,raw}}, \tag{2.5}$$

$$T_{\mathrm{r,calib}} = c_{\mathrm{r,pla}} \times T_{\mathrm{r,raw}}, \tag{2.6}$$

$$T_{\mathrm{pla}} = \frac{T_{\mathrm{r,calib}} + T_{\mathrm{l,calib}}}{2}. \tag{2.7}$$

The calibration parameters were derived by a run with the TDC calibrator. The TOFs between F3 and F7 for the secondary beam ($\mathrm{TOF_{F3-F7}}$), and between F8 and F11 for the reaction products ($\mathrm{TOF_{F8-F11}}$), were calculated using the timing information for each focal plane $T_{\mathrm{F,pla}}$ as:

$$\mathrm{TOF_{F3-F7}} = T_{\mathrm{F7,pla}} - T_{\mathrm{F3,pla}} + \mathrm{offset_{F3-F7}}, \tag{2.8}$$

$$\mathrm{TOF_{F8-F11}} = T_{\mathrm{F11,pla}} - T_{\mathrm{F8,pla}} + \mathrm{offset_{F8-F11}}. \tag{2.9}$$

The parameters $\mathrm{offset_{F3-F7}}$ and $\mathrm{offset_{F8-F11}}$ were adjusted to make the TOFs equal to that calculated from the $B\rho$ value of the ^{93}Nb beam. Figure 2.6 shows $\mathrm{TOF_{F3-F7}}$ in panel (a) and $\mathrm{TOF_{F8-F11}}$ in panel (b). Some sharp peaks are seen in Fig. 2.6 (a), because the momenta of the secondary beams were limited by the aperture of the slit at F1, which is equivalent to $\pm 0.1\%$ of the momentum spread. Assuming that $B\rho$ is constant in Eq. (2.3), β and TOF depend on only A/Q. Thus, it is apparent that the peaks correspond to A/Q distribution. These peaks are smeared out due

to energy straggling and nuclear reaction in the beamline materials, as shown in Fig. 2.6 (b).

Double-PPAC

The PPACs provided the five timing signals from an anode and cathodes. The horizontal and vertical positions x_{PPAC} and y_{PPAC} at which the beam passed the PPAC were calculated by the time differences between the timing signals from the both sides of each cathode, as per the following equations:

$$x_{\mathrm{PPAC}} = c_{x,\mathrm{PPAC}} \times (T_{x1} - T_{x2} + \mathrm{offset}_{x1}) - \mathrm{offset}_{x2}, \tag{2.10}$$

$$y_{\mathrm{PPAC}} = c_{y,\mathrm{PPAC}} \times (T_{y1} - T_{y2} + \mathrm{offset}_{y1}) - \mathrm{offset}_{y2}, \tag{2.11}$$

where $c_{x,\mathrm{PPAC}}$ and $c_{y,\mathrm{PPAC}}$ are calibration parameters to convert the time difference into length. The offset_{x1} and offset_{y1} values were determined by the cable delays in the circuits. On the other hand, the offset_{x2} and offset_{y2} values correspond to geometrical offsets. Timing information converted from the output channel generated by the cathodes were defined as T_{x1}, T_{x2}, T_{y1}, and T_{y2}. Four pairs of vertical and horizontal positions were obtained from two double-PPACs for each focal plane. The horizontal and vertical positions x and y and the angles a, b at the focal plane were determined by tracking the particle applying the least-squares method to four pairs of x_{PPAC} and y_{PPAC} values. Here, a and b correspond to the horizontal and vertical angles with respect to the z axis, respectively. The schematic illustration of this trajectory reconstruction is shown in Fig. 2.7. In the tracking process, pairs of positions with invalid TSum values were rejected. Here TSum for x and y are defined as:

$$\mathrm{TSumX} = (T_{x1} - T_A) + (T_{x1} - T_A)\,, \tag{2.12}$$

$$\mathrm{TSumY} = (T_{y1} - T_A) + (T_{y1} - T_A)\,, \tag{2.13}$$

where T_A indicates the timing signal from the anode plane. Since the length of the delay line was constant, the sum of the times at which signals propagate along the delay line should be constant. Figure 2.8 shows the distribution of TSumX and TSumY. The events located at TSumX $\simeq$ 97 and TSumY $\simeq$ 95 are considered to be valid. On the other hand, events other than this point are invalid events such as multiple hits or δ-ray generation. Only valid TSumX/Y events were used for the above-mentioned trajectory reconstruction.

Next, we explain the procedure for determination of the $B\rho$ value using the transport matrix. The relationships of the positions and angles of the particle between the two focal planes are described using the transport matrix. For example,

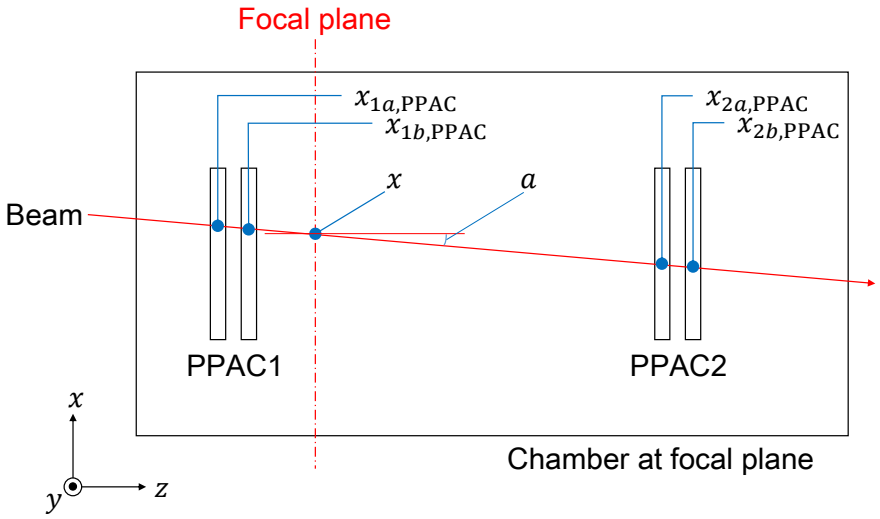

Figure 2.7: Schematic illustration of trajectory reconstruction.

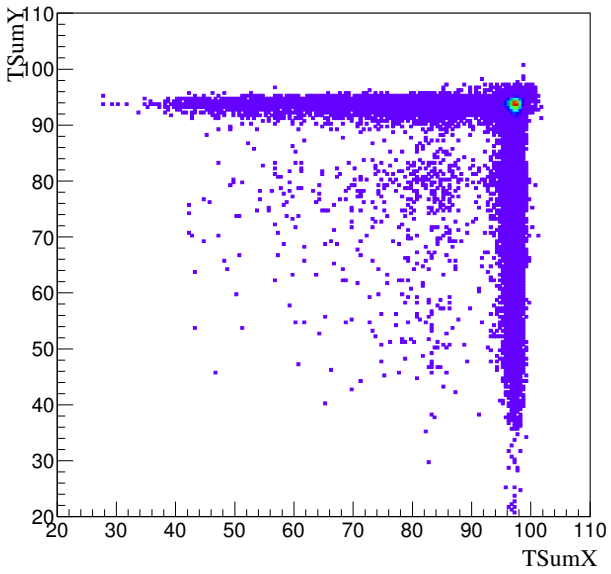

Figure 2.8: Correlation plot of TSumX and TSumY for the first PPAC at F3.

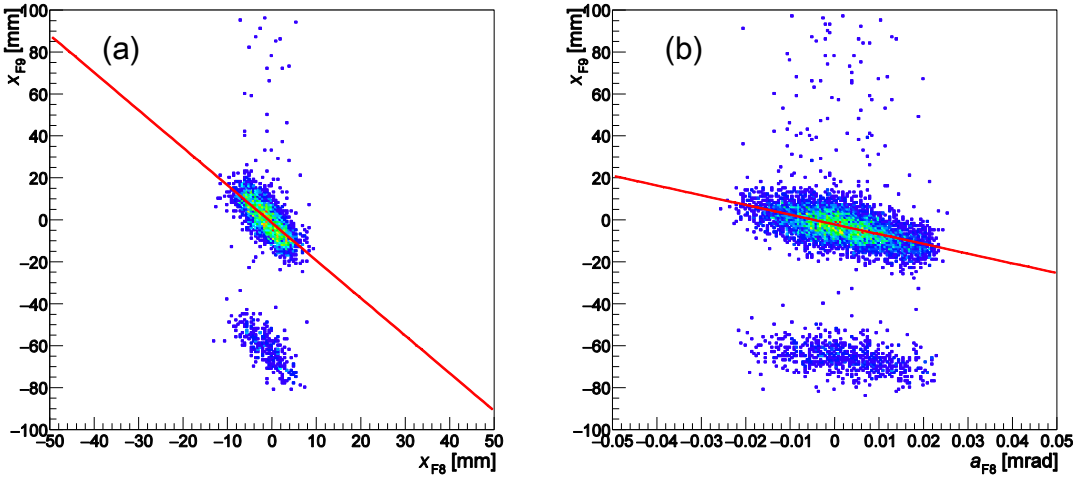

Figure 2.9: (a) Correlation between x_{F8} and x_{F9} in the case of $a_{\mathrm{F8}} \simeq 0$ and $\delta_{\mathrm{F8-F9}} \simeq 0$ for the determination of the matrix element $(x|x)_{89}$. (b) Correlation between a_{F8} and x_{F9} in the case of $x_{\mathrm{F8}} \simeq 0$ and $\delta_{\mathrm{F8-F9}} \simeq 0$ for the determination of the matrix element $(x|a)_{89}$. The red lines show the results of fitting with a linear function.

that between F3 and F5 can be expressed with matrix elements as:

$$\begin{pmatrix} x_{\mathrm{F5}} \\ a_{\mathrm{F5}} \\ \delta_{\mathrm{F5}} \end{pmatrix} = \begin{pmatrix} (x|x)_{35} & (x|a)_{35} & (x|\delta)_{35} \\ (a|x)_{35} & (a|a)_{35} & (a|\delta)_{35} \\ 0 & 0 & 1 \end{pmatrix} \begin{pmatrix} x_{\mathrm{F3}} \\ a_{\mathrm{F3}} \\ \delta_{\mathrm{F3}} \end{pmatrix}, \tag{2.14}$$

where δ indicates the deviation of magnetic rigidity from the magnetic field at the center of D magnet $B\rho_0$ as

$$\delta = 100 \times (B\rho - B\rho_0)\,/B\rho_0. \tag{2.15}$$

The matrix elements for BigRIPS were derived using the COSY INFINITY code [60, 61]; those for ZDS were derived from the ^{93}Zr beam contained in the secondary beam. The correlations of positions and angles were used to derive the matrix elements for ZDS. When $a_{\mathrm{F8}} \simeq 0$ and $\delta_{\mathrm{F8-F9}} \simeq 0$, Eq. (2.14) for transport between F8 and F9 is rewritten as follows:

$$x_{\mathrm{F9}} = (x|x)_{89} x_{\mathrm{F8}}. \tag{2.16}$$

In this situation, the correlation of x_{F8} and x_{F9} yields the matrix element $(x|x)_{89}$, as shown in Fig. 2.9 (a). Similarly, the element $(x|a)_{89}$ can be deduced from the correlation between a_{F8} and x_{F9}, as shown in Fig. 2.9 (b). Then, δ was derived

Table 2.8: Matrix elements used in the $B\rho$ derivation.

Section	$(x\|x)$	$(x\|a)$ [mm/mrad]	$(x\|\delta)$ [%/mm]
F3−F5	0.927	0.00471	31.7
F5−F7	1.08	0.0226	-34.2
F8−F9	-1.95	-0.472	-24.8
F9−F11	0.926	-1.19	12.3

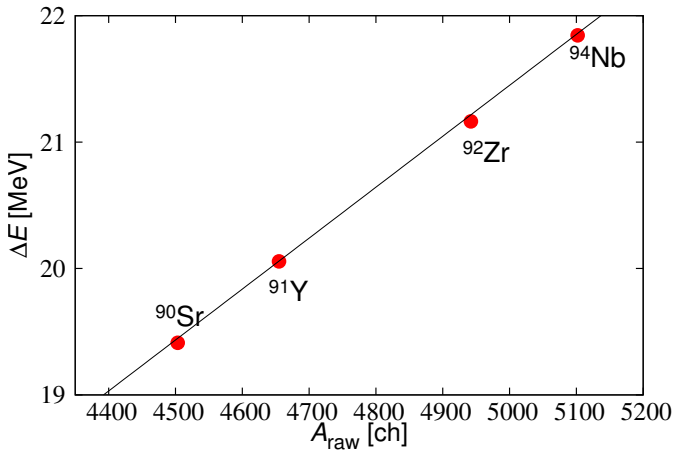

Figure 2.10: Determination of the calibration function by linear fitting of the correlation plot between the output channel and the energy loss at the first layer of MUSIC at F7. The black line shows the fitting function.

from the trajectory and the matrix elements as Eq. (2.17), and δ was converted into $B\rho$ using $B\rho_0$:

$$\delta_{\mathrm{F8-F9}} = \frac{x_{\mathrm{F9}} - (x|x)_{89} x_{\mathrm{F8}} - (x|a)_{89} a_{\mathrm{F8}}}{(x|\delta)_{89}}. \tag{2.17}$$

In this analysis, only the 1st-order matrices were used for the δ determination. Table. 2.8 shows the matrix elements used in the derivation of $B\rho$ in this analysis.

MUSIC

The MUSICs provided six charge signals corresponding to the energy loss in each section of MUSIC. The signals were calibrated from the output channel A_{raw} to the energy loss ΔE using a linear function with two parameters for each layer. The calibration parameters were determined by fitting the correlation plot between the output channel and the energy loss calculated by LISE++ [62] in several secondary

beam nuclei as shown in Fig. 2.10. The averaged energy loss for the six layers was used for the TOF$-B\rho-\Delta E$ method.

2.3.2 Particle Identification

So far, we have explained the analyses of TOF, $B\rho$, and ΔE data. Next, the particle-identification procedure via the TOF$-B\rho-\Delta E$ method is introduced for the case of secondary-beam identification. Then, the results of particle identification of the secondary beam and reaction products are described.

Particle-Identification Procedure

In particle identification, the atomic number Z and the mass-to-charge ratio A/Q were deduced via the TOF$-B\rho-\Delta E$ method. The yields of the secondary beam and the reaction products can be counted directly from the correlation plot between Z and A/Q.

We obtained $\mathrm{TOF}_{\mathrm{F3-F7}}$, $B\rho_{\mathrm{F3-F5}}$, and $B\rho_{\mathrm{F5-F7}}$ from the above analyses. Since a degrader was placed at F5, Eqs. (2.2), (2.3), and (2.4) are transformed into the following equations:

$$\mathrm{TOF}_{\mathrm{F3-F7}} = \frac{L_{\mathrm{F3-F5}}}{\beta_{\mathrm{F3-F5}}c} + \frac{L_{\mathrm{F5-F7}}}{\beta_{\mathrm{F5-F7}}c}, \tag{2.18}$$

$$(A/Q)_{\mathrm{F3-F5}} = \frac{(B\rho)_{\mathrm{F3-F5}}}{\beta_{\mathrm{F3-F5}}\gamma_{\mathrm{F3-F5}}}\frac{c}{m_u}, \tag{2.19}$$

$$(A/Q)_{\mathrm{F5-F7}} = \frac{(B\rho)_{\mathrm{F5-F7}}}{\beta_{\mathrm{F5-F7}}\gamma_{\mathrm{F5-F7}}}\frac{c}{m_u}, \tag{2.20}$$

where $L_{\mathrm{F3-F5}}$ and $L_{\mathrm{F5-F7}}$ denote the flight-path lengths of individual sections and are 23.318 and 23.758 meters, respectively. Assuming that the mass-to-charge ratio A/Q does not change at F5, Eq. (2.21) is derived from Eqs. (2.19) and (2.20):

$$\frac{\beta_{\mathrm{F3-F5}}\gamma_{\mathrm{F3-F5}}}{\beta_{\mathrm{F5-F7}}\gamma_{\mathrm{F5-F7}}} = \frac{(B\rho)_{\mathrm{F3-F5}}}{(B\rho)_{\mathrm{F5-F7}}}. \tag{2.21}$$

Then, $\beta_{\mathrm{F3-F5}}$ and $\beta_{\mathrm{F5-F7}}$ were calculated from Eqs. (2.18) and (2.21). Finally, A/Q for the secondary beam was derived using Eq. (2.20).

The atomic number Z was derived from ΔE and $\beta_{\mathrm{F5-F7}}$ using the following equation transformed from Eq. (2.2):

$$Z = c_{1,Z}\beta_{\mathrm{F5-F7}}\sqrt{\frac{\Delta E_{\mathrm{F7}}}{\ln\frac{2m_ec^2\beta^2_{\mathrm{F5-F7}}}{I} - \ln\left(1-\beta^2_{\mathrm{F5-F7}}\right) - \beta^2_{\mathrm{F5-F7}}}} + c_{2,Z}, \tag{2.22}$$

where $c_{1,Z}$ and $c_{2,Z}$ were the scaling parameters.

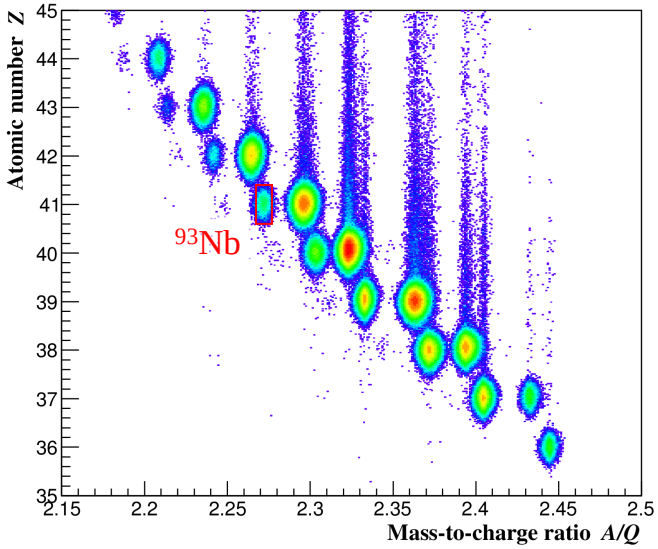

Figure 2.11: Particle identification plot for the secondary beam. The red box outlines the selected ^{93}Nb events.

Particle Identification of the Secondary Beam

Figure 2.11 shows the particle identification plot of the secondary beam based on the correlation between Z and A/Q. Each locus corresponds to a specific isotope. In this experiment, two chains of isotone were contained within the secondary beam. Two characteristic γ rays with the energies of 315 and 492 keV from ^{92m}Y [63] were used for isomer tagging [64, 65] to validate the absolute Z and A/Q. The resolution of 0.40 (FWHM) in Z and 0.23 (FWHM) in A is clearly sufficient to identify the ^{93}Nb beam. Although the beam tails along the y-axis that result from signal pile-up in MUSIC are observed, there is no contamination in the ^{93}Nb beam. Moreover, the contribution of the isomer state ^{93m}Nb (E_x =0.0308 MeV, $T_{1/2}$ = 16.12 years), which is included in the identified ^{93}Nb beam, is estimated to be negligible based on an optical model calculation with the CCONE code [55]. The almost all ^{93}Nb beam were fully-stripped state, that is, all electrons were separated from the ^{93}Nb atom. The events in the ranges $40.6 \leq Z \leq 41.4$ and $2.266 \leq A/Q \leq 2.276$ were selected as ^{93}Nb, as shown by the red box in Fig. 2.11. The energy of the ^{93}Nb beam was determined from $B\rho_{\mathrm{F5-F7}}$. The average $B\rho_{\mathrm{F5-F7}}$ value of the ^{93}Nb beam is 4.04225 Tm, which is equivalent to 142.5 MeV/nucleon. The energy of the ^{93}Nb beam in the secondary target was determined to be 113 MeV/nucleon with an energy spread of $\pm$11 MeV/nucleon, based on beam simulations using the LISE++ code [62] considering the energy loss in the beamline materials from F7 to the secondary target, as listed in Table. 2.9. The specific energy spread of

Table 2.9: Beamline materials from F7 to the secondary target.

Material	Composition	Thickness [mg/cm^2]
F7PPAC1	Mylar foil ($H_8C_{10}O_4$)	6.23
F7MUSIC window	Kapton foil ($C_{22}H_{10}N_2O_4$	35.50
F7MUSIC gas	P10 (H_4CAr_9)	98.27
F7MUSIC electrodes	Mylar foil ($H_8C_{10}O_4$)	13.97
F7PPAC2	Mylar foil ($H_8C_{10}O_4$)	6.23
F7PL	Polyethylene ($H_{10}C_9$)	20.64
F8PPAC1	Mylar foil ($H_8C_{10}O_4$)	6.23
F8PL	Polyethylene ($H_{10}C_9$)	10.32
F8PPAC2	Mylar foil ($H_8C_{10}O_4$)	6.23

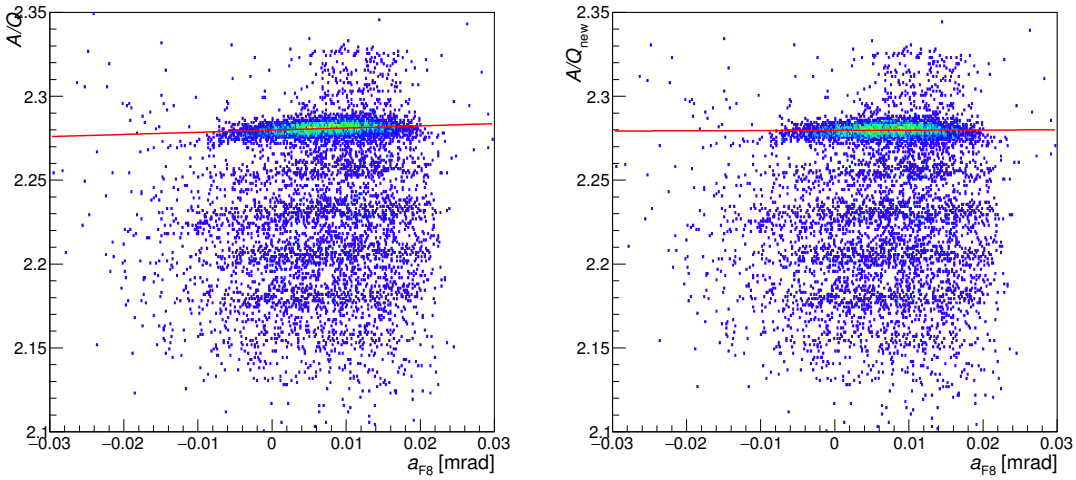

Figure 2.12: Correlation plots between the angle at F8 and the mass-to-charge ratio A/Q. There is linear correlation between A/Q and a_{F8} (Left). The correlation is canceled out (Right). The red lines indicate the fitting function.

the secondary beam was $\pm 0.36\%$, which is negligible compared with that in the secondary targets. The average intensity of the ^{93}Nb beam was approximately 70 counts per second (cps), with 4.4% purity in front of the secondary target, which was calculated as the ratio of the number of ^{93}Nb beam in the red box and the number of total events.

Particle Identification of the Reaction Products

Particle identification of the reaction products was performed in almost the same way as that used for the secondary beam. To achieve a higher resolution in A, A/Q was corrected by the positions and angles at F8, F9, and F11. In principle, A/Q does not correlate with the positions and with the angles at the focal planes. The correlations between A/Q and the position, and between A/Q and the angles, were canceled out using a parameter $c_{A/Q}$ derived by the slope fitting shown in Fig. 2.12. For example, A/Q was corrected by the angle at F8 (a_{F8}) as:

$$A/Q_{\mathrm{new}} = A/Q - c_{A/Q} \times a_{\mathrm{F8}}. \tag{2.23}$$

After canceling, A/Q_{new} showed no correlation with the positions or angles shown in Fig. 2.12.

Figure 2.13 shows the particle-identification plot for the reaction products from the CH_2 target with the 0% $B\rho$ setting after selecting the ^{93}Nb beam. The resolution for ^{90}Nb was 0.53 (FWHM) in Z and 0.26 (FWHM) in A, and individual reaction products were identified unambiguously. Many events located at $Z \simeq 41$ and $A/Q \simeq 2.283$ correspond to the incident ^{93}Nb beam passing through the secondary target without changing A or Z. Also, loci at $Z \simeq 41$ and $A/Q \simeq 2.34$ in the panels (a) and (b) are hydrogen-like ^{93}Nb beam. The correction for such a charge-changing event is described in Sec. 2.3.3.

The yields of each isotope were counted directly from Fig. 2.13. However, there were contaminations of the ^{93}Nb-beam tail along the y axis at the ^{91}Zr and ^{88}Y loci. The contributions of the contaminations were removed by the fitting with two Gaussian functions, as given by $f\,(A/Q)$ with two free parameters A_{beam} and A_{prod}, in order to obtain the yields of ^{91}Zr and ^{88}Y:

$$\begin{aligned} f\,(A/Q) = A_{\mathrm{beam}} \exp\left\{ -\frac{(A/Q - \mu_{\mathrm{beam}})^2}{\sigma_{\mathrm{beam}}^2} \right\} \\ + A_{\mathrm{prod}} \exp\left\{ -\frac{(A/Q - \mu_{\mathrm{prod}})^2}{\sigma_{\mathrm{prod}}^2} \right\}. \end{aligned} \tag{2.24}$$

The first term on the right-hand side of Eq. (2.24) is the component of the ^{93}Nb-beam tail, and the second one is that of the reaction product ^{91}Zr or ^{88}Y. The parameters μ_{beam} and σ_{beam} were fixed to be the same as those of the ^{93}Nb locus in the particle-identification plot of the reaction products. The corresponding A/Q values of ^{91}Zr and ^{88}Y were used for μ_{prod}. In addition, the typical dispersion of the reaction products was used for σ_{prod}. Figure 2.14 shows the two-Gaussian fitting using the likelihood method owing to few statistics for ^{88}Y after selecting Y isotopes ($38.6 \leq Z \leq 39.4$) and for ^{91}Zr after selecting Zr isotopes ($39.6 \leq Z \leq$

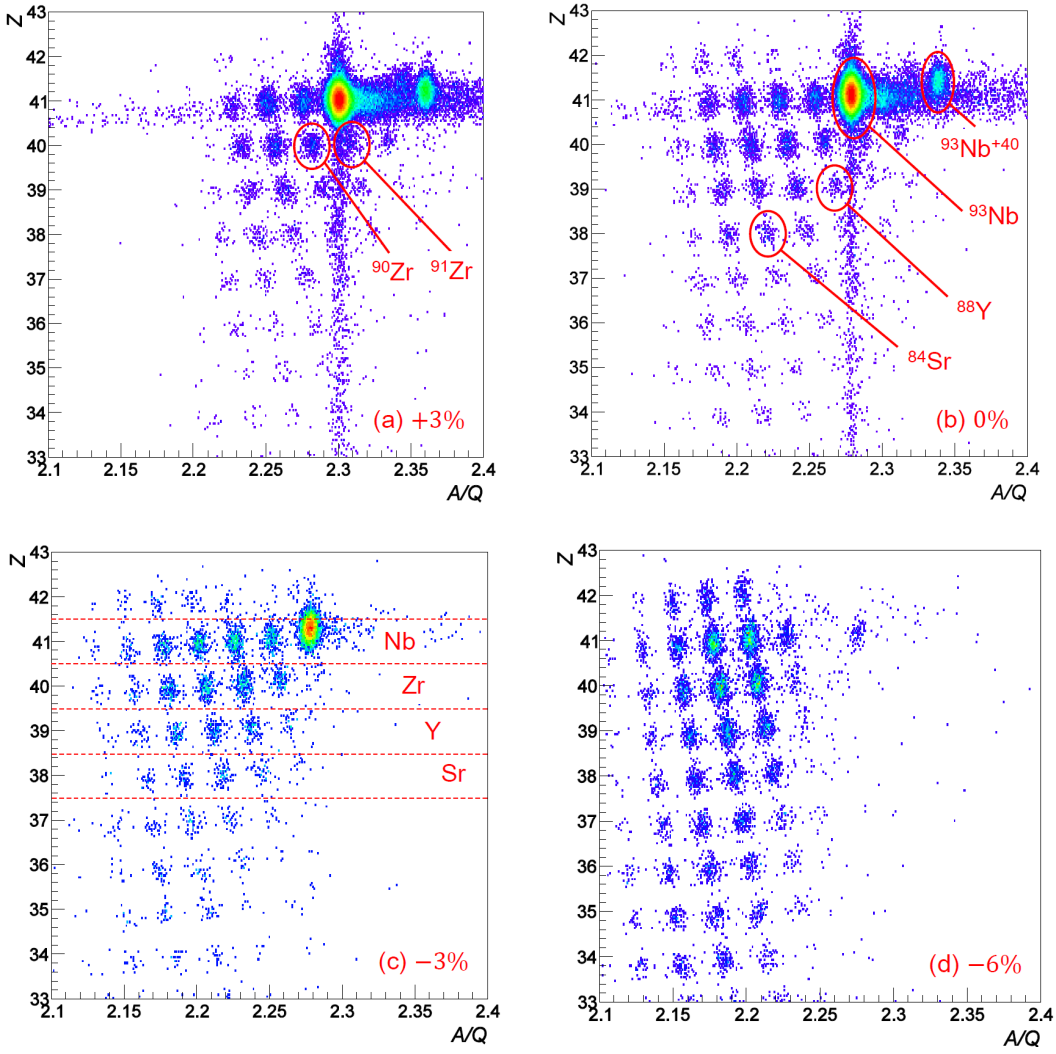

Figure 2.13: Particle identification plot for the reaction products from the CH_2 target with the (a) +3%, (b) 0%, (c) −3%, (d) −6%, and (e) −9% $B\rho$ settings after selecting the ^{93}Nb beam.

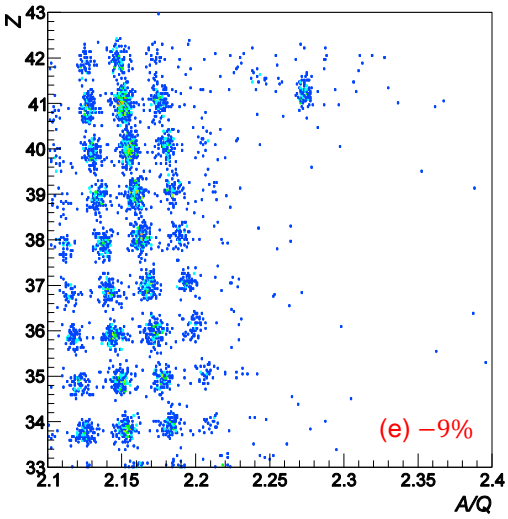

Figure 2.13: *Continued.*

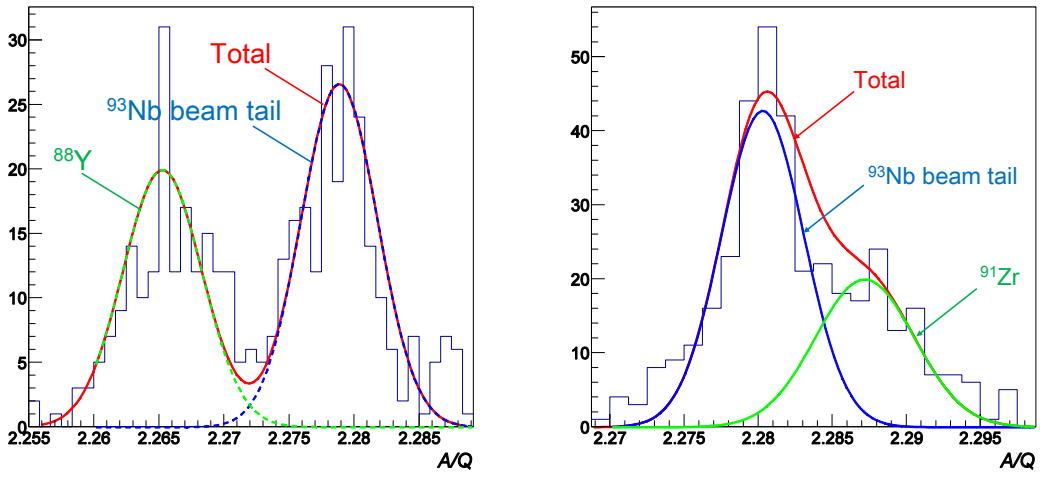

Figure 2.14: Two-Gaussian fittings for ^{88}Y (Left) and ^{91}Zr (Right). The green, blue, and red lines indicate the components of the reaction products, the ^{93}Nb-beam tail, and the total, respectively.

40.4). The yields of ^{88}Y and ^{91}Zr were calculated using Eq. (2.25) with the obtained parameters A_{beam} and A_{prod} from the fitting, as well as the number of all events

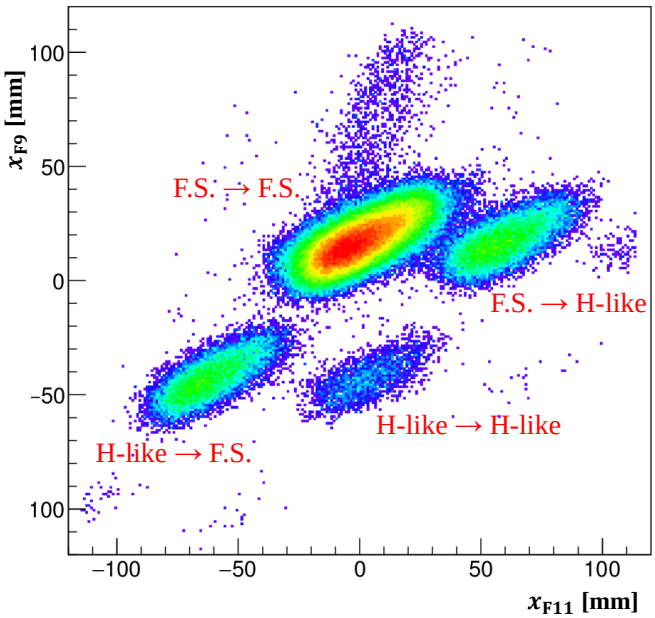

Figure 2.15: Charge-state distribution in the ZDS given by the horizontal positions at F9 and F11 for the CH_2 target and the +3% $B\rho$ setting after selecting the ^{93}Nb beam.

in the fitting range N_{all} in order to conserve this quantity:

$$(\mathrm{Yield}) = N_{\mathrm{all}} \times \frac{A_{\mathrm{prod}}\sigma_{\mathrm{prod}}}{A_{\mathrm{beam}}\sigma_{\mathrm{beam}} + A_{\mathrm{prod}}\sigma_{\mathrm{prod}}}. \tag{2.25}$$

2.3.3 Corrections

Correction for Charge-state Changes

The secondary beam and the reaction products were mostly in fully stripped (F.S.) states, for which the charge is proportional to eZ. However, the charge-states can change by picking up or losing electrons while passing through beamline materials. Since the charge state of the particles is assumed not to change at intermediate focal planes F5 and F9, as mentioned in Sec. 2.3.2, such events should be removed from the analysis. Charge-state-changing events that produce hydrogen-like (H-like) or helium-like (He-like) particles before the final focal plane of BigRIPS were removed automatically by selecting the ^{93}Nb beam in Fig. 2.11. On the other hand, such charge-state-changing events also need to be eliminated in the ZDS. Figure 2.15 shows the charge-state distribution in the ZDS after selecting the ^{93}Nb beam. The vertical and horizontal axes correspond to the horizontal positions at

Table 2.10: Charge-state distributions of the ^{93}Nb beam. LISE++ calculations were performed at energies of 113 MeV/nucleon (CH_2-, CD_2-, and C-targets case) and 80 MeV/nucleon (empty-target case).

Secondary	Target	F.S.→F.S.	F.S.→H-like	H-like→F.S.	H-like→H-like
CH_2	exp	77.78	10.45	8.95	2.18
	calc	77.55	10.61	10.05	1.79
CD_2	exp	76.65	11.26	8.71	2.30
	calc	76.01	10.47	11.48	2.04
C	exp	77.65	10.70	8.68	2.29
	calc	78.56	10.80	9.03	1.61
Empty	exp	80.89	6.81	8.78	2.96
	calc	80.36	13.43	6.21	0.00

F9 and F11, respectively. Each locus corresponds to the charge state in the first and second halves of the ZDS. The vertical axis represents the charge state in the first half, whereas the horizontal axis corresponds to the difference between the charge states of the first and second halves. The locus in the upper center corresponds to fully stripped events in both sections (F.S. → F.S.), and the loci at opposite sides of the horizontal axis represent charge-state-changing events at F9, *i.e.*, fully stripped to hydrogen-like (F.S. → H-like) events at the right-hand side and hydrogen-like to fully-stripped (H-like → F.S.) events at the left-hand side. The locus located at the lower center is equivalent to hydrogen-like events over the whole ZDS (H-like → H-like). These charge-state-changing events were removed prior to particle identification. The measured distribution of the charge state for the ^{93}Nb case is listed in Table. 2.10 together with the calculated distribution by the LISE++ code. This calculation was performed with an energy of 113 MeV/nucleon for the CH_2-, CD_2-, and C-target cases and with an energy of 80 MeV/nucleon for empty-target case in order to reproduce the measured charge-state distribution. The differences between the calculated and experimental F.S. → F.S. ratios are less than 1%. Therefore, the yields of the removed charge-state-changing events for each isotope were compensated using the ratio of the F.S. events over the whole ZDS to the total events calculated by the LISE++ code.

Correction for Acceptance

In the achromatic mode, the acceptance of ZDS is limited by the horizontal position at F9. It is possible that reaction products passing through near the edge of the focal plane may be lost for some $B\rho$ settings. Thus, it is necessary to compensate

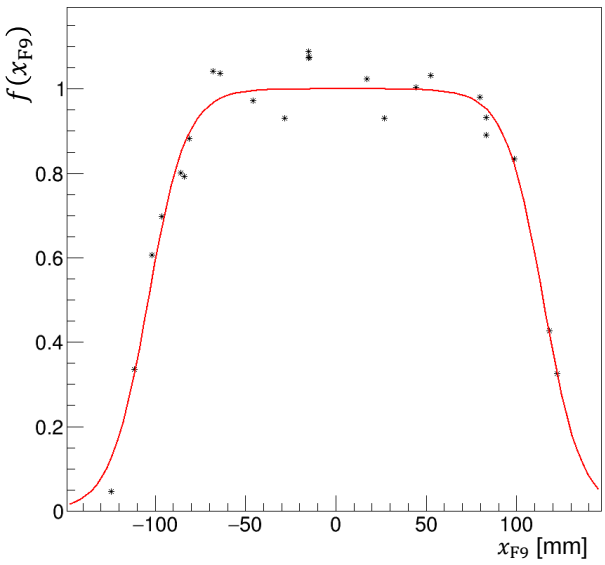

Figure 2.16: Survival-rate distribution as a function of x_{F9}, denoted by the black points and Eq. (2.16), derived by fitting with the Woods-Saxon function indicated by the red line.

for these lost events as a function of the horizontal position at F9. From the yields of several major reaction products ^{92}Nb, ^{89}Nb, ^{90}Zr, ^{89}Zr, and ^{88}Zr, we derived the survival rate S as a function of the horizontal position at F9 (x_{F9}) as the ratio of the reaction rates for runs at two different $B\rho$ settings. For example, the following equation shows the survival rate when all produced isotopes were detected at the -3% setting, and some of the particles were lost in 0% setting:

$$S\left(x_{\mathrm{F9}}\right) = \frac{Y_{0\%}/B_{0\%}}{Y_{-3\%}/B_{-3\%}}, \tag{2.26}$$

where Y and B correspond to the numbers of detected reaction products and incident-beam particles of ^{93}Nb, respectively. As mentioned above, the $B\rho$ setting in the denominator was suitably selected so as to accept all produced isotopes. We fitted the deduced survival rate $S\left(x_{\mathrm{F9}}\right)$ for each isotope with the following Woods-Saxon function, with parameters a, b, and V:

$$f\left(x_{\mathrm{F9}}\right) = \left\{1 + \exp\left(\frac{|x_{\mathrm{F9}} - b| - V}{a}\right)\right\}^{-1}. \tag{2.27}$$

Figure 2.16 shows the result of the fitting. The parameters obtained are $a = 11.61 \pm 1.19$, $b = 4.15 \pm 1.22$, and $V = 109.72 \pm 1.25$. We made the final acceptance

correction for the ZDS using Eq. (2.27) to obtain the total yields of all produced isotopes.

2.3.4 Isotope-Production Cross Sections

Isotope-production cross sections for p- and d-induced reactions were derived by subtracting the background contributions of the beamline materials and the carbon target from the yields measured in the CH_2 and CD_2 target runs, respectively. The contribution to the yields of reaction products from carbon nucleus in CH_2 and CD_2 was almost the same as those from hydrogen and deuterium. For the individual ZDS $B\rho$ settings, the p-induced cross section σ_p is given by

$$\sigma_p = \frac{1}{2}\left\{\frac{1}{t_{\mathrm{CH_2}}}\left(\frac{Y_{\mathrm{CH_2}}}{c_{\mathrm{CH_2}}B_{\mathrm{CH_2}}} - \frac{Y_{\mathrm{emp}}}{c_{\mathrm{emp}}B_{\mathrm{emp}}}\right) - \frac{1}{t_{\mathrm{C}}}\left(\frac{Y_{\mathrm{C}}}{c_{\mathrm{C}}B_{\mathrm{C}}} - \frac{Y_{\mathrm{emp}}}{c_{\mathrm{emp}}B_{\mathrm{emp}}}\right)\right\}, \quad (2.28)$$

where B is the number of incident ^{93}Nb ions, Y is the number of detected reaction products, and t is the areal density of the reaction targets. The parameter c corresponds to the correction factor for charge-state changes. The subscripts CH_2, C, and emp denote individual runs with the CH_2, C, and empty-frame targets, respectively. The statistical uncertainty δ_p is calculated by

$$\delta_p = \frac{1}{2}\sqrt{\frac{Y_{\mathrm{CH_2}}^2}{t_{\mathrm{CH_2}}^2 c_{\mathrm{CH_2}}^2 B_{\mathrm{CH_2}}^2}\left(\frac{1}{Y_{\mathrm{CH_2}}} + \frac{1}{B_{\mathrm{CH_2}}}\right) + \frac{Y_{\mathrm{C}}^2}{t_{\mathrm{C}}^2 c_{\mathrm{C}}^2 B_{\mathrm{C}}^2}\left(\frac{1}{Y_{\mathrm{C}}} + \frac{1}{B_{\mathrm{C}}}\right)} \\ \overline{+\frac{Y_{\mathrm{emp}}^2}{c_{\mathrm{emp}}^2 B_{\mathrm{emp}}^2}\left(\frac{1}{t_{\mathrm{CH_2}}} - \frac{1}{t_{\mathrm{C}}}\right)^2\left(\frac{1}{Y_{\mathrm{emp}}} + \frac{1}{B_{\mathrm{emp}}}\right)}. \quad (2.29)$$

For the d-induced case, the subscript CH_2 is replaced by CD_2. The isotope-production cross section for C-induced reactions was derived by subtracting the contribution of the beamline materials from the C-target run using the following equation:

$$\sigma_{\mathrm{C}} = \frac{1}{t_{\mathrm{C}}}\left(\frac{Y_{\mathrm{C}}}{c_{\mathrm{C}}B_{\mathrm{C}}} - \frac{Y_{\mathrm{emp}}}{c_{\mathrm{emp}}B_{\mathrm{emp}}}\right). \quad (2.30)$$

The statistical uncertainty δ_{C} is determined by

$$\delta_{\mathrm{C}} = \frac{1}{t_{\mathrm{C}}}\sqrt{\frac{Y_{\mathrm{C}}^2}{B_{\mathrm{C}}^2}\left(\frac{1}{Y_{\mathrm{C}}} + \frac{1}{B_{\mathrm{C}}}\right) + \frac{Y_{\mathrm{emp}}^2}{B_{\mathrm{emp}}^2}\left(\frac{1}{Y_{\mathrm{emp}}} + \frac{1}{B_{\mathrm{emp}}}\right)}. \quad (2.31)$$

Final isotope-production cross sections were determined as weighted means of the cross sections measured for different ZDS $B\rho$ settings, with the weights given by statistical uncertainties.

2.3.5 Systematic Uncertainty Evaluation

The systematic uncertainties in the measured production cross sections are composed of two major components: the uncertainty in the areal density of the reaction targets and the correction factor c in Eq. (2.28) for charge-state changes. The former were estimated to be less than 2% in Ref. [43], and the latter was estimated to be less than 1% based on comparisons between the experimental and calculated correction factors for charge-state changes, as shown in Table. 2.10.

2.4 Results and Discussion

First, the isotope-production cross sections measured for the p-, d-, and C-induced reactions on ^{93}Nb are presented and comparison is made among them. Then, the present data for the p-induced reactions are compared with past data measured by the activation method [66] to check the consistency between the inverse-kinematics and activation methods. In addition, benchmark tests of theoretical-model calculations and nuclear data libraries are performed using our measured isotope-production cross sections. Finally, comparisons between the ^{93}Nb data and the previously measured ^{93}Zr data [44] are discussed, with a focus on the effects of shell closure on isotope production in p- and d-induced spallation reactions.

2.4.1 Experimental Data

Figure 2.17 shows the isotope-production cross sections for p-, d-, and C-induced reactions on ^{93}Nb at an energy of 113 MeV/nucleon using the inverse-kinematics method. The error bars include only the statistical uncertainties. The experimental results demonstrate the advantages of the inverse-kinematics method, with which one can measure isotope-production cross sections over a wide range of isotopic chains, including stable isotopes.

As shown in panel (a) in Fig. 2.17, the value of σ_p for Mo isotopes for which the atomic number is increased by one ($\Delta Z = +1$) from the projectile ^{93}Nb is approximately twice as large as σ_d. A similar tendency is observed in the production of isotopes with $\Delta Z = +1$ in other studies [26, 43, 44, 47]. From Nb isotopes (b) to Rb isotopes (f), σ_p decreases more rapidly with decreasing atomic number than σ_d and σ_C, resulting in σ_p being smaller than σ_d and σ_C for the Y, Sr, and Rb isotopes. This can be explained by differences in the excitation energies of the pre-fragments formed by the intranuclear cascade process. The incident energy per nucleon is the same for three targets, but the total incident energies of the d- and C-induced reactions are higher than for the p-induced reactions. Thus, it is expected that pre-fragments with higher excitation energies are formed in the d-

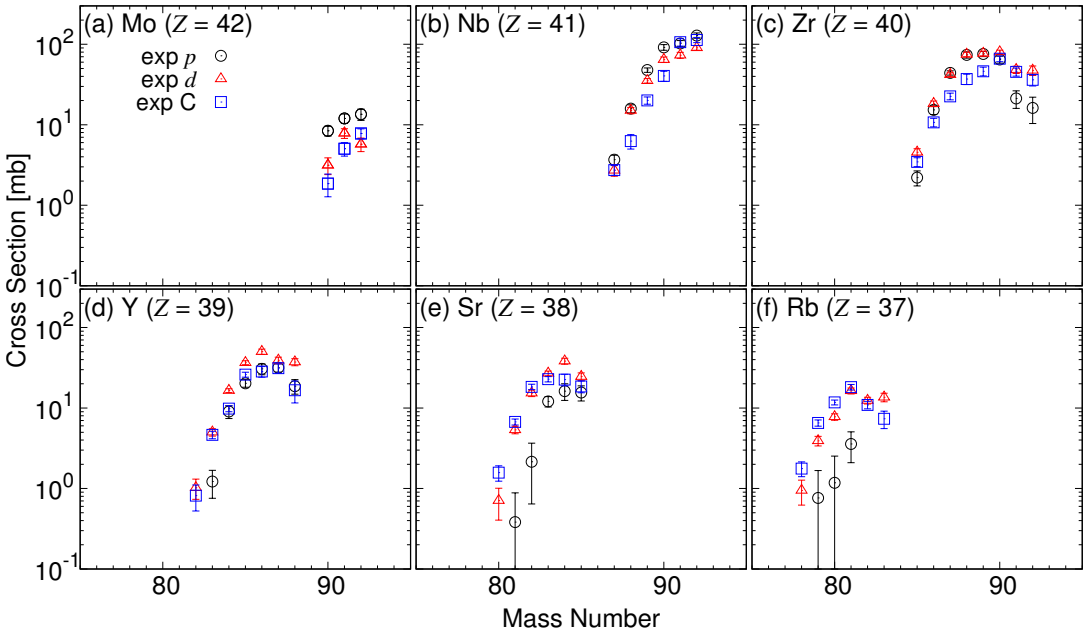

Figure 2.17: Measured isotope-production cross sections for ^{93}Nb + p, d, and C reactions at 113 MeV/nucleon: (a) Mo, (b) Nb, (c) Zr, (d) Y, (e) Sr, and (f) Rb. The black circles, red triangles, and blue squares represent the production cross sections for the p-induced reactions (σ_p), d-induced reactions (σ_d), and C-induced reaction (σ_C), respectively.

and C-induced reactions than in the p-induced reactions, and the production yields of isotopes with lower Z are enhanced by the sequential decays of more nucleons than in p-induced reactions.

In Fig. 2.17, discontinuity is observed in the production cross sections for p-, d-, and C-induced reactions between ^{90}Zr and ^{91}Zr because of the closed-shell structure at the neutron magic number $N = 50$. The neutron-separation energies S_n are 8,634.78 keV for ^{92}Zr, 7,194.35 keV for ^{91}Zr, 11,968 keV for ^{90}Zr, and 9,318 keV for ^{89}Zr [67]. Thus, ^{91}Zr emits a neutron more easily than the other Zr isotopes. The production of ^{90}Zr therefore increases relative to that of ^{91}Zr. These discontinuous jumps are weakened for the heavier incident particles, because the larger excitation energies of the pre-fragments probably allow them to compensate for the effects of shell structure. Although a jump was observed in the Zr isotopes ($\Delta Z = 0$) in the ^{93}Zr data [44], no jump appeared for the Nb isotopes ($\Delta Z = 0$) in the ^{93}Nb data, despite the large gap in S_n between ^{92}Nb ($S_n = 7,887$ keV) and ^{91}Nb ($S_n = 12,048$ keV). We discuss this difference in the context of a theoretical-model calculation in Sec. 2.4.4.

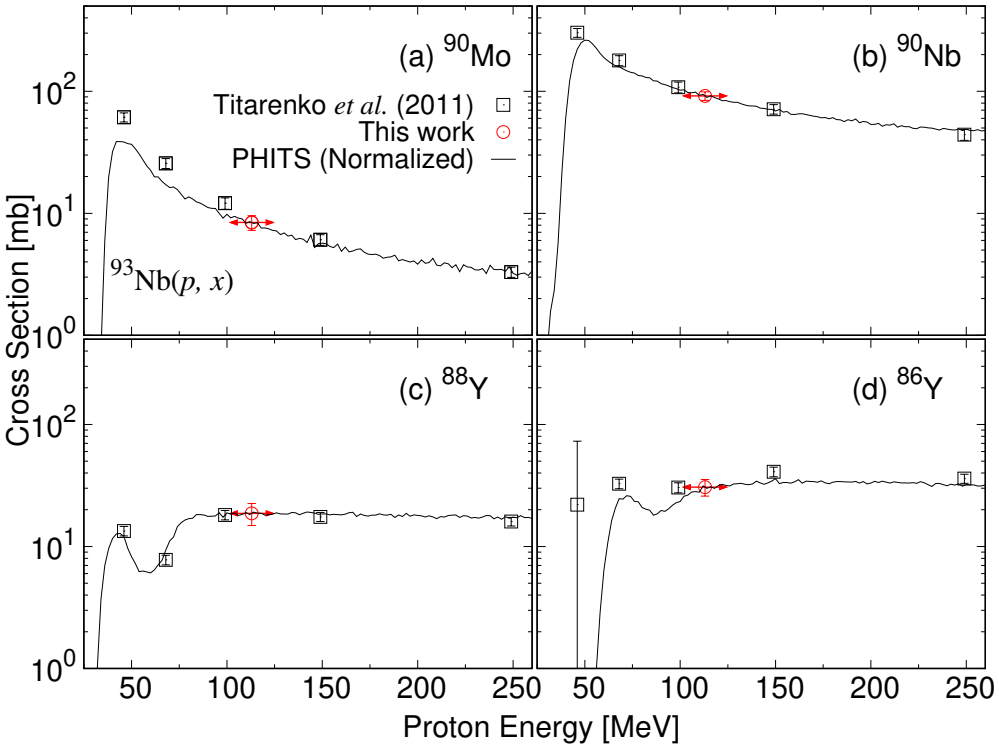

Figure 2.18: Comparison between data measured by the inverse-kinematics method and by the activation method [66] for the production cross sections of (a) ^{90}Mo, (b) ^{90}Nb, (c) ^{88}Y, and (d) ^{86}Y. The red circles represent the data measured via the inverse-kinematics method along with their statistical uncertainties, and the red arrows in the x-direction correspond to the energy spread at the reaction targets. The black lines are the calculations by PHITS, which are normalized by the present data. The activation data are denoted by black squares.

2.4.2 Comparison with the Activation Data

Several isotope-production datasets measured by the conventional activation method have been reported to date for p-induced reactions on ^{93}Nb [66]. The present data measured by the inverse-kinematics method can be compared with the measured data provided as independent yields from these activation data. Here, we choose four radioactive isotopes, ^{90}Mo, ^{90}Nb, ^{88}Y, and ^{86}Y, for comparison. The results are shown in Fig. 2.18. Note that the red horizontal arrows indicate the energy spread in the reaction target. The black squares denote the activation data [66]. The calculated production cross sections by PHITS are displayed by the black lines as an eye guide. The PHITS calculation is normalized by the present data in each panel. These figures show that, within the experimental uncertainties, the data

measured by the inverse-kinematics method are consistent with those measured by the activation method.

2.4.3 Comparison with Model Calculations and Nuclear Data Libraries

In this subsection, we perform benchmark tests for the reaction models implemented in PHITS version 3.10 [48, 49], for CCONE code [55], and for the nuclear data libraries [50–52] by comparisons with the isotope-production cross section data obtained in the present work. In the PHITS calculations, a spallation reaction is described as a two-step process; that is, pre-fragments are formed via the intranuclear cascade (INC) process, and the excited pre-fragments subsequently decay by the evaporation of light particles and γ rays. The present σ_p and σ_d data are used to benchmark the Liège Intranuclear Cascade model (INCL4.6) [53] for the INC process and the Generalized Evaporation Model (GEM) [54] for the evaporation process. The CCONE code includes the optical model, the pre-equilibrium exciton model, and the Hauser-Feshbach statistical model with width-fluctuation correction as the nuclear-reaction model. In addition, the experimental σ_p data are compared with data stored in the latest nuclear data libraries, *i.e.*, JENDL-4.0/HE [50], JENDL/ImPACT-2018 [68], TENDL-2017 [51], and ENDF/B-VIII.0 [52]. Among these libraries, TENDL-2017 contains the σ_d data, but the maximum incident energy of 200 MeV is less than the total incident energy of 226 MeV in the present measurements. Therefore, the experimental σ_d data are not compared with the TENDL-2017 data. The σ_C data are compared with model calculations using JQMD [56] and JQMD-2.0 [69], where JQMD-2.0 is a modified version of JQMD that was implemented in PHITS to improve the treatment of peripheral collisions by considering the relativistic covariance of the Hamiltonian and modifying the treatment of neutron-proton scattering near the nuclear surface. PHITS has several options for the total reaction cross sections: we employ the Pearlstein-Niita formula [70] for p-induced reactions and the KUROTAMA model [71, 72] for the d- and C-induced reactions in the present work. The details of the models and the libraries are introduced in Appendix A.

Proton- and Deuteron-induced Reactions

Figure 2.19 compares our experimental σ_p and σ_d data with calculations that use INCL4.6 plus GEM implemented in the PHITS and CCONE code. The black circles and red triangles denote the experimental σ_p and σ_d data, respectively, and the black solid and red dotted lines represent the corresponding theoretical calculations by INCL4.6/GEM. Moreover, the black dash-dotted line corresponds to the CCONE calculation with the optical potentials (OPs) of Koning and Delaroche

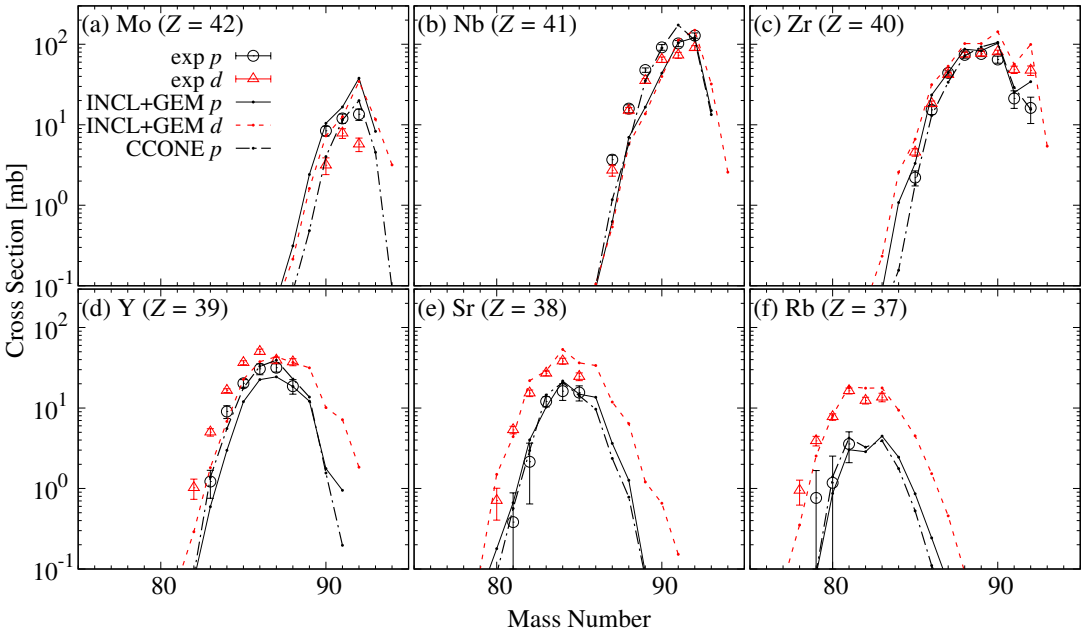

Figure 2.19: Comparison between the experimental isotope-production cross sections for p- and d-induced reactions on ^{93}Nb at 113 MeV/nucleon, the PHITS calculations with INCL4.6/GEM, and the CCONE calculation.

for the proton and neutron [73], and of An and Cai for the deuteron [74].

The χ^2 value is calculated with the formula:

$$\chi^2 = \frac{1}{n}\sum_{i}^{n}\left(\frac{\mathrm{exp}_i - \mathrm{calc}_i}{\mathrm{err}_i}\right)^2, \tag{2.32}$$

where n, exp_i, err_i, and calc_i represent the number of measured datapoints, the measured cross section, the statistical error of this cross section, and the calculated cross section, respectively. The χ^2 values are 13.1 for p-induced reactions in PHITS, 51.5 for d-induced reactions in PHITS, and 6.84 for p-induced reactions in the CCONE calculation. The χ^2 value for the d-induced reaction in PHITS is approximately four times worse than that for the p-induced reaction in PHITS because the production cross sections for isotopes near the target nucleus ^{93}Nb are significantly overestimated in d-induced reactions. The CCONE shows a smaller χ^2 value than the PHITS calculation, because it fairly well predicts production cross sections such as ^{92}Mo and ^{89}Nb.

The PHITS calculation shows overall agreement with the measured isotope-production cross sections for both p- and d-induced reactions. The jumps in the production cross sections at a neutron magic number of 50 for the Zr isotopes are

reproduced reasonably well in panel (c), whereas neither the calculation nor the measured cross section show a jump at the neutron magic number for Nb isotopes in panel (b). The effects of shell closure on isotope production will be discussed together with the data on the ^{93}Zr + p and d reactions [44] in Sec. 2.4.4. There are three major discrepancies between the experimental data and the PHITS calculations in Fig. 2.19. First, the calculations overestimate the production cross sections of isotopes near the target nucleus, such as ^{92}Mo and ^{92}Zr. A similar overestimation was observed in our previous data on the ^{93}Zr + p and d reactions [44]. The INC process described by the INCL4.6 model dominates the formation of these isotopes, as shown below in Sec. 2.4.4. As discussed in Refs. [44, 75, 76], one reason for such overestimation is that the INCL4.6 model fails to reproduce the excitation-energy distributions in the pre-fragments formed after the INC process. If the transition to highly excited states in the pre-fragments is enhanced, the production of ^{92}Mo and ^{92}Zr is expected to be reduced, because more nucleons can be emitted from the pre-fragments via the evaporation process. Second, the even-odd staggering (EOS) in the calculational results, which is shown clearly in Fig. 2.19 (e), is not appreciable in the experimental data. A similar situation was also pointed out in Ref [43, 44]. The exaggerated even-odd staggering may be caused by the absence of competition between particle and γ-ray emissions in the evaporation process or by inappropriate pairing corrections in the level densities employed in the GEM in the PHITS calculations [43]. Third, the PHITS calculations underpredict the neutron-deficient region in odd-Z isotopes such as the Nb and Y isotopes. This underestimation may be originated from the mis-prediction of the proton-neutron branching ratio of pre-fragment due to the above-mentioned inappropriate pairing corrections in the level densities. A detailed discussion of this underestimation is presented in Sec. 3.4.4. The C/E values of the PHITS calculations are drawn in the chart of the nuclides for the p- and d-induced reactions in Figs. 2.20 and 2.21, respectively. The black squares show the stable isotopes and the black circle shows the target nucleus, ^{93}Nb. The grey line surrounds the datapoints. Figures 2.20 and 2.21 clearly show the EOS along both the proton and neutron numbers. This fact strongly implies the existence of an inappropriate pairing correction in the level densities.

The CCONE calculation predicts the isotope-production cross sections for the p-induced reaction fairly well, especially ^{92}Mo and ^{92}Zr compared with the PHITS calculation. The CCONE calculation also shows the jump both in the Nb and Zr isotopic chains. However, the CCONE calculation shows the effect of a closed shell $N = 50$ in the Nb isotope despite of the absence of a jump in the measured data, resulting in overestimation in ^{91}Nb.

In Fig. 2.22, the isotope-production cross sections taken from JENDL-4.0/HE, JENDL/ImPACT-2018, TENDL-2017, and ENDF/B-VIII.0 are plotted together

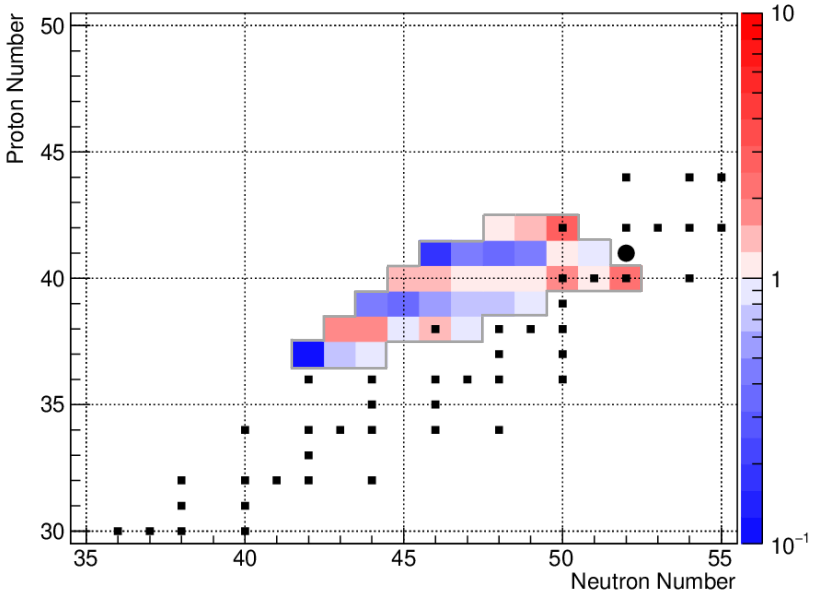

Figure 2.20: C/E values of the PHITS calculation drawn in the chart of the nuclides for the p-induced reaction on ^{93}Nb. The grey line surrounds the datapoints.

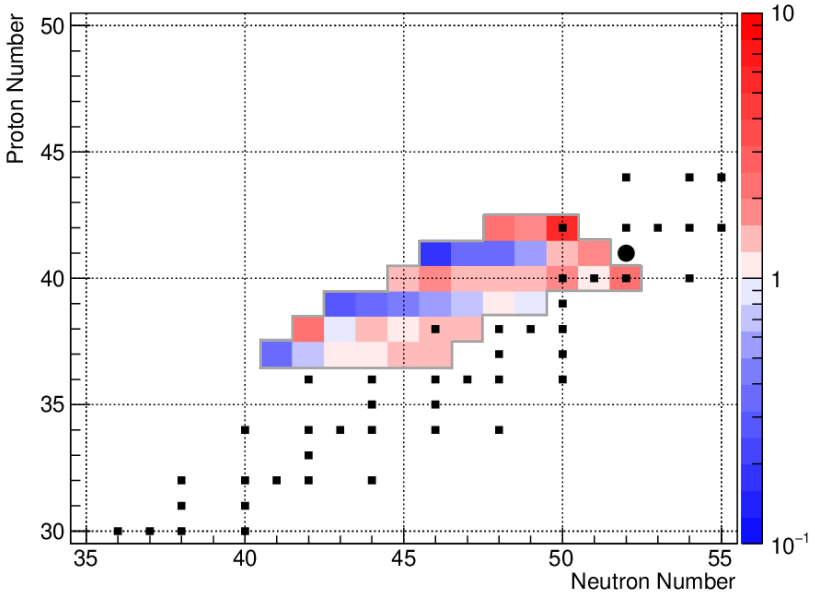

Figure 2.21: Same as Fig. 2.21, but for the d-induced reaction on ^{93}Nb.

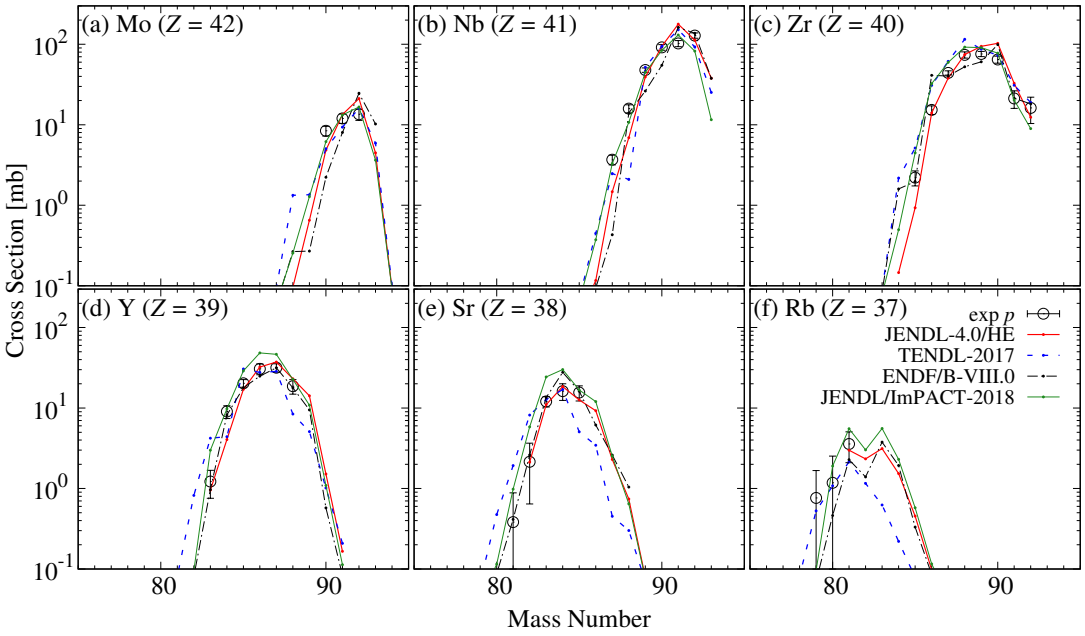

Figure 2.22: Comparison of the experimental isotope-production cross sections for p-induced reactions on ^{93}Nb at 113 MeV with four nuclear data libraries: JENDL-4.0/HE (red solid), JENDL/ImPACT-2018 (green solid), TENDL-2017 (blue dashed), and ENDF/B-VIII.0 (black dash-dotted).

with the measured data. The χ^2 values are 6.92 for JENDL-4.0/HE, 9.51 for JENDL/ImPACT-2018, 12.11 for TENDL-2017, and 13.29 for ENDF/B-VIII.0. The JENDL-4.0/HE cross sections show fairly good agreement with the measured data, resulting in the smallest χ^2 value among all the nuclear data libraries, even smaller than for the PHITS calculations, although there are no data in the low-mass-number regions for the Sr and Rb isotopes. Moreover, JENDL-4.0/HE generally overestimates the production cross sections of the Mo, Nb, and Zr isotopes at $N = 50$. As for JENDL/ImPACT-2018, the overestimations at the neutron magic number $N = 50$ are improved compared to JENDL-4.0/HE. This is because the contribution of the pre-equilibrium process is weakened in JENDL/ImPACT-2018. Thus pre-fragments with higher excitation energies are more likely to be generated, resulting in enhanced nucleon emission. However, this tuning also affects the isotopic distributions in the Y, Sr, and Rb isotopes, and there are overestimations over the mass region. There are three major discrepancies between TENDL-2017 and the experimental data: the peak seen in ^{91}Nb; the overestimates seen in the even-Z isotopes, *i.e.*, Zr, in contrast to the INCL4.6/GEM calculations; and the strong even-odd staggering seen in all the isotopes. In contrast, ENDF/B-VIII.0

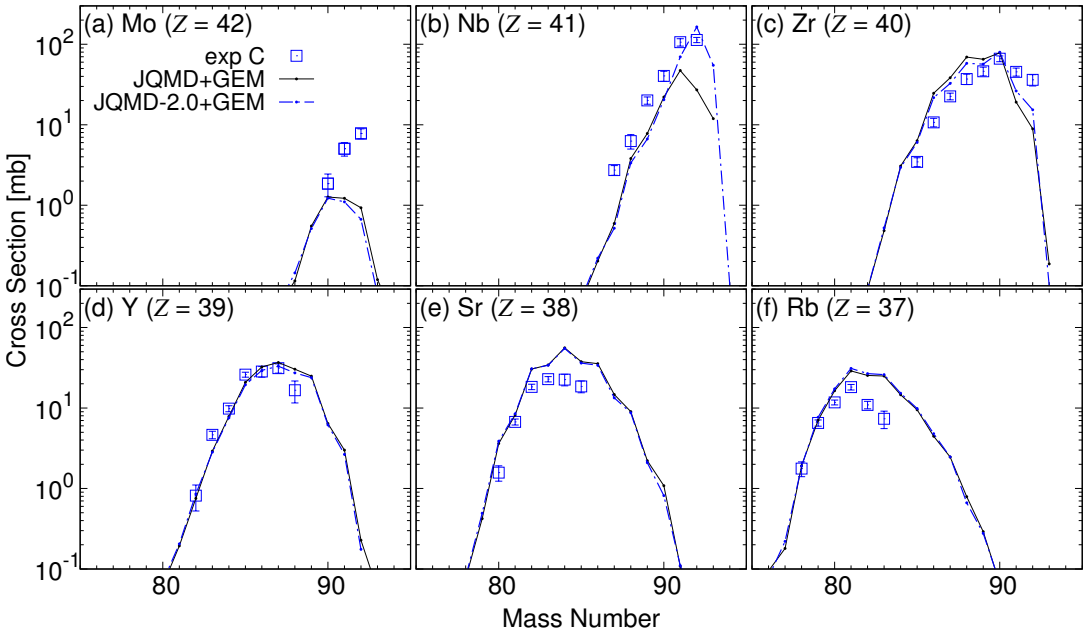

Figure 2.23: Comparison of the experimental isotope-production cross sections for C-induced reactions on ^{93}Nb at 113 MeV/nucleon and PHITS calculations with JQMD/GEM (black solid) and JQMD-2.0/GEM (blue dash-dotted).

reproduces the isotopic distributions of Y and Sr better than others, but the even-odd staggering appears strongly in the Zr isotopes, which results in the worst χ^2 value among the four nuclear data libraries.

Carbon-induced Reactions

Figure 2.23 compares between the measured σ_C and PHITS calculations using JQMD/GEM and JQMD-2.0/GEM. The blue squares, black solid lines, and blue dash-dotted lines correspond to the experimental data, the JQMD/GEM calculations, and the JQMD-2.0/GEM calculations, respectively. The JQMD/GEM results show much smaller production cross sections for the isotopes near ^{93}Nb, because JQMD does not treat peripheral collisions appropriately. These calculations have recently been improved by considering the relativistic covariance of the Hamiltonian and by modifying the treatment of neutron-proton scattering near the nuclear surface. The improved version is called JQMD-2.0 [69]. As shown in Fig. 2.23, the JQMD-2.0 calculations result in a considerable improvement in the underestimation of ^{91,92}Nb, whereas only slight changes appear in the production cross sections of the other isotopes. The productions of ^{91,92}Nb are sensitive to the treatment of neutron-proton scattering near the nuclear surface, because

peripheral collisions generate pre-fragments with low excitation energy, resulting in one- or two-neutron-knockout reactions. As a result, the production of ^{91,92}Nb is enhanced. However, the production cross sections for ^{91,92}Mo are considerably underestimated in both of calculations. In the calculated isotopic distributions, the strong even-odd staggering is seen in the Zr and Sr isotopes, just as in the p- and d-induced cases shown in Fig. 2.19. In addition, the production cross sections for the Nb isotopes are underestimated in the neutron-deficient region, whereas those in the neutron-rich regions of the Y, Sr, and Rb isotopes are overestimated. This disagreement may be due mainly to the modeling in GEM, as it was for the p- and d-induced reactions. Finally, the χ^2 values are 34.2 for JQMD/GEM and 31.2 for JQMD-2.0/GEM. The latter is slightly better than the former, thanks to improvements in the treatment of peripheral collisions in JQMD-2.0.

2.4.4 Comparison with ^{93}Zr Data

We compare the present ^{93}Nb data and the previous ^{93}Zr data [44], paying especial attention to the effect of neutron-shell closure at $N = 50$ on isotope production. Both nuclei are isobars with $A = 93$: the proton number is $Z = 41$ and the neutron number is $N = 52$ for ^{93}Nb, whereas they are $Z = 40$ and $N = 53$ for ^{93}Zr. Note that the reaction energies are 113 MeV/nucleon for ^{93}Nb and 105 MeV/nucleon for ^{93}Zr. Since this difference is less than 10%, however, the influence on the following discussion is expected to be negligible.

The isotopic distributions of the ^{93}Nb and ^{93}Zr data are compared in Fig. 2.24. Panels (a) and (c) show the isotope-production cross sections for (p, pxn) reactions on ^{93}Nb and ^{93}Zr, respectively, whereas panels (b) and (d) present those for $(p, 2pxn)$ reactions on ^{93}Nb and ^{93}Zr, respectively. The experimental data are plotted as open circles and triangles for the ^{93}Nb and ^{93}Zr data, respectively. We focus on the production of isotopes with the magic number $N = 50$. Jumps are clearly seen at $N = 50$ in the experimental production cross sections for both the $(p, 2pxn)$ data, namely, for ^{90}Zr in panel (b) and ^{89}Y in panel (d). However, such a jump is not observed in the production of ^{91}Nb with $N = 50$ from the ^{93}Nb(p, pxn) reactions shown in panel (a), whereas a jump does appear at $N = 50$ in the ^{93}Zr(p, pxn) reactions shown in panel (c).

On the basis of a theoretical model calculation, we can now discuss the reason why the jump disappears at $N = 50$ in panel (a). In Fig. 2.24, the production cross sections calculated with PHITS are decomposed into two components, namely, the INCL and GEM components. The former, shown by the red dash-dotted line, represents the direct production yield via the INC process, *i.e.*, the formation of pre-fragments having excitation energies lower than the particle-emission threshold energies followed by sequential de-excitation by γ ray emission. Conversely,

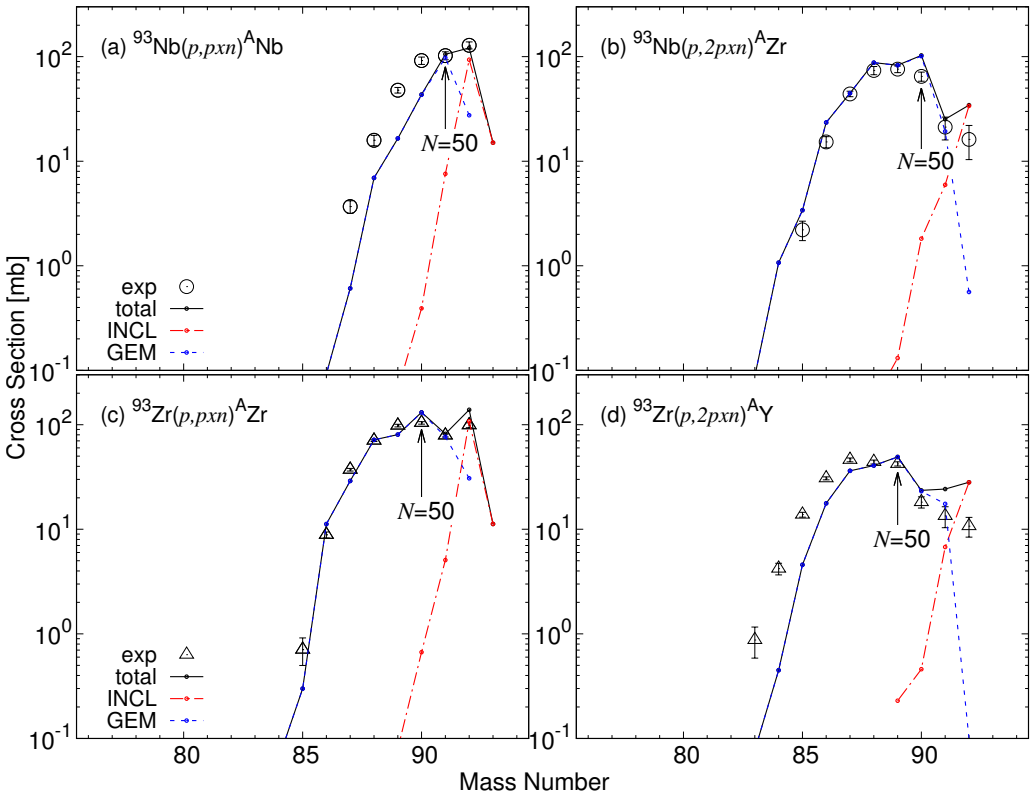

Figure 2.24: Isotope-production cross sections for the (p, pxn) and $(p, 2pxn)$ reactions on ^{93}Nb and ^{93}Zr. The calculated results denoted by the black solid lines are decomposed into two components: the production of isotopes via just the INC process described by INCL4.6 (red dashed-dotted line) and that via the sequential evaporation process described by GEM (blue dashed-line).

the GEM component shown as the blue dashed-line corresponds to the production of isotopes by particle evaporation from highly excited pre-fragments generated after the INC process. The INCL components look similar for both the ^{93}Nb and ^{93}Zr target nuclei, and they have no jump at the magic number $N = 50$, with the maximum values at $A = 92$ corresponding to one-nucleon removal from the target nuclei. In contrast, the GEM component shows a maximum production yield in each isotopic distribution at $N = 50$, and a jump in the production cross section appears in all the panels. When one compares the sum of the INCL and GEM components, which are in reasonable agreement with the measured data, the jump seen at $N = 50$ in the GEM component of the ^{93}Nb(p, pxn) reaction is smeared out by the INCL component and disappears, as shown in panel (a). Thus, it was

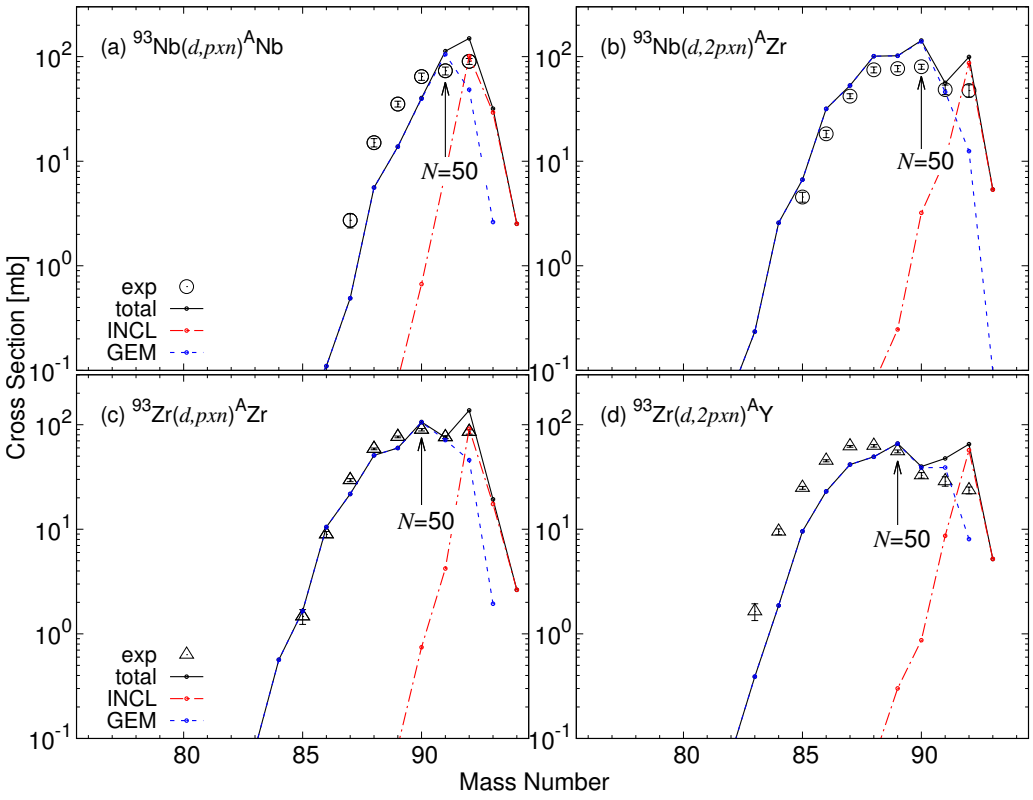

Figure 2.25: Same as Fig. 2.24, but for the (d, pxn) and $(d, 2pxn)$ reactions on ^{93}Nb and ^{93}Zr.

found that the appearance of the jump in the isotopic distribution depends on the relative fraction of INCL and GEM components in the isotope production. For the other reactions, the INCL components do not disturb the jumps seen in the GEM components, because the mass number corresponding to $N = 50$ occurs far from $A = 92$, where the INCL component provides the maximum value. Thus, the effects of the closed neutron shell on isotope production appear in all three cases.

Comparisons of the d-induced reactions on ^{93}Nb and ^{93}Zr are shown in Fig. 2.25. The same result as for the p-induced spallation reaction is obtained, and the effect of neutron-shell closure at $N = 50$ in the d-induced spallation reactions can be interpreted in the same manner as for the p-induced ones.

Finally, the measured element-production cross section for ^{93}Nb and ^{93}Zr are plotted as a function of the change in atomic number ΔZ by the black circles and the red triangles in Fig. 2.26 in order to see how the difference of a single nucleon in the initial proton and neutron numbers influences the measured distributions.

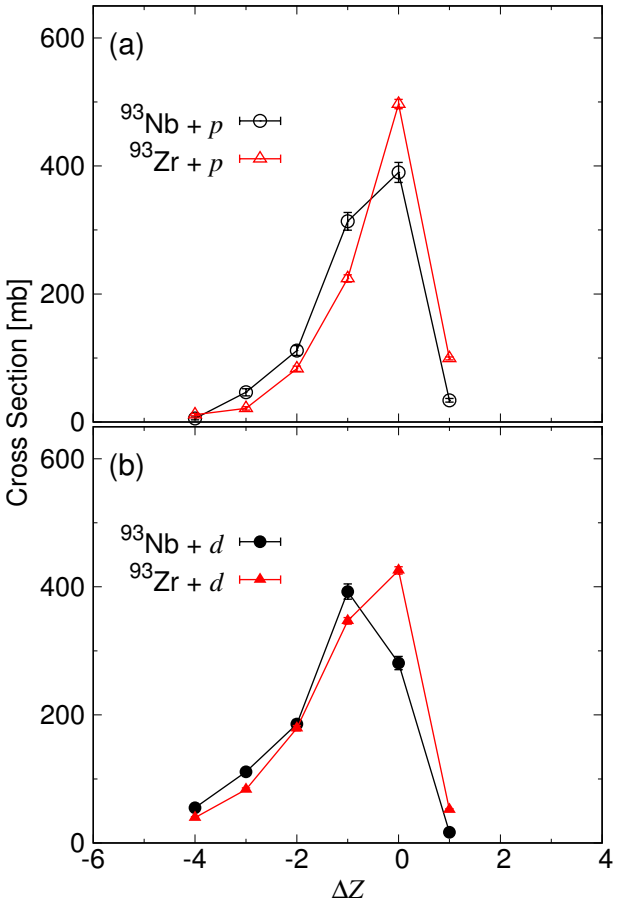

Figure 2.26: Distribution of production cross sections as a function of the change in atomic number ΔZ (a) for p-induced reactions on ^{93}Nb and ^{93}Zr and (b) for d-induced reactions.

Panels (a) and (b) present the p- and d-induced reactions, respectively. In panel (a), the ΔZ distribution of the p-induced reactions on ^{93}Zr shows a sharp peak at $\Delta Z = 0$, whereas a broader peak is observed in the ΔZ distribution for ^{93}Nb, resulting in a smaller cross section at $\Delta Z = 0$ and a larger cross section at $\Delta Z = -1$ than in the ^{93}Zr data. This difference in the ΔZ distribution can be explained by the difference in proton and neutron separation energies between the Nb and Zr isotopes. In Fig. 2.27 (a), the calculated branching ratios for the proton and neutron emission from excited Nb and Zr isotopes generated by the INC process at 15, 35, and 55 MeV are shown as black and red lines, respectively. The niobium isotopes have larger proton emission probabilities than the Zr isotopes at all excitation energies. This tendency originates from the proton and neutron separation energies for each isotope. In Fig. 2.27 (b), the separation energies S_p and S_n

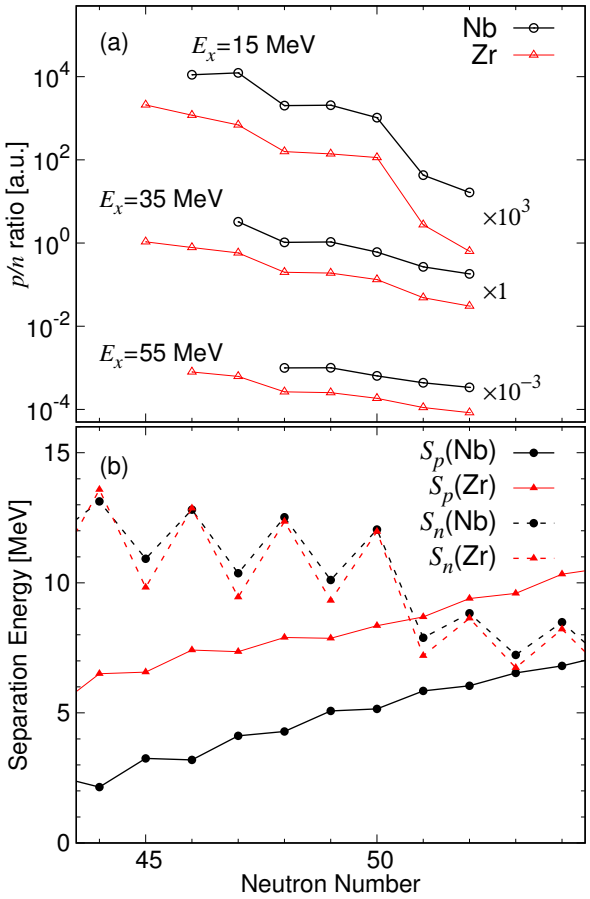

Figure 2.27: (a) The branching ratios for proton and neutron emission from excited Nb and Zr isotopes, and (b) the separation energies of protons and neutrons from Nb and Zr isotopes, both as a function of neutron number.

calculated from the mass table AME2016 [67] are shown as a function of neutron number by the solid and dashed-lines, respectively. Both the Nb and Zr isotopes have almost the same S_n, whereas S_p has a gap of approximately 5 MeV because of sub-shell closure at $Z = 40$. The different behaviors of S_n and S_p enhance the proton emission from each excited Nb pre-fragment generated by the INC process compared with the Zr isotopes. As a result, it is expected that the ΔZ distribution for ^{93}Nb spreads toward smaller ΔZ.

Figure 2.26 also compares the change ΔZ produced by p- and d-induced reactions on ^{93}Nb and ^{93}Zr. The production cross sections for the d-induced reactions are larger in the small ΔZ region than are those of the p-induced reactions. Since incident deuterons have twice the kinetic energy of protons, the pre-fragments generated via the INC stage have higher excitation energies than those produced

by p-induced reactions. The higher excitation energy allows the pre-fragments to emit more particles including protons in the evaporation stage. Thus, it is expected that the distributions are shifted to lower ΔZ. In addition, the neutron contained in the deuteron may affect the shift of the distribution to low ΔZ in the d-induced reactions. Since the $n-p$ scattering cross section is larger than the $p-p$ scattering one, an incident deuteron is more likely to knock out protons of a target nucleus in the INC process than is an incident proton. As a result, the ΔZ distributions of the d-induced reactions are broader than the p-induced ones in both of the ^{93}Nb and ^{93}Zr data.

2.5 Conclusion

The isotope-production cross sections in p-, d-, and C-induced reactions on ^{93}Nb at 113 MeV/nucleon were measured using the inverse-kinematics method. The measured data were compared with the available activation data, the theoretical calculations by reaction models implemented in PHITS, CCONE, and the latest nuclear data libraries (JENDL-4.0/HE, JENDL/ImPACT-2018, TENDL-2017, and ENDF/B-VIII.0). Moreover, the p- and d-induced production cross sections on ^{93}Nb were compared with the data of ^{93}Zr that is one of LLFPs and a neighboring isobar of ^{93}Nb in order to investigate how the neutron shell closure with the magic number 50 affects the isotopic distribution of production cross sections.

First, we found that within the experimental uncertainties the measured production cross sections for ^{90}Mo, ^{90}Nb, and ^{86,88}Y produced by p-induced reactions on ^{93}Nb are in fairly good agreement with those measured by the activation method. This confirms the consistency between the isotope-production cross sections measured by the two different methods. It should be emphasized that the inverse-kinematics method is suitable for the investigation of isotope production over a wide range of mass numbers, including stable isotopes, compared with the conventional activation method.

Second, we benchmarked the reaction models implemented in PHITS and the nuclear data libraries by comparisons with the measured isotope-production cross sections. The model calculations with INCL4.6/GEM showed generally good agreement with the experimental data for the p- and d-induced reactions, although some discrepancies were seen, *e.g.*, the overestimate of ^{92}Mo production and the exaggerated even-odd staggering in the calculated isotopic distributions. Noticeable jumps seen in the measured production cross sections for ^{90}Zr and ^{91}Zr were reproduced by the PHITS calculations reasonably well. The CCONE calculation showed the best reproducibility for p-induced reaction among the models and the libraries. For the C-induced reactions on ^{93}Nb, we compared model calculations using both JQMD/GEM and JQMD-2.0/GEM with the measured data.

The underestimate of ^{91,92}Nb seen in the JQMD/GEM calculation was considerably improved in the JQMD-2.0/GEM calculations due to the improved treatment of peripheral collisions in JQMD-2.0. However, neither calculation reproduced very well the charge-exchange reaction leading to the production of Mo isotopes. From comparisons with the four nuclear data libraries, we found that JENDL-4.0/HE is in better agreement with the experimental data than JENDL/ImPACT-2018, TENDL-2017, or ENDF/B-VIII.0.

Third, we compared the measured ^{93}Nb data to the ^{93}Zr data, with particular attention to the effect of neutron-shell closure on the isotopic distribution of production cross sections. We observed noticeable jumps at the neutron number $N = 50$ in the Zr and Y isotopes produced by the p- and d-induced reactions on ^{93}Zr. In contrast, although such a jump was clearly seen at $N = 50$ in the Zr isotopes produced by the p- and d-induced reactions on ^{93}Nb, it disappeared in the Nb isotopes produced by the same reactions. Our INCL4.6/GEM calculations showed that the isotopes with removal neutron numbers $\Delta N = 1$ and 2 are produced mainly by the INC process, whereas the jump at $N = 50$ appears in the isotopic distribution formed by evaporation from the excited pre-fragments generated by the INC process. This indicates that the appearance of the jump in the isotopic distribution depends on the relative fractions of the INC and evaporation components in the isotope production. We have thus clarified that the jump formed in the evaporation process is smeared out by the INC component in the production of ^{91}Nb by the $(p, p2n)$ and $(d, d2n)$ reactions on ^{93}Nb. Moreover, we compared the production cross sections obtained as a function of the change in atomic number ΔZ (*i.e.*, the removal number of protons) for the p- and d-induced reactions on ^{93}Nb and ^{93}Zr. The ΔZ distributions showed that the production cross sections with $\Delta Z = 0$ for ^{93}Nb are smaller than those for ^{93}Zr for both the p- and d-induced reactions, whereas those with $\Delta Z = 1$ for ^{93}Nb are larger than those for ^{93}Zr. These differences can be explained by the difference in the proton and neutron separation energies of the Zr and Nb isotopes. That is, the proton-separation energies of the Nb isotopes with $Z = 41$ are much smaller than those of the Zr isotopes with $Z = 40$, resulting predominantly in proton emission from the excited Nb isotopes generated by the INC process.

3 Isotope Production in Proton- and Deuteron-Induced Reactions on ^{93}Zr at 50 MeV/nucleon

3.1 Introduction

As mentioned in Chapter 1, isotope-production cross sections in p- and d-induced reactions at energies of 105 [44] and 209 MeV/nucleon [45] have previously been measured. Using the measured data for these cases, theoretical-model analyses with the intranuclear cascade and evaporation models have been performed. As a next step, we intend to investigate the incident-energy dependence of the isotopic distribution of production cross sections by further measurements in the lower-incident-energy region at which the spallation reaction is no longer dominant. Therefore, isotope-production cross sections for ^{93}Zr were newly measured at reaction energies of approximately 50 MeV/nucleon using the inverse-kinematics method in order to investigate how the isotopic distribution changes with the reaction energy. The measured cross sections are compared with those measured previously at 105 and 209 MeV/nucleon, and the incident-energy dependence of the isotopic distributions is discussed. In addition, theoretical-model calculations using INCL4.6/GEM [53, 54] implemented in PHITS [48, 49], CCONE code [55], and INCL++/ABLA07 [77, 78] are compared with the measured data for benchmarking of the models in the low-incident-energy region. Recently, the newly evaluated nuclear data library JENDL/ImPACT-2018 [68], developed as a part of the ImPACT Program, has been released as a special purpose file for nuclear transmutation of LLFPs. The experimental ^{93}Zr data are useful for checking the performance of JENDL/ImPACT-2018.

3.2 Experiment

The experiment was performed at the RIKEN RIBF using a cocktail beam including a ^{93}Zr secondary beam with a kinetic energy of approximately 50 MeV/nucleon,

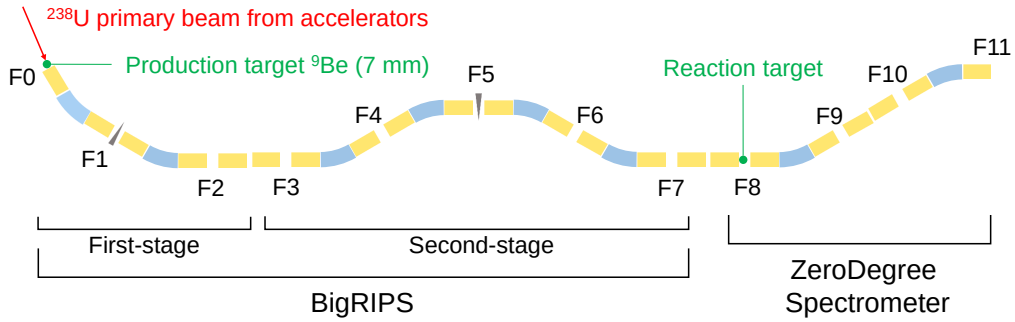

Figure 3.1: Schematic view of BigRIPS and the ZeroDegree Spectrometer used in the experiment for ^{93}Zr.

paying attention to charge-state changes due to relatively low incident energy. Since the experimental procedure and setup were similar to that for ^{93}Nb as described in Sec. 2.2, we focus on the differences from that experiment and on the essence of this experiment. In this experiment, a ^{238}U primary beam accelerated up to 345 MeV/nucleon impinged onto a 7-mm-thick ^{9}Be primary target installed at the entrance of BigRIPS. RILAC, RRC, fRC, IRC, and SRC were used to accelerate the ^{238}U primary beam. The secondary beam containing ^{93}Zr ions was produced through in-flight fission of the ^{238}U primary beam, and separated and identified by using BigRIPS. Then the secondary beam impinged onto the secondary target, cooled gaseous H_2 and D_2 [79], located at the entrance of the ZDS. The residual nuclei produced by nuclear reactions with the secondary targets were also identified at ZDS to derive the isotope-production cross section. In this section, the basic setup of BigRIPS and ZDS, as well as the setups of the beamline detectors, secondary targets, and DAQ system are introduced.

3.2.1 Basic Setup and Experimental Procedure

The BigRIPS [14] and the ZDS [14] were used to analyze the incident ^{93}Zr beam and the reaction products in this experiment, respectively. The schematic view of the beamline is displayed in Fig. 3.1, which is almost the same as Fig. 2.1, but the thicknesses of the primary targets are not equal. The yellow blocks, the blue blocks, and the symbols F respectively indicate the STQ magnets, the D magnets, and the focal planes at which slits, degraders, beamline detectors, and targets are placed. The secondary beam was produced and separated in the first stage of BigRIPS and identified in the second stage. The magnetic fields of D magnets and apertures of the slits optimized for the production of ^{93}Zr are listed in Tables. 3.1 and 3.2, respectively. Moreover, the geometries of wedge-shaped aluminum degraders for purifying the secondary beam are listed in Table. 3.1. To limit the momentum

Table 3.1: Apertures of slits and geometries of degraders.

Focal Plane	Slit [mm]	Degrader [mm, mrad]
F1	L: −5.00, R: 5.00	thickness: 5, angle: 5.986
F2	L: −2.00, R: 2.00	-
F5	L: −5.00, R: 5.00	thickness: 0.5, angle: 2.36
F7	L: −7.00, R: 3.00	-

Table 3.2: Magnetic fields at each section of BigRIPS.

Section	$B\rho$ [Tm]
F0 - F1	4.8921
F1 - F3	3.2833
F3 - F5	3.1862
F5 - F7	2.7515

spread, the aperture of the F1 slit was set to be ±5 mm, corresponding to a momentum spread of ±0.5%. The secondary beam impinged onto the secondary target at F8. The reaction products were analyzed using ZDS. We predict that changes in the charge-state are more serious in the 50-MeV/nucleon experiment. In this experiment, therefore, we put no detectors at F9 to avoid complicated charge-state changes at the intermediate focal plane in ZDS. ZDS was operated in dispersive mode, where the final focal plane (F11) is a dispersive focal plane used to extract momentum information from the horizontal position at F11. In the dispersive mode, the momentum acceptance of ZDS is limited to less than ±2%. Seven different magnetic-field settings $\Delta(B\rho)/B\rho = -6\%$, -4%, -2%, 0%, +2%, +4%, and +6% were adopted to measure a wide range of mass numbers and charge states of reaction products. The typical current of the primary beam was approximately 400 enA.

3.2.2 Beamline Detectors

In this experiment, plastic scintillators (PLs), double-PPACs, and energy loss at the F5 energy degrader were used to identify the secondary beam via the TOF$-B\rho-\Delta E$ method. By contrast, PLs, double-PPAC, and the newly developed MUSIC were used to identify the reaction products via a similar method. The list of detectors used and their locations are shown in Table. 3.3.

Table 3.3: Beamline detectors used for particle identification.

Focal Plane	Detector
F3	Plastic scintillator, double-PPAC×2
F5	Plastic scintillator, double-PPAC×2
F7	Plastic scintillator, double-PPAC×2
F8	Plastic scintillator, double-PPAC×3
F11	Plastic scintillator, double-PPAC×2, MUSIC

Table 3.4: Dimensions of the plastic scintillators.

Focal Plane	Thickness [mm]	Active Area [mm^2]
F3	0.2	120(W) × 100(H)
F5	0.2	120(W) × 100(H)
F7	0.2	120(W) × 100(H)
F8	0.1	120(W) × 100(H)
F11	0.1	240(W) × 150(H)

Plastic Scintillator

The plastic scintillators were installed at F3, F5, F7, F8, and F11 in order to measure the TOF. Two PMTs were connected to both sides of each scintillator except that a F11 to determine the timing at which beam passes through them. In contrast, we used a larger plastic scintillator at F11 to cover a wider region. For the F11PL, four PMTs were connected to the scintillator, as shown in Fig. 3.2. The dimensions of the plastic scintillators are summarized in Table. 3.4. The signal from the PMT was divided into two signals. One was sent to charge ADC module and the other was sent to TDC module after discrimination by a constant fraction discriminator.

Double-PPAC

The double-PPACs were installed at F3, F5, F7, F8, and F11 for trajectory reconstruction. As mentioned in Sec. 3.2.1, we did not use a PPAC at F9 in order to simplify analysis of charge-state changes. Moreover, an additional double-PPAC was placed at F8 for more precise position determination around the secondary target. In the present experiment, PPACs were filled with C_3F_8 gas at a pressure of 30 Torr and their active areas are 240(W) × 150(H) mm^2. The signals from the electrodes were amplified by a fast timing amplifier, discriminated by a constant fraction discriminator, and sent to the TDC module.

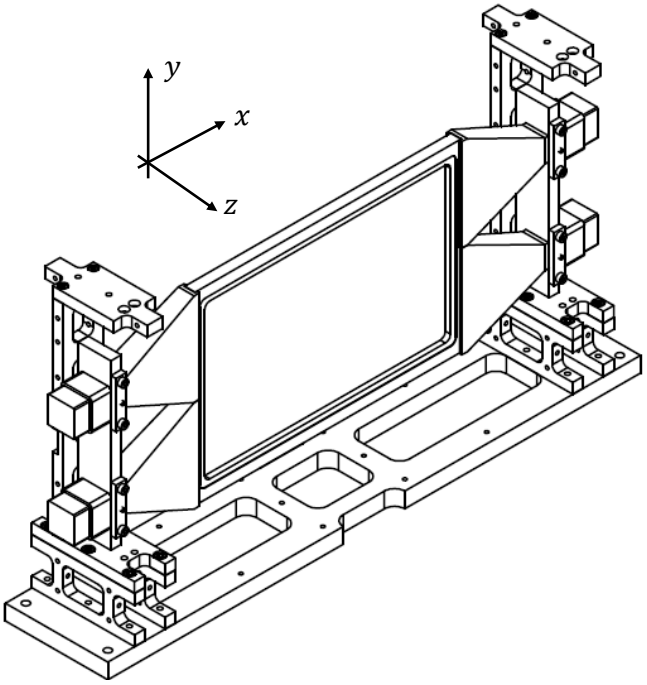

Figure 3.2: Schematic view of the plastic scintillator placed at F11. The z axis corresponds to the beam direction.

New-MUSIC

The newly developed MUSIC (New-MUSIC) was installed at F11 to measure the energy loss ΔE and total kinetic energy E. Its read-out electrodes are segmented into 30 triangular pads with a backgammon structure, as shown in Fig. 3.3. New-MUSIC provides 30 signals, which reflect the energy loss of the reaction product in each segmented pad. The difference of the signal magnitudes between two pads gives the horizontal position of the incident beam. The total energies of the reaction products were measured by stopping the reaction products in the New-MUSIC chamber to identify their charge states. This chamber has a sufficiently large active volume of 260(W) $\times$ 170(H) $\times$ 757(D) mm^3 to stop the reaction products and obtain Bragg peaks. The New-MUSIC was filled with P10 gas (Ar(90%) + CH_4(10%)) at a pressure of 765 Torr. The signals were gained by a preamplifier and a spectroscopy amplifier, then sent to charge ADC module.

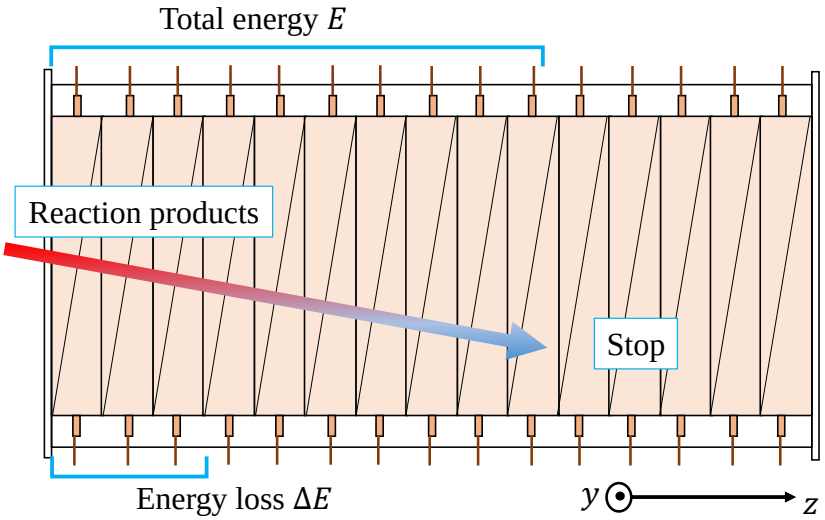

Figure 3.3: Schematic view of New-MUSIC with its 30 backgammon-structured triangular read-out pads. The reaction products stop in New-MUSIC to simultaneously measure both the total kinetic energy and the energy loss.

3.2.3 Secondary Targets

The secondary targets were placed at F8. In this experiment, cooled gaseous H_2 (22.6 mg/cm^2) and D_2 (34.5 mg/cm^2) were used as secondary targets to reduce the energy loss at the secondary target for measurements of the p- and d- induced reactions. A schematic view of the cooling system is shown in Fig. 3.4, quoted from Ref. [79]. Note that Fig. 3.4 presents the liquid-helium target, and the "He GAS CYLINDER" is replaced by the H_2 and D_2 gas cylinders for this experiment. Hydrogen and deuterium were packed in the cylindrical cell with a diameter of 30 mm [79] at pressures of 4,100 and 3,960 hPa, and cooled to 32.71 and 36.00 K, respectively. The window of the target cell was made of havor foil with the thickness of 6 μm. The fluctuation of the pressure and temperature were monitored during the experiment. The fluctuation of the pressure was $\pm$10 hPa for H_2 and $\pm$30 hPa for D_2. That of the temperature was $\pm$0.07 K for H_2 and $\pm$0.06 K for D_2. An empty-cell run was also performed to subtract background contributions from beamline materials.

3.2.4 Trigger

The trigger was generated by coincidence of signals from both sides of the PMTs connected to F7PL. In contrast to the experiment for ^{93}Nb, only one trigger setting

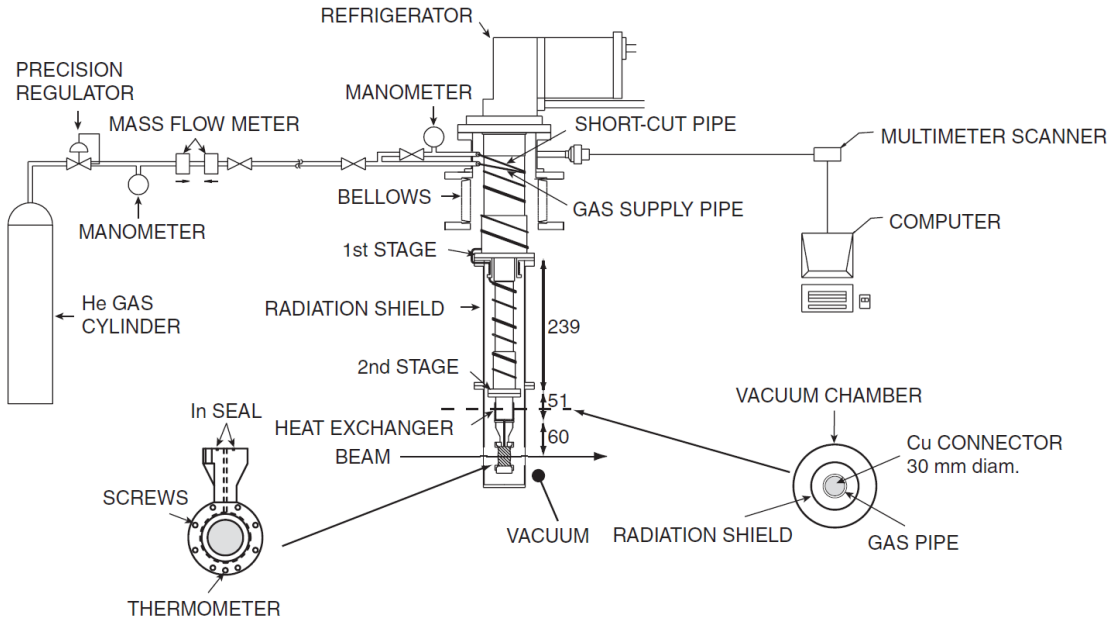

Figure 3.4: Schematic view of the target system quoted from Ref. [79].

was adopted in this experiment, because count rates were almost the same under all settings due to the charge-state-changed incident ^{93}Zr beam.

3.3 Data Analysis

In this section, we focus on analysis of the measured data. First, analysis of each beamline detector and particle identification based on the TOF$-B\rho-\Delta E$ method with Eqs. (2.2), (2.3), and (2.4) are introduced. Then, some corrections for the yields of the reaction products, the derivation of isotope-production cross section, and the evaluation of systematic uncertainty are described.

3.3.1 Data Analysis of Beamline Detectors

Plastic Scintillator

The plastic scintillators provided charge and timing information corresponding to the incident particles. Raw timing data were calibrated from the output channel into actual timing information. The calibration parameters were determined by a measurement with a TDC Calibrator. For all plastic scintillators except F11PL, the calibrated timings from two PMTs were averaged to cancel out the position dependence. For F11PL, four calibrated signals were averaged to cancel out the

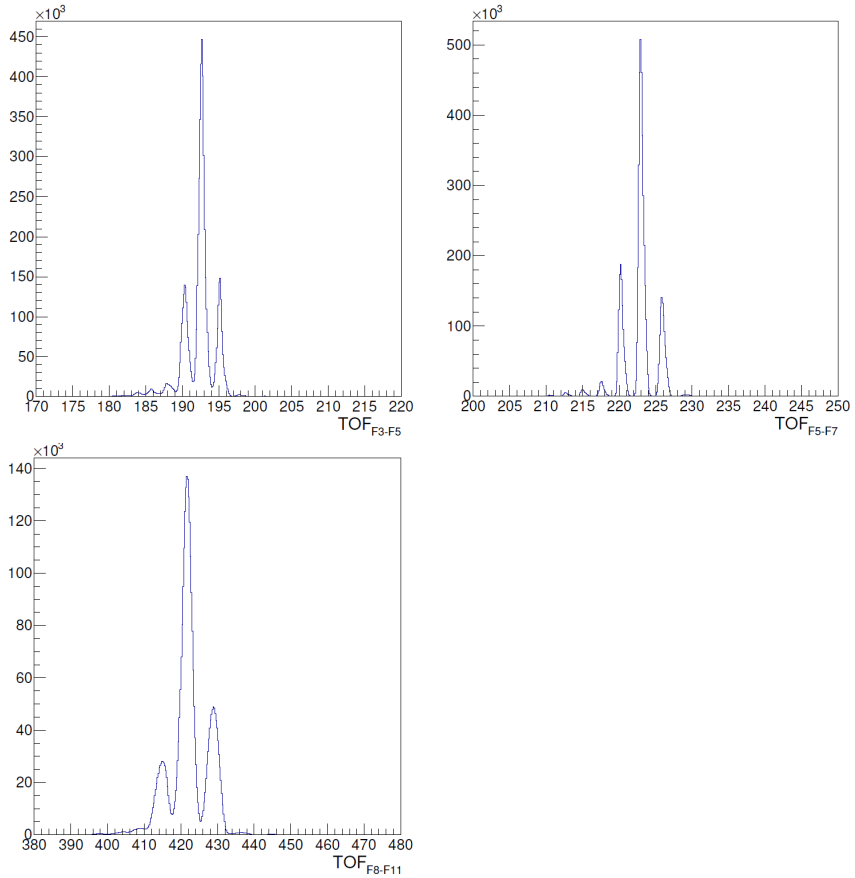

Figure 3.5: Distributions of the time-of-flight (TOF) between F3 and F5 (Upper Left), F5 and F7 (Upper Right), and F8 and F11 (Lower Left).

position dependence. The TOFs between F3 and F5, F5 and F7, and F8 and F11 were calculated using the timing information from each plastic scintillator, as shown in Fig. 3.5. Some sharp peaks observed in $\mathrm{TOF_{F3-F5}}$ and $\mathrm{TOF_{F5-F7}}$ correspond to individual isotopes, as explained in Sec. 2.3.1. These peaks were smeared out by the beamline materials and the broader peaks were observed in $\mathrm{TOF_{F8-F11}}$.

Double-PPAC

The analysis of PPAC was almost the same as that for ^{93}Nb. First, the vertical and horizontal positions at each PPAC were calculated based on the difference in the timing information between two read-outs of a cathode. Using four pairs of vertical and horizontal positions with valid TSumX/Y values, trajectory reconstruction was performed to obtain the position and angle at the focal plane. With

Table 3.5: Matrix elements used in $B\rho$ derivation.

Section	$(x\|x)$	$(x\|a)$ [mm/mrad]	$(x\|\delta)[\%/mm]$
F3−F5	0.92659	-0.004712	31.6690
F5−F7	1.08043	0.022634	-34.1741
F8−F11	0.99690	0.142275	40.6112

this trajectory and transport matrix, the magnetic rigidity $B\rho$ for the beam was obtained. Matrix elements used in the calculation of $B\rho$ are listed in Table. 3.5.

New-MUSIC

The New-MUSIC provided 30 charge signals corresponding to the energy loss in each pad. For the calibration, ^{126}Sn at 200 MeV/nucleon data was used because the ^{93}Zr beam at 50 MeV/nucleon stopped in the New-MUSIC and thus did not deposit its energy to all of the pads. Since New-MUSIC has a backgammon structure, we extract the beams passing through the center of New-MUSIC for calibration to remove the position dependence. Moreover, the horizontal position at F9 was limited to remove charge-state-changing events. Note that double-PPACs were installed at F9 in ^{126}Sn measurement. The conditions of the ^{126}Sn beam used for the calibration were as follows:

- -10 $< x_{\mathrm{F9}}$ [mm] < 10
- -5 $< x_{\mathrm{F11}}$ [mm] < 5
- -5 $< y_{\mathrm{F11}}$ [mm] < 5
- -0.001 $< a_{\mathrm{F11}}$ [mrad] < 0.001
- -0.001 $< b_{\mathrm{F11}}$ [mrad] < 0.001

Under these conditions, the averaged output channels for ^{127}Sb, ^{126}Sn, and ^{125}In were compared to the energy loss calculated by LISE++ [62] in each pad. From these three points and a pedestal assumed to have an energy loss of 0 MeV, linear functions for calibration were derived by the fitting for each pad. Figure 3.6 shows the calibrated energy loss as a function of pad number and of layer number in the case of a ^{93}Zr beam at 50 MeV/nucleon and 0% ZDS $B\rho$ setting with an H_2 target. Note that the layer refers to the sum of the two neighboring triangular pads. The energy loss for each pad has two main components: one component consists of F.S. events that pass through the center of New-MUSIC, and the other consists of H-like events that pass the high-momentum side. The energy loss of F.S. events shows a smooth curve. By contrast, H-like events lost their energy alternating

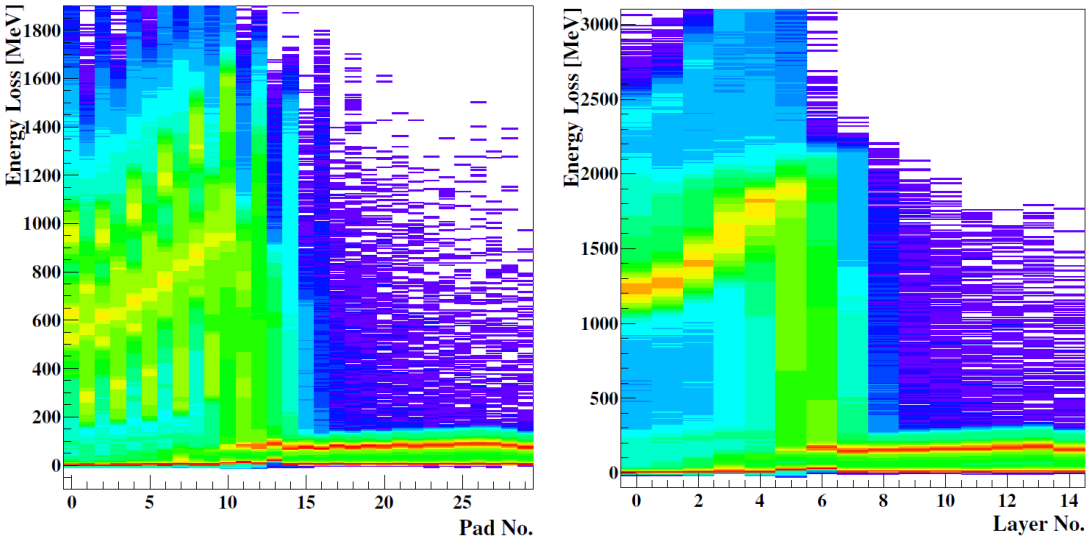

Figure 3.6: Energy loss of the ^{93}Zr beam at New-MUSIC as functions of pad number (Left) and layer number (Right) in an H_2 target with a 0% ZDS $B\rho$ setting.

between large and small, as seen in Fig. 3.6, because the particles in H-like case have different path lengths in each pad. The energy loss as a function of each layer has a smooth Bragg curve, even for H-like events, because the position dependence is canceled out.

To determine how many layers to use for the ΔE calculation, we checked $\Delta E - E$ correlation for some ΔE cases after selecting the ^{93}Zr beam. Figure 3.7 shows the correlation plots between ΔE and E in the case of the ^{93}Zr beam with an H_2 target and a -4% ZDS $B\rho$ setting. The energy losses ΔE_1, ΔE_2, ΔE_3, and ΔE_4 were calculated as the averaged energy loss of the first one, two, three, and four layers, respectively. The linear correlation in the low-E region corresponds to the stopped events upstream of the layer used for ΔE calculation. The stopping ratios were calculated from the number of total events and stopping events as 0.84% for ΔE_1, 5.07% for ΔE_2, 32.07% for ΔE_3, and 71.33% for ΔE_4. Upstream of the third layer, 32.07% of the beam was stopped, which is more events than expected. Thus, we used ΔE_2 for particle identification of the reaction products. In the following analysis, the stopped 5.07% events were removed and their yields are compensated in the following corrections, as explained in Sec. 3.3.3.

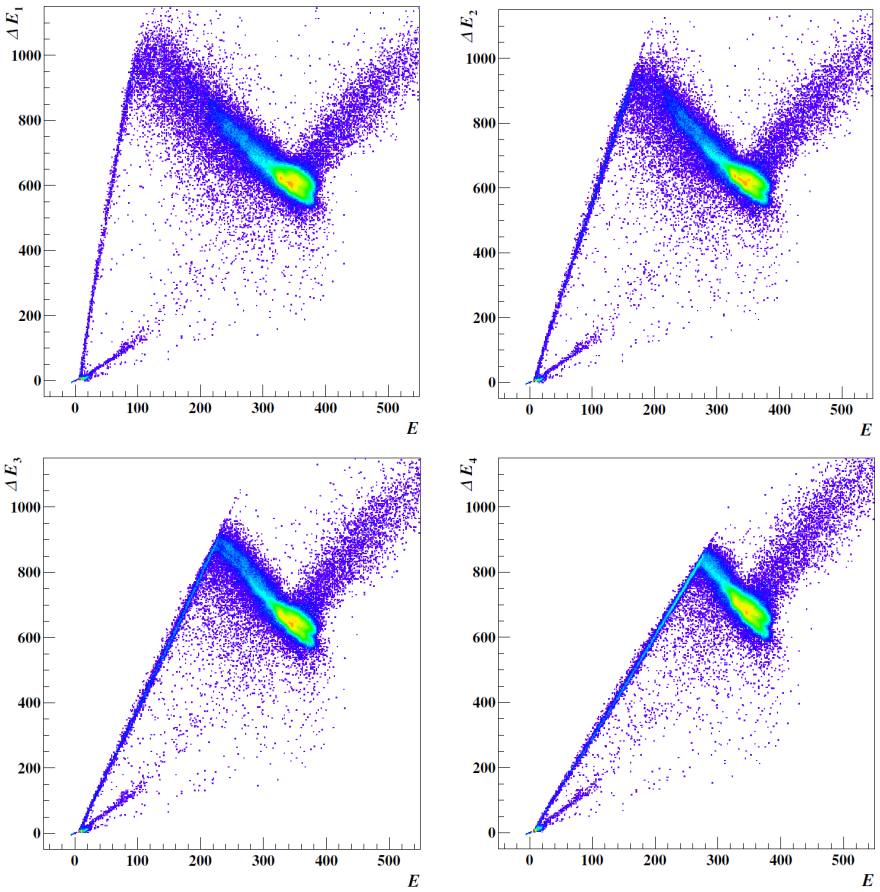

Figure 3.7: Two-dimensional plot of energy loss ΔE and total kinetic energy E in the case of an H_2 target with a -4% ZDS $B\rho$ setting after selecting the ^{93}Zr beam. The averaged energy losses with one (Upper Left), two (Upper Right), three (Lower Left), and four (Lower Right) layers are used.

3.3.2 Particle Identification

In this subsection, we explain the analytical procedure for particle identification. The procedure for the reaction products is almost the same as that explained in Sec. 2.3.2, but that for the secondary beam differs because we did not use MUSIC at F7.

Particle Identification of the Secondary beam

From the aforementioned analyses, the TOFs and $B\rho$ for the F3−F5 and F5−F7 sections were obtained. We derived the ΔE of the secondary beam from the energy loss in the energy degrader at F5 under the assumption of no change in Z and A

at F5. The energy loss in the degrader at F5 (dE/dx) can be expressed as:

$$\frac{dE}{dx} \simeq \frac{1}{t}\left(E_{\rm in} - E_{\rm out}\right), \tag{3.1}$$

where t, $E_{\rm out}$, and $E_{\rm in}$ indicate the path length in the energy degrader, and the total energies at downstream and upstream of the energy degrader, respectively. Here, the path length of a particle with an incident angle of a and horizontal position x in a wedge-shaped energy degrader with angle θ and thickness at the center of degrader l is described as:

$$t \simeq l + \frac{x\tan\left(\theta\right)}{\cos\left(a\right)}. \tag{3.2}$$

The total energies are calculated as $E = A\gamma m_u c^2$. From Eq. (2.3), $A\gamma m_u$ is proportional to $B\rho Q/\beta$, then:

$$\frac{dE}{dx} \propto \frac{1}{t}\left\{\frac{B\rho_{\rm in}\left(Z - e_{\rm in}\right)}{\beta_{\rm in}} - \frac{B\rho_{\rm out}\left(Z - e_{\rm out}\right)}{\beta_{\rm out}}\right\}, \tag{3.3}$$

where e represents the number of electrons. Then, using Eq. (2.4), Z is proportional to dE/dx as:

$$Z^2 \propto \beta^2\frac{dE}{dx} \simeq \frac{\beta^2}{t}\left\{\frac{B\rho_{\rm in}\left(Z - e_{\rm in}\right)}{\beta_{\rm in}} - \frac{B\rho_{\rm out}\left(Z - e_{\rm out}\right)}{\beta_{\rm out}}\right\}. \tag{3.4}$$

Assuming that Eq. (3.4) is a quadratic equation of Z, Z can be calculated as:

$$\begin{aligned} Z \simeq{}& \frac{1}{2}C\frac{\beta^2}{t}\left(\frac{B\rho_{\rm in}}{\beta_{\rm in}} - \frac{B\rho_{\rm out}}{\beta_{\rm out}}\right) \\ &+\sqrt{\frac{\beta^4}{4t^2}C^2\left(\frac{B\rho_{\rm in}}{\beta_{\rm in}} - \frac{B\rho_{\rm out}}{\beta_{\rm out}}\right)^2 - \frac{\beta^2}{t}C\left(\frac{B\rho_{\rm in}e_{\rm in}}{\beta_{\rm in}} - \frac{B\rho_{\rm out}e_{\rm out}}{\beta_{\rm out}}\right)}, \end{aligned} \tag{3.5}$$

where C indicates a constant value. In the present experiment, the charge state of the ^{93}Zr beam was H-like between F3 and F5, and F.S. between F5 and F7. For β^2 in Eq.(3.5), $\beta^2_{\rm out}$ was used because of better separation of Z.

On the other hand, A/Q was calculated from $B\rho_{\rm out}$ and $\beta_{\rm out}$. Figure 3.8 shows a two-dimensional identification plot for the secondary beam by the atomic number Z and the mass-to-charge ratio A/Q. The secondary beam includes just one isotone, as seen in Fig. 3.8. As with the isomer tagging in Sec. 2.3.2, two γ rays with 315 and 492 keV from ^{92m}Y were used to verify the absolute Z and A/Q values. Each nuclide was clearly separated with resolutions of 0.45 (FWHM) in Z and 0.28 (FWHM) in A, which are sufficient to identify the ^{93}Zr beam. The

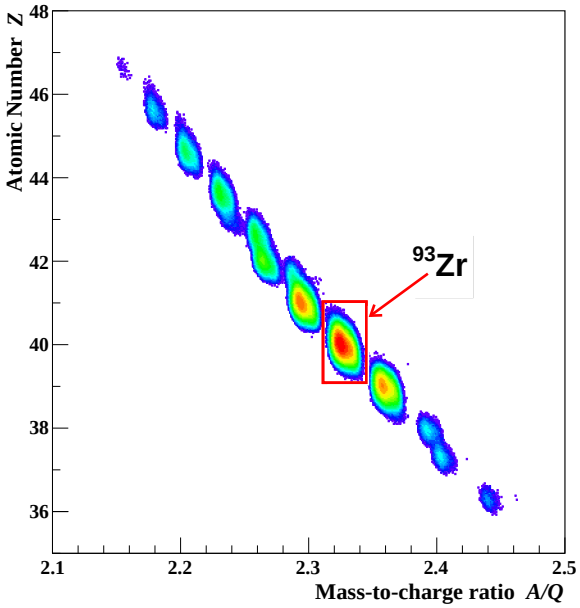

Figure 3.8: Particle identification plot for the secondary beam. The red box outlines the ^{93}Zr beam.

events in the ranges $39.6 \leq Z \leq 40.4$ and $2.319 \leq A/Q \leq 2.333$ were selected as the ^{93}Zr beam. The purity, which is calculated as the ratio of the number of ^{93}Zr beam in the red box and the number of total events, and typical count rate of ^{93}Zr were 57.8% and 980 count per second, respectively. The energy of the ^{93}Zr beam was calculated as 51 and 52 MeV/nucleon at the centers of the H_2 and D_2 targets, respectively, from $B\rho_{\mathrm{F5-F7}}$ considering the energy loss in materials placed between F7 and the secondary target (as listed in Table 3.6) using the LISE++ code [62]. The energy spreads in the secondary targets were calculated as ±10 MeV/nucleon.

Particle Identification of the Reaction Products

Particle identification of the reaction products was performed based on the TOF$-B\rho-\Delta E$ method. Similar to the A/Q of the secondary beam, the A/Q of the reaction products was calculated from $B\rho_{\mathrm{F8-F11}}$ and $\beta_{\mathrm{F8-F11}}$. The obtained A/Q was corrected by the positions and angles mentioned in Sec. 2.3.2 to achieve a higher A/Q resolution. The atomic number Z was calculated from $\beta_{\mathrm{F8-F11}}$ and ΔE_2 based on Eq. (2.4). Figure 3.9 represents the identification plot for the reaction products from the H_2-reaction target at the 0% ZDS $B\rho$ setting after selecting the

Table 3.6: Beamline materials placed between F7 and the secondary target.

Material	Composition	Thickness [mg/cm^2]
F7PPAC1	Mylar foil ($H_8C_{10}O_4$)	6.23
F7PPAC2	Mylar foil ($H_8C_{10}O_4$)	6.23
F7PL	Polyethylene ($H_{10}C_9$)	20.64
F8PPAC1	Mylar foil ($H_8C_{10}O_4$)	6.23
F8PPAC2	Mylar foil ($H_8C_{10}O_4$)	6.23
F8PL	Polyethylene ($H_{10}C_9$)	10.32
Heat Shield	Al	2.70
Target Cell Window	Harvar foil ($Co_{42}Cr_{20}Ni_{13}Fe_{19}W$)	4.98

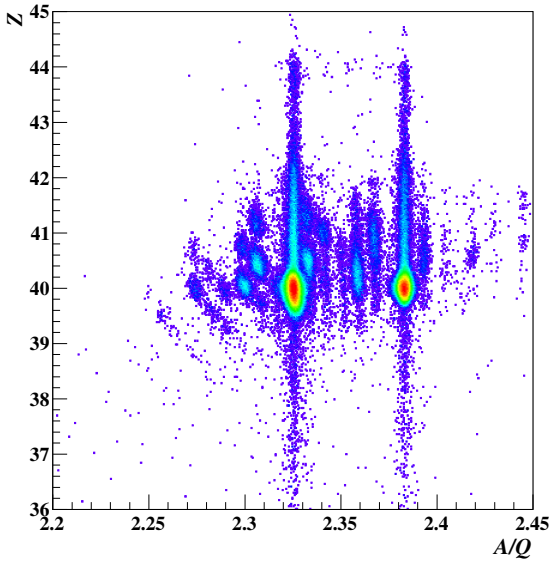

Figure 3.9: Particle identification plot for reaction products from the H_2 target after selecting the ^{93}Zr beam in the 0% $B\rho$ setting.

^{93}Zr beam. There are two problems: one is that there is the worse separation in Z than that of the experiment for ^{93}Nb, and the other is that Z has a divided value depending on its charge state, that is, H-like events have larger Z than F.S. events, resulting in two different Z values for one isotope. To solve these problems, we applied two corrections for Z to achieve higher resolutions and to cancel out invalid Z positions depending on the charge state. First, a correlation between ΔE_2 and E was canceled out in order to obtain better separation, because they

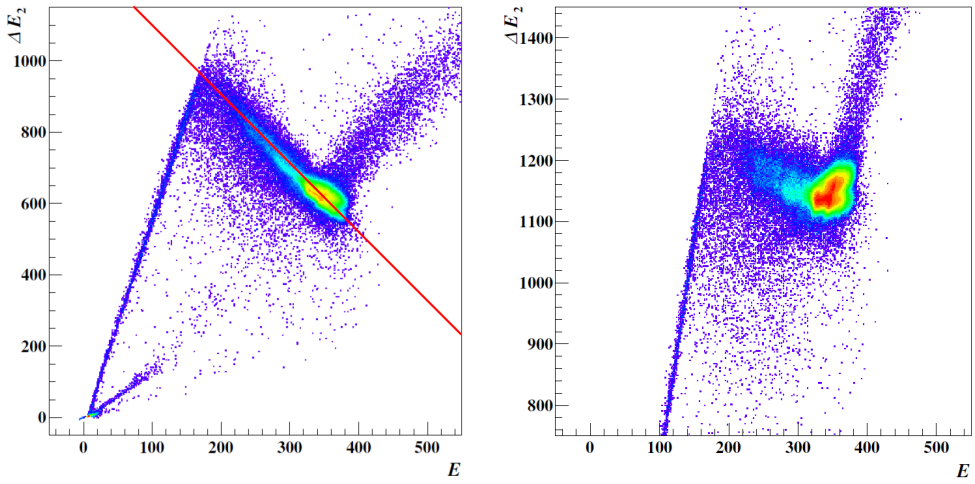

Figure 3.10: Correlation plot between ΔE_2 and E in the case of an H_2 target and a -4% ZDS $B\rho$ setting (Left). The correlation was canceled by the obtained linear function indicated by the red line (Right).

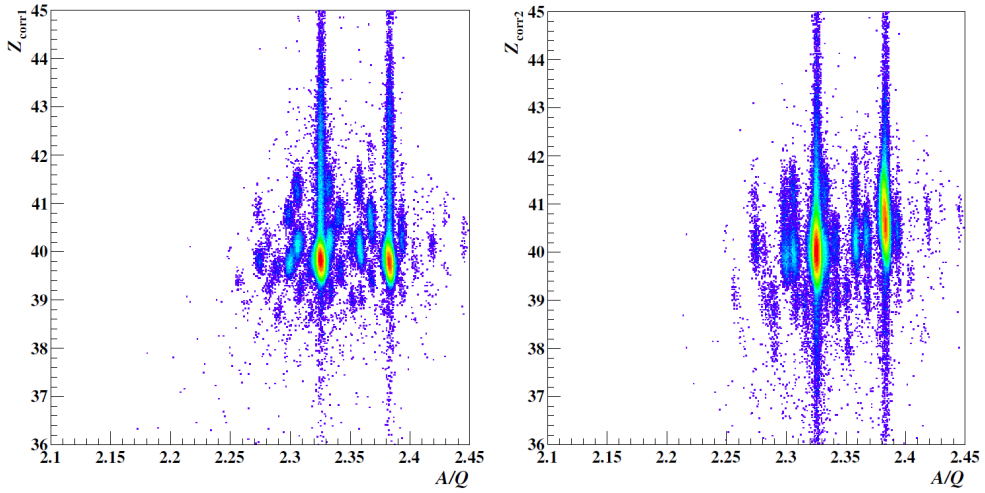

Figure 3.11: Particle identification plot after correction for $\Delta E_2 - E$ (Left) and for $\beta_{\mathrm{F8-F11}}$ (Right) from the H_2 target after selecting the ^{93}Zr beam in a 0% $B\rho$ setting.

should not be correlated. Figure 3.10 shows a correlation plot between ΔE_2 and E. The unstopped events have a negative correlation prior to correction. ΔE_2 was corrected by the linear function obtained by the fitting shown by the red line. The identification plot after ΔE_2 correction is shown in Fig. 3.11. A better separation of Z was obtained. Next, Z and $\beta_{\mathrm{F8-F11}}$ also have a correlation, as shown in

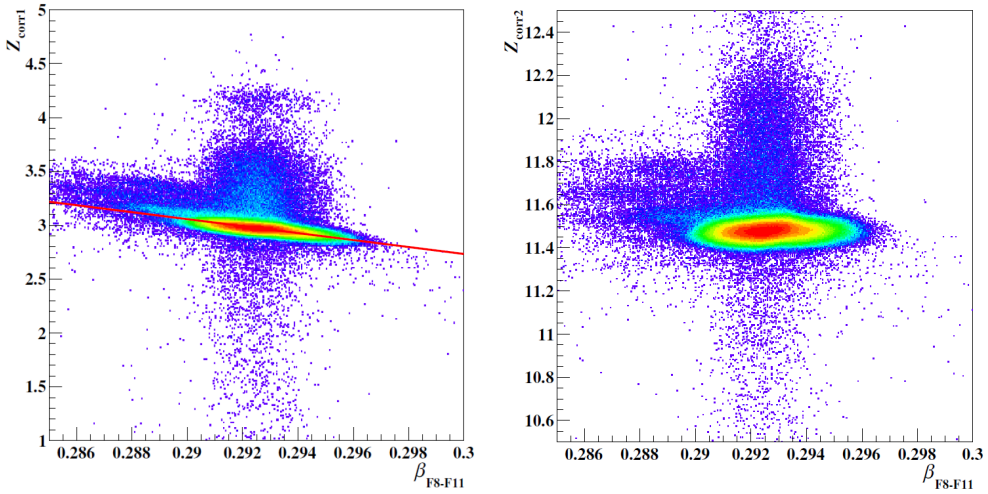

Figure 3.12: Correlation plot between Z and $\beta_{\mathrm{F8-F11}}$ in the case of an H_2 target and a -4% ZDS $B\rho$ setting (Left). The correlation was canceled out by the obtained linear function indicated by the red line (Right).

Fig. 3.12, although they generally should not. The atomic number Z was directly corrected by the linear function obtained by the fitting, as shown in Fig. 3.12. Figure 3.11 shows the corrected particle-identification plot of the reaction products. The atomic number Z divided by its charge state was merged but worse separation was obtained. Therefore, we used the $\Delta E - E$-corrected plot to count the yields of the reaction products.

Since the fragments have lower kinetic energies than those in the previous measurements [44, 45], they easily pick up electrons and change their charge states. Hence, reaction products with a few charge states, *i.e.*, F.S., H-like, and He-like fragments, were observed in Fig. 3.11. We obtained the charge-state distribution of ^{93}Zr from correlation plots between x_{F11} and ΔE, as shown in Fig. 3.13. The yields of the ^{93}Zr beam for each charge state at ZDS were estimated from Gaussian fittings of each locus after projection onto the x-axis. The derived-charge-state distributions were 34.34%, 48.21%, 17.11%, and 0.34% for the F.S., H-like, He-like, and Li-like beams, respectively. Since we assumed that the Li-like beam is negligible from the obtained distribution, the yields of each isotope were counted from the particle identification plot up to the He-like ones.

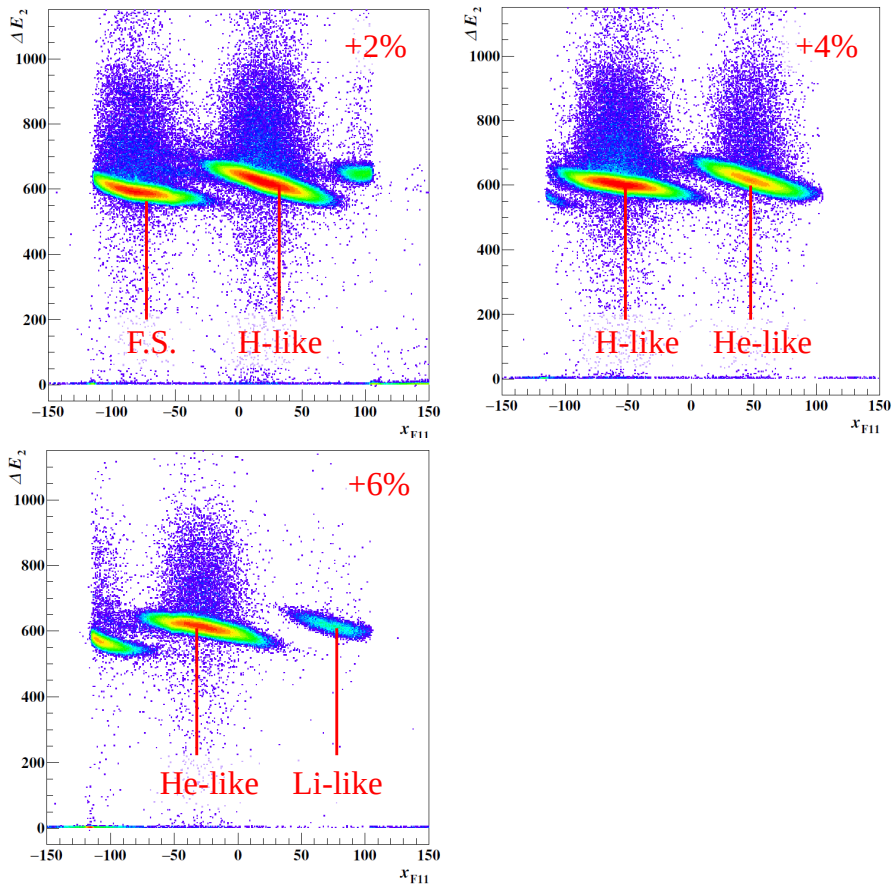

Figure 3.13: Charge-state distribution of the ^{93}Zr beam at ZDS by x_{F11} and ΔE at the +2% (Upper Left), +4% (Upper Right), and +6% (Lower Left) ZDS $B\rho$ settings. F.S. and H-like, H-like and He-like, He-like and Li-like beams were observed at the +2%, +4%, and +6% $B\rho$ settings, respectively.

3.3.3 Corrections

Correction for Acceptance

As with the analysis of ^{93}Nb data, it is possible that the reaction products passing near the edge of the dispersive focal plane may be lost under some $B\rho$ settings. In the dispersive mode, the acceptance of ZDS is limited to ±2% by the horizontal position at F11. Thus, the lost yields were compensated by the survival rate as a function of x_{F11}. The survival rate S was derived from the ratio of the reaction

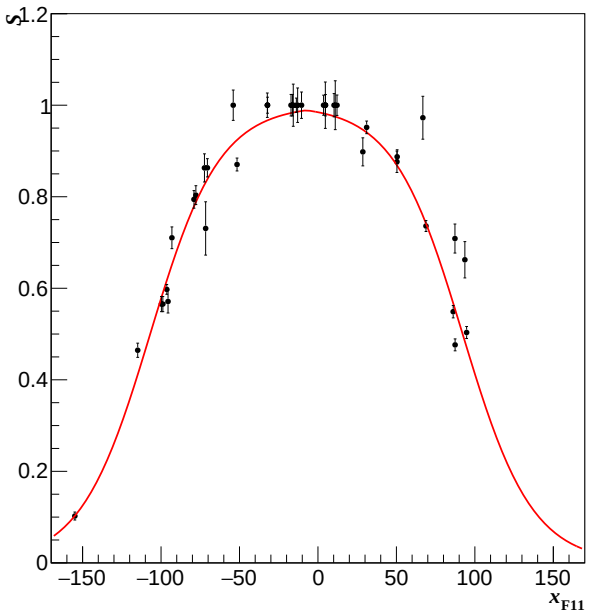

Figure 3.14: Survival-rate distribution represented by the black points and the fitting curve given by Eq. (3.7) as a function of x_{F11}, denoted the red line.

rates at two different $B\rho$ settings as:

$$S\left(x_{\mathrm{F11}}\right) = \frac{Y_{0\%}/B_{0\%}}{Y_{-3\%}/B_{-3\%}}, \tag{3.6}$$

where Y is the number of detected reaction products and B is the number of incident-beam particles ^{93}Zr. The $B\rho$ setting in the denominator was suitably selected so as to accept all produced isotopes. The obtained $S\left(x_{\mathrm{F11}}\right)$ were fitted by the Woods-Saxon function with parameters a, b, and V as:

$$f\left(x_{\mathrm{F11}}\right) = \left\{1 + \exp\left(\frac{|x_{\mathrm{F11}} - b| - V}{a}\right)\right\}^{-1}. \tag{3.7}$$

The parameters were derived to be a = 22.15 ± 0.50, b = -7.36 ± 0.39, and V = 99.56 ± 0.44 from the fitting shown in Fig.3.14. To determine the production cross section, isotopes with larger acceptances than 0.7 were used to avoid the uncertainty from rapid changes in the acceptance function.

Correction for Target Thickness

The target cell was composed of thin harvar foils. Therefore, surface of the target cell may be deformed by the pressure of the gas. Thus, the effective thickness of

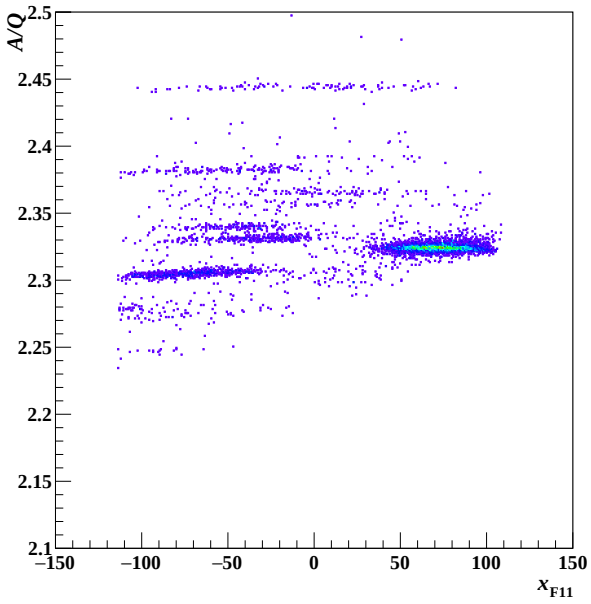

Figure 3.15: Correlation plot between x_{F11} and A/Q with a stopping-event gate in the case of an H_2 target and a -2% ZDS $B\rho$ setting. The stopping events upstream of the second layer can be counted from this plot.

the gas target was not identical to the cell thickness. We calculated the effective cell thickness from the difference in beam energy before and after the target cell. The obtained effective thickness was determined to be 22.6 mg/cm^2 for H_2 and 34.5 mg/cm^2 for D_2, as introduced in Sec. 3.2.3.

Correction for Rejected Events in $\Delta E_2 - E$ Plot

As mentioned in Sec. 3.3.1, the stopping events upstream of the second layer in MUSIC were rejected because their ΔE_2 value cannot be determined correctly. These events were counted from the correlation plot without Z information. Figure 3.15 shows the correlation plot between x_{F11} and A/Q. The number of stopping events for each isotope was estimated from the A/Q value with x_{F11} to obtain better separation. These yields were included in the total counts for each nuclide.

Table 3.7: Ratio of isotope-production cross sections for each charge state and each element.

p-Induced Case			
Charge State	Nb isotope	Zr isotope	Y isotope
F.S.	24.77%	29.32%	39.61%
H-like	49.64%	50.45%	45.98%
He-like	25.59%	20.23%	14.86%
d-Induced Case			
F.S.	25.92%	32.85%	43.02%
H-like	48.76%	48.51%	43.53%
He-like	25.32%	18.64%	13.45%

Correction for the Unmeasured Charge State

Yields of some isotopes with a certain charge state such as $^{93}Nb^{40+}$ and $^{88}Y^{38+}$ could not be counted because the tail of ^{93}Zr beam was completely contaminated. Moreover, the yield of $^{88}Zr^{40+}$ was not estimated due to large loss of the yield by the acceptance. For these isotopes, the production cross sections were deduced from other isotopes whose production cross sections for each charge state have been derived. From the analysis thus far and the isotope-production cross sections explained in Sec. 3.3.4, the weighted average ratios of the element-production cross sections for each charge state were derived as:

$$R_i = \frac{\sum_j \left(\sigma_{i,j}/\sigma_{\mathrm{tot},j}\,(1/\delta_{i,j})\right)}{\sum_j (1/\delta_{i,j})}, \tag{3.8}$$

where σ is the isotope-production cross section and δ is its statistical uncertainty. The subscripts i and j indicate the charge state and isotope, respectively. Note that the ratios of each charge state were almost constant over the element. The averaged ratios of the charge state for each element are listed in Table 3.7. The isotope-production cross sections for a charge state that cannot be measured were deduced from the charge-state distribution.

3.3.4 Isotope-Production Cross Sections

The isotope-production cross section for each reaction product and for each charge state was derived from the yields of the incident ^{93}Zr beam and each isotope produced with the charge state by subtracting the contribution from beamline

materials that can be estimated from empty-target runs as:

$$\sigma_{p,i} = \frac{1}{2t}\left(\frac{Y_{\mathrm{H}_2,i}}{B_{\mathrm{H}_2}} - \frac{Y_{\mathrm{emp},i}}{B_{\mathrm{emp}}}\right), \tag{3.9}$$

where σ, t, Y, and B represent the isotope-production cross section, the target thickness, the number of the reaction products, and the number of incident ^{93}Zr beams, respectively. The subscript indicates the secondary target and i is the charge state. The contribution to the yields of reaction products from beamline materials was less than 10% of those from hydrogen and deuterium. Its statistical uncertainty is calculated from the propagation of uncertainties as:

$$\delta_{p,i} = \frac{1}{2t}\sqrt{\frac{Y^2_{\mathrm{H}_2,i}}{B^2_{\mathrm{H}_2}}\left(\frac{1}{Y_{\mathrm{H}_2,i}} + \frac{1}{B_{\mathrm{H}_2}}\right) + \frac{Y^2_{\mathrm{emp},i}}{B^2_{\mathrm{emp}}}\left(\frac{1}{Y_{\mathrm{emp},i}} + \frac{1}{B_{\mathrm{emp}}}\right)} \tag{3.10}$$

The total isotope-production cross section is given by the sum of the cross sections for each charge state. For a d-induced reaction, the subscript H_2 is replaced by D_2.

3.3.5 Systematic-uncertainty Evaluation

The systematic uncertainty includes three components: uncertainty of the thickness of the secondary target, the contribution of multiple reaction in the secondary target, and the energy spread of the secondary beam in the secondary target. For the thickness of the secondary target, it is estimated to be 0.3% for the p-induced case and 0.8% for the d-induced case, respectively, based on the fluctuation of pressure and temperature in the cooled gaseous targets. The contributions of multiple reactions in the secondary target is estimated to be less than 1% from the transport simulation via the PHITS code because of thin gaseous targets. The largest uncertainty is the energy spread in the secondary target, which is estimated to be 4.4% for the p-induced reaction and 2.2% for the d-induced reaction based on PHITS calculations. The little difference in incident energy can change the tendency of the isotope-production cross sections because the absolute incident energy is relatively small.

3.4 Results and Discussion

In this section, the results of the measured isotope-production cross sections are presented. Intercomparison among the present data and the previous data measured at 105 [44] and 209 MeV/nucleon [45] is performed. Also, benchmark tests of theoretical model calculations and evaluated nuclear data libraries are performed using the measured data, together with the previously measured data [44, 45].

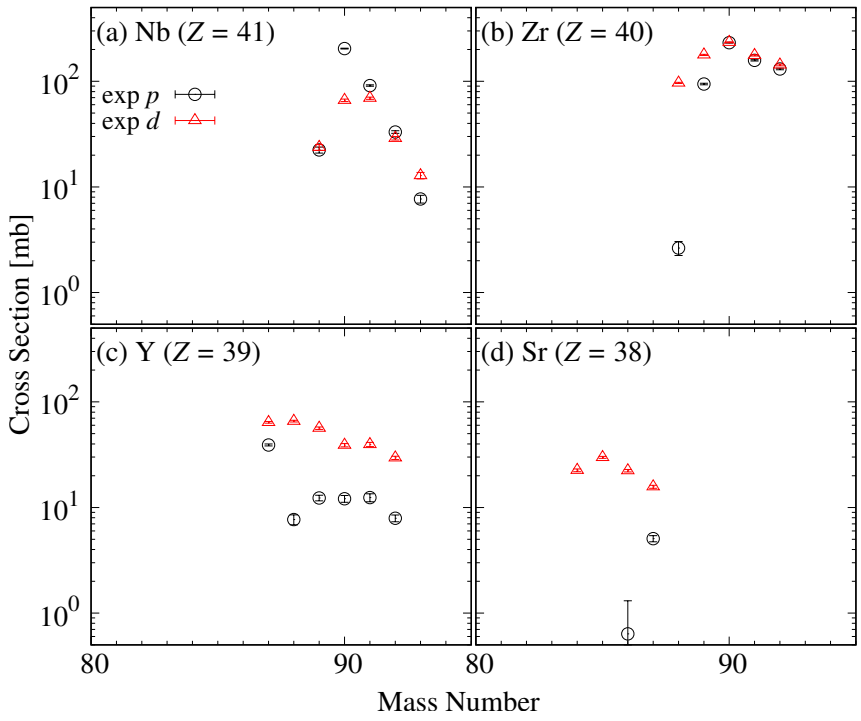

Figure 3.16: Measured isotope-production cross sections for the ^{93}Zr + p and d reactions at 51 and 52 MeV/nucleon, respectively: (a) Nb, (b) Zr, (c) Y, and (d) Sr. The black circles and red triangles represent the production cross sections for the p-induced (σ_p) and d-induced reactions (σ_d), respectively.

Finally, INCL++/GEM and INCL++/ABLA07 were used for the model analysis in order to discuss the causes of the underestimation in odd-Z isotopes seen in GEM calculations.

3.4.1 Experimental Data

Figure 3.16 shows the isotope-production cross sections for p- and d-induced reactions on ^{93}Zr at 51 and 52 MeV/nucleon, respectively. The error bars include only statistical uncertainties. We measured systematic data for 18 nuclides in the p-induced reaction and 20 nuclides in the d-induced reaction including stable isotopes, demonstrating the advantage of the inverse-kinematics method.

The measured σ_p shows the relatively narrow isotopic distribution. This range is determined by the lower limit of the measurable cross section and the acceptance of the ZDS. σ_p decreases rapidly in the lower-mass region; this is because of the relatively small total incident energy of 51 MeV/nucleon, which is able to knock

out fewer nucleons than the previous data [44, 45]. The jumps at neutron magic number $N = 50$ are seen in Zr for σ_p and in Zr and Y for σ_d. However, no jump of σ_p in Y is clearly seen. In the Y-isotopic chain, ^{87}Y has a noticeable large production cross section. This is because the excitation function of $^{93}\mathrm{Zr}(p, x)^{87}\mathrm{Y}$ reaction has its first peak around 50 MeV/nucleon, resulting in the sharp peak at ^{87}Y. This peak corresponds to alpha-particle emission with three neutrons. Comparison between σ_p and σ_d shows that σ_d has a much larger production cross section than σ_p, except in Nb. As discussed in Sec. 2.4.1, this tendency can be explained by the difference in total kinetic energies. Since the deuteron has twice the kinetic energy of the proton, the deuteron induces a higher excitation energy, resulting in more nucleon emissions from the pre-fragment formed in the d-induced reaction. Hence, fragments are more likely to remain in heavier isotopes in p-induced reactions, but to reach the relatively light isotopes in d-induced ones.

3.4.2 Incident Energy Dependence

Figures 3.17 and 3.18 show the measured isotope-production cross sections in p- and d-induced reactions on ^{93}Zr together with the previously measured data, to investigate the incident energy dependence of isotope-production cross sections. The error bars indicate the statistical uncertainties. The present data (σ_{p51} and σ_{d52}) are represented by red circles. The previously measured data at 105 and 209 MeV/nucleon [44, 45] are displayed by black triangles (σ_{p105} and σ_{d105}) and blue squares (σ_{p209} and σ_{d209}) in Figs 3.17 and 3.18, respectively.

Four differences are observed among the three data measured at the different energies. To begin with, in Figs. 3.17 (b) and (c), the lower-mass limits of the σ_{p51} distribution end at greater mass number than those of σ_{p105} and σ_{p209}, resulting in a narrow distribution. The measured range of the cross section is restricted by the lower limit of measurement possible and by the acceptance of ZDS. Since incident particles with higher kinetic energies can remove more nucleons than those with lower kinetic energies, the isotopic distribution of σ_{p51} has a much narrower range than the previous data at 105 and 209 MeV/nucleon. Next, σ_{p51} has much larger production cross sections near the target nucleus ^{93}Zr. These nuclei are mainly produced via the fusion-evaporation process, whereby an incident particle is captured by the target nucleus and subsequently de-excited with emission of several particles. In the lower-incident-energy case, this process is significantly enhanced. Hence, Nb and Zr isotopes with large-mass numbers have much larger cross sections than those in the higher-incident-energy cases. Then, in Fig. 3.17 (c), σ_{p51} for Y isotopes shows a very different trend from σ_{p105} and σ_{p209}. In particular, ^{87}Y has quite a large production cross section in σ_{p51}, and unique behavior is observed in the Y-isotopic chain. Finally, in the previously measured data at 105 and 209 MeV/nucleon, the productions of ^{90}Zr and ^{89}Y were enhanced due to the

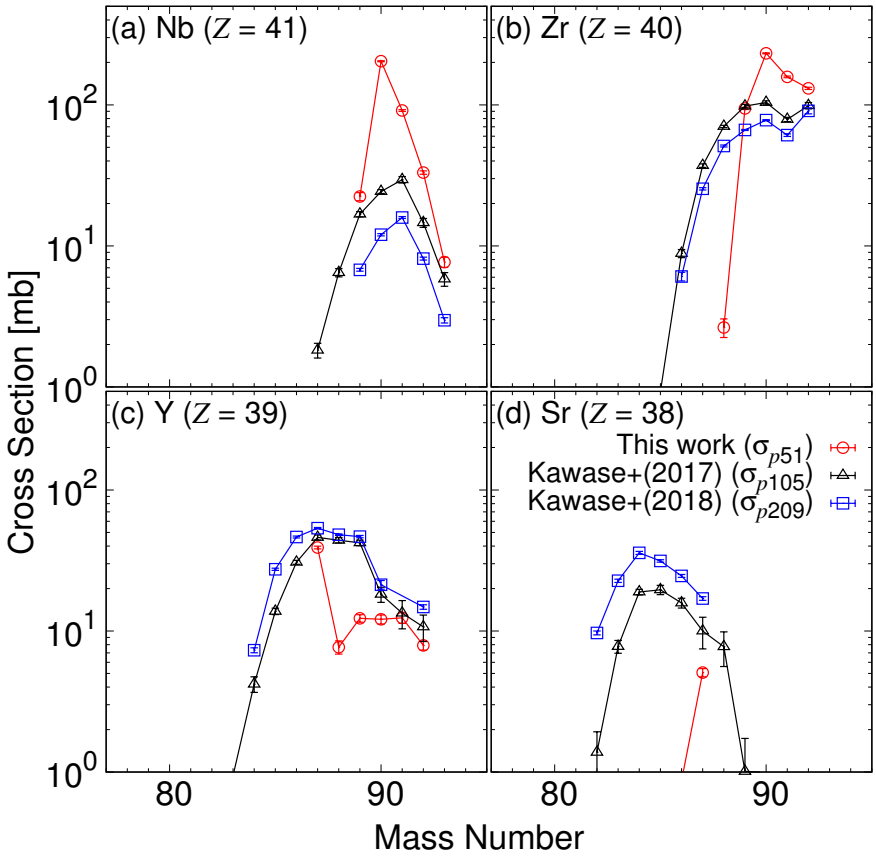

Figure 3.17: Measured isotope-production cross sections for the p-induced reaction on ^{93}Zr at 51 MeV with previous works at 105 and 209 MeV.

closed-shell effect at the neutron magic number $N = 50$, resulting in discontinuous jumps at ^{90}Zr and ^{89}Y. Although the isotopic distribution of Zr shows a jump between ^{90}Zr and ^{91}Zr, no clear jump is seen in Y isotopes regardless of the presence of jumps in σ_{p105} and σ_{p209}.

As for the d-induced reaction shown in Fig. 3.18, the distributions of σ_{d52}, σ_{d105}, and σ_{d209} have similar shapes. In terms of their quantities, the Nb and Zr isotope-production cross sections decrease with an increase in incident energy. By contrast, Sr isotope-production cross sections increase with an increase in incident energy. As mentioned above, those Nb and Zr isotopes near the target nucleus ^{93}Zr are largely produced by a fusion-evaporation process, which dominates in nuclear reactions at lower kinetic energies. On the other hand, the production of Sr isotopes, which requires many particle emissions like a spallation reaction, is enhanced in the higher-incident-energy cases. Thus, the dependence of isotope-production

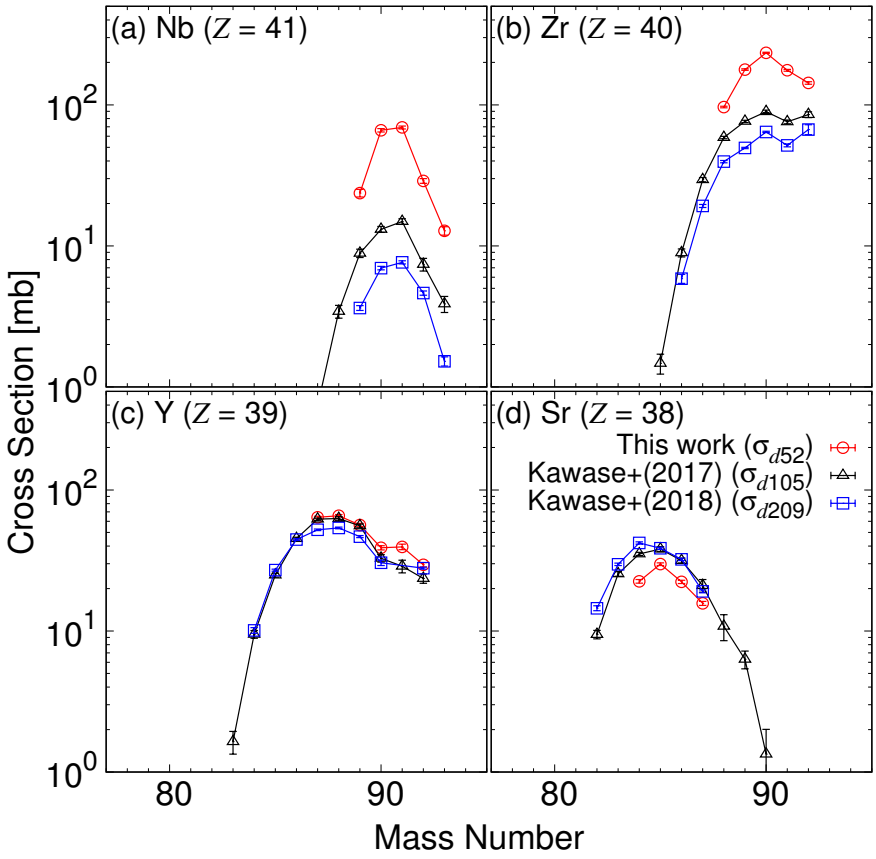

Figure 3.18: Same as Fig. 3.17, but for a d-induced reaction at 52 MeV/nucleon with previous works at 105 and 209 MeV/nucleon.

cross sections on incident energy has a different tendency in each isotopic chain. Finally, these three data show jumps at the neutron magic number $N = 50$ in both Zr and Y isotopes.

The isotope production cross sections are categorized by half-lives of reaction products for p- and d-induced reactions, as shown in Figs. 3.19 and 3.20, respectively. In both cases, the ratio of stable nuclei decreases with an increase of incident energy. This tendency originates from the production of stable Zr isotopes such as ^{90,91,92}Zr. On the other hand, the ratio of nuclei with half-lives over 30 thousand years has a minimum value at 209 MeV in the p-induced case and at 105 MeV/nucleon in the d-induced case. The components of these long-lived products are ^{92}Nb ($T_{1/2} = 3.47 \times 10^7$ years) and ^{81}Kr ($T_{1/2} = 2.29 \times 10^5$ years). Since ^{92}Nb has a larger production cross section in 50-MeV/nucleon cases than at higher energies, the ratios of long-lived products become maximal in lower-energy

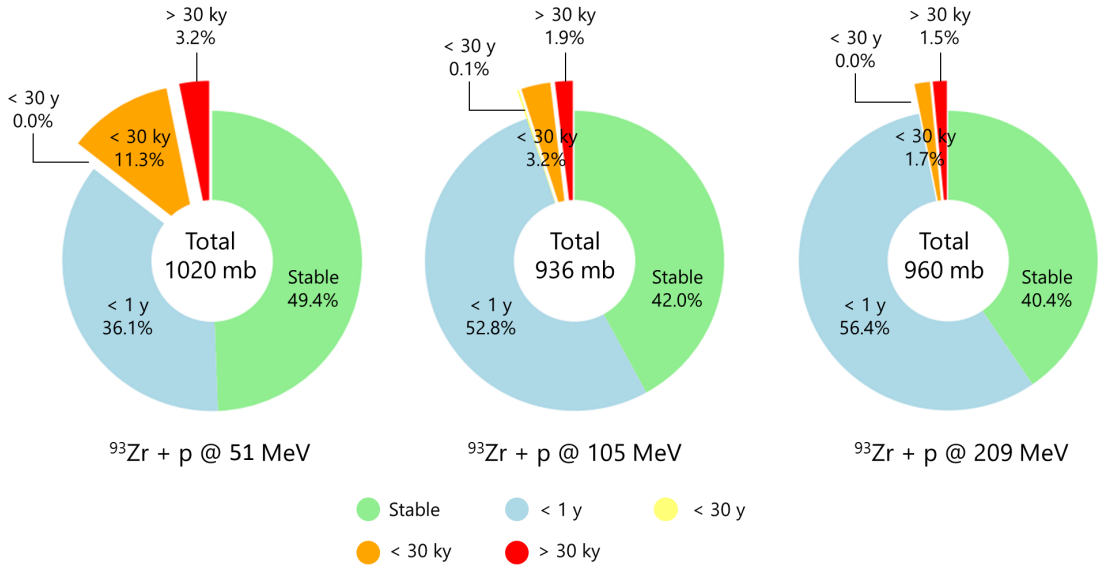

Figure 3.19: Pi chart of the ^{93}Zr + p data categorized by the half-lives of the reaction products.

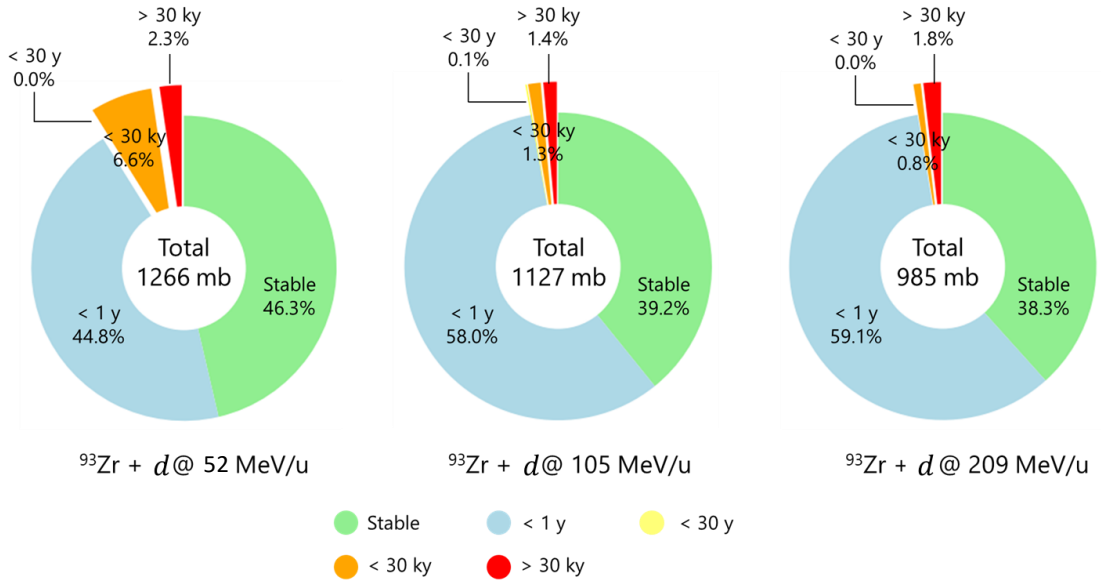

Figure 3.20: Same as Fig. 3.19, but for ^{93}Zr + d data.

cases. The sum of the production of ^{92}Nb and ^{81}Kr become the minimal for a total kinetic energy of around 200 MeV. From the viewpoint of reducing long-lived isotopes, irradiation of protons or deuterons with a total kinetic energy of 200 MeV is the best choice for considering the nuclear transmutation of ^{93}Zr by high-energy light-ions with the energy ranging from 50 to 200 MeV/nucleon.

3.4.3 Comparison with Model Calculations and Nuclear Data Libraries

The measured σ_p are compared with theoretical model calculations using the Particle and Heavy Ion Transport code System (PHITS) version 3.10 [48, 49], CCONE code [55], INCL++ [77] plus ABLA07 [78] code, and JENDL/ImPACT-2018 [68], together with the previous data. Also, σ_{d52}, σ_{d105}, and σ_{d209} are compared with the calculations with PHITS 3.10 and INCL++/ABLA07. The Liège Intranuclear Cascade model (INCL4.6) [53] and the Generalized Evaporation Model (GEM) [54] were employed to calculate the isotope-production cross section in PHITS. The Liège Intranuclear Cascade model ++ (INCL++) is a reimplementation of INCL4.6 for C++ with some modifications. It is combined with the evaporation code of ABLA07.

p-induced reaction

Figure 3.21 compares the measured data in the *p*-induced case, the calculations by PHITS, CCONE, and INCL++/ABLA07, and the data stored in JENDL/ImPACT-2018 at 209 (Upper panels), 105 (Center panels), and 51 MeV (Lower panels). Note that the JENDL/ImPACT-2018 data are not plotted in the upper row because the reaction energy of 209 MeV is out of range for JENDL/ImPACT-2018. Also, the CCONE calculation was performed in the 51- and 105-MeV cases but not at 209 MeV. The data for 209 and 105 MeV are taken from Refs. [44, 45] for systematic comparison. The four theoretical predictions show generally good agreement with the experimental data, even at such low-incident energy.

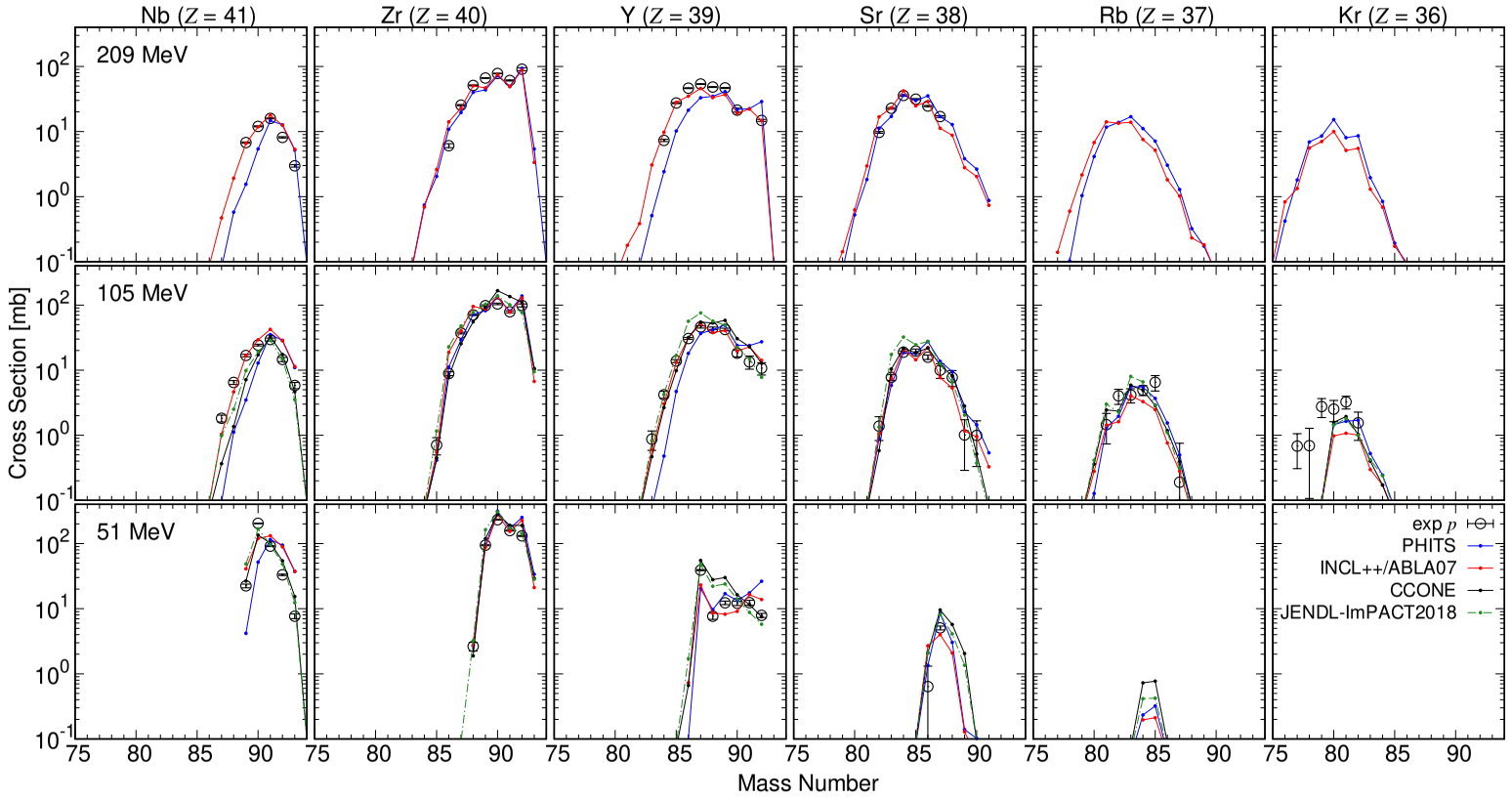

Figure 3.21: Comparison between the measured isotope-production cross sections and calculated cross sections with PHITS version 3.10, with INCL++/ABLA07 code, with CCONE code, and data in the evaluated nuclear data library JENDL/ImPACT-2018 for the p-induced reactions on ^{93}Zr.

First, we focus on the calculation by PHITS at 51 MeV, indicated by the blue lines in Fig. 3.21. In the PHITS calculation in which INCL4.6 and GEM are used, the shape of isotopic distribution and the peak for ^{87}Y are well reproduced. However, they also show some discrepancies in the 105- and 209-MeV/nucleon cases. The calculations are shifted by one-mass to the heavy side in the distribution of the Nb-isotope-production cross sections. Also, the calculations overestimate the production cross sections near the target nucleus, ^{93}Zr. These discrepancies have also been pointed out in previous studies [44, 45], and they still appear over the range of these incident energies. Finally, the calculated isotopic distribution of Y exhibits a sharp rise at mass number 87, but underestimates the production cross section. Next, the INCL++/ABLA07 calculation predicts the isotope-production cross section well, especially for Nb and Y isotopes with odd-Z. The one-mass-shift seen in the INCL4.6/GEM calculation is improved thanks to the better $n-p$ branching ratio in ABLA07 code. However, the neutron-rich sides of the Nb isotopes are still overestimated due to the inappropriate treatment of fusion-evaporation processes. The production cross sections for ^{92}Zr and ^{92}Y are reproduced fairly well by the INCL++/ABLA07 calculation. This is because the one-nucleon knockout reactions are treated appropriately in INCL++, as explained in Ref. [75, 76]. The CCONE code shows good agreement with the measured data. As seen in ^{93}Nb data, CCONE predicts the production cross sections well for ^{92}Zr and ^{92}Y, which are generated by one-nucleon knockout. Also, the production cross sections of the Nb isotopes are predicted well, although the two other calculations have discrepancies. Finally, the data from JENDL/ImPACT-2018 are shown by green lines in Fig. 3.21. This library reproduces the distribution of production cross sections in Nb isotopes fairly well compared with the calculations. In addition, there is no overestimation of the ^{92}Zr-production cross section. The magnitude of the ^{87}Y-production cross section is also well predicted; however, the production of certain Y and Sr isotopes is overestimated, especially in the 105-MeV case. As mentioned in Sec. 2.4.3, this is because of the pre-fragments gaining excitation energy. The χ^2 value is calculated with the formula:

$$\chi^2 = \frac{1}{n}\sum_{i}^{n}\left(\frac{\mathrm{exp}_i - \mathrm{calc}_i}{\mathrm{err}_i}\right)^2, \tag{3.11}$$

where n, exp_i, err_i, and calc_i represent the number of measured datapoints, the measured cross section, the statistical uncertainty of this cross section, and the calculated cross section, respectively. The χ^2 values for JENDL/ImPACT-2018 are 287.51 for the 51-MeV data, 57.67 for the 105-MeV data. That values for both the 51- and 105-MeV data is 121.32. The 51-MeV data shows much larger χ^2 value than 105-MeV data, because of the large magnitude of the cross section near the target nuclei, ^{93}Zr.

d-induced reaction

Figure 3.22 shows the experimental σ_d data, including the 105- and 209-MeV/nucleon cases [44, 45], as compared with the PHITS and INCL++/ABLA07 calculations. Both calculations predict the measured data well, even in the d-induced reaction with a relatively low-incident energy of approximately 50 MeV/nucleon. As seen in the p-induced reaction, the one-mass-shift in the Nb isotopes is still observed in the PHITS calculation; by contrast, the neutron-deficient region is improved in the INCL++/ABLA07 calculation. Also, the exaggerated even-odd staggering is clearly observed for the calculated Zr, Y, and Sr isotopes for both of the calculations, regardless of weak staggering of the measured data. In the low-incident-energy case, an intranuclear cascade process is no longer dominant and a fusion-evaporation process mainly occurs. Hence, almost all of the isotopes are generated in the evaporation process from the highly excited pre-fragment.

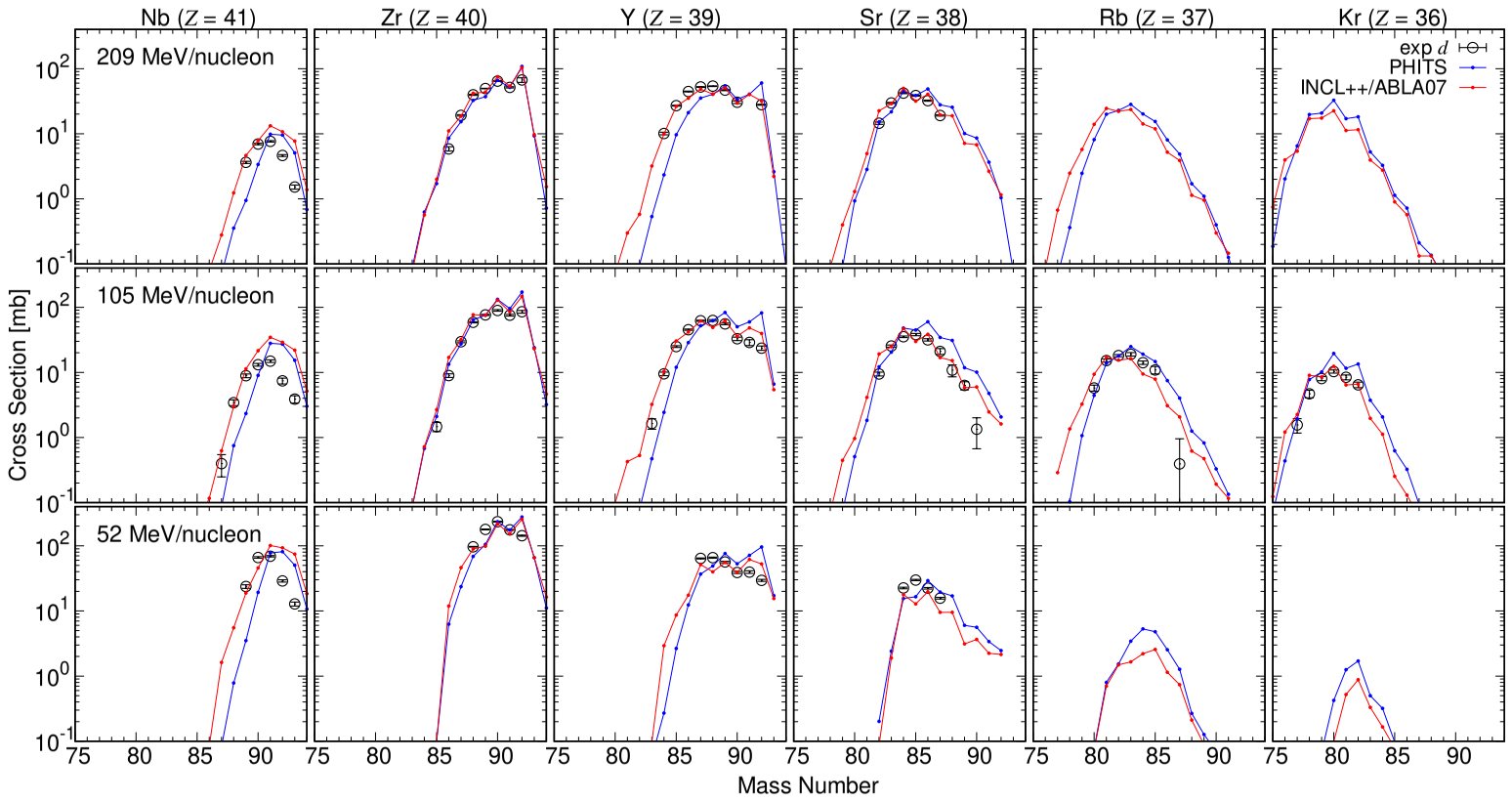

Figure 3.22: Comparison between the measured isotope-production cross sections and calculated cross sections with PHITS version 3.10 and with INCL++/ABLA07.

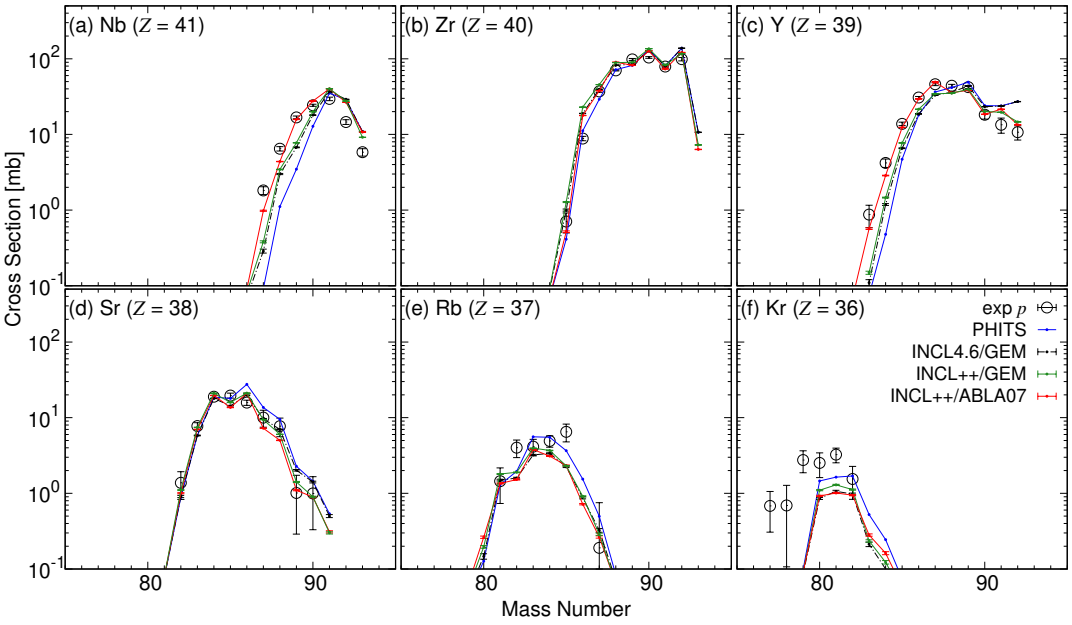

Figure 3.23: Isotope-production cross section in ^{93}Zr + p reaction at 105 MeV. The circles represent the measured data [44], and the lines indicate the calculated data by INCL4.6/GEM implemented in PHITS (blue solid lines), INCL4.6/GEM (black dot-dashed lines), INCL++/GEM (green solid lines), and INCL++/ABLA07 (red solid lines).

3.4.4 Theoretical-model Analysis by INCL++/GEM and INCL++/ABLA07

Figure 3.23 shows the measured isotope-production cross sections in p-induced reaction on ^{93}Zr at 105 MeV [44] together with the calculations by INCL4.6/GEM implemented in PHITS by the blue lines and INCL++/ABLA07 by the red lines. As mentioned in Sec. 3.4.3, INCL4.6/GEM implemented in PHITS fails to predict the production cross sections in the neutron-deficient region of odd-atomic number isotopes. The magnitude of the production cross section in the neutron-deficient region is mainly determined in the evaporation process based on the discussion in Sec. 2.4.4. Therefore, the underestimation is inferred to be originated from GEM calculation. While, INCL++/ABLA07 successfully reproduces the isotope-production cross section, especially in the neutron-deficient region of odd-atomic-number isotopes. Therefore, the comparison between ABLA07 and GEM may provide information on the cause of the underestimation in the PHITS calculation. In the following discussion, we focus on the ^{93}Zr + p reaction at 105 MeV. Since the two-step process is employed, the de-excitation process depends on the

mass and atomic number of pre-fragment and its excitation energy. In GEM implemented in PHITS, charged particle emissions are enhanced from the original GEM. To remove the effect of this enhancement, the calculation by using INCL4.6 and original GEM was performed, and the result is shown by the black lines in Fig. 3.23. The underestimation was improved by using the original GEM, but still two times underestimated. Prior to detailed comparisons between ABLA07 and original GEM, we examined the difference in isotope production caused by INC calculations with different codes. The calculation by using INCL++ and original GEM was performed as shown by the green lines in Fig. 3.23. In the regions of interest, the effect by the INC process is negligible. Therefore, we have performed the comparison between ABLA07 and GEM by INCL++/ABLA07 calculation and that by INCL++ and original GEM (INCL++/GEM).

Monte Carlo calculations of the ^{93}Zr + p reaction at 105 MeV were performed 10^7 times by using INCL++/ABLA07 and INCL++/GEM. For each calculation, the atomic number, the mass number, and the excitation energy of the pre-fragment formed in the INC process described by INCL++ were recorded. Then the evaporation processes were simulated by using the two evaporation codes, ABLA07 and GEM, and the atomic number, the mass number, and the kinetic energy of both the residual nuclei and emitted particles were recorded. The recorded data were analyzed event-by-event to clarify the difference in particle emissions between ABLA07 and GEM.

Figure 3.24 shows the branching ratios of proton and neutron emissions from ^{93}Nb* (Left), ^{92}Zr* (Center), and ^{92}Y* (Right) pre-fragments as a function of excitation energy. The dashed and the solid lines represent GEM calculation and ABLA07 calculation, respectively. In the GEM calculation, proton emission branching ratios in ^{93}Nb* and ^{92}Y* are twice as large as those in the ABLA07 calculation over the whole excitation energy. Conversely, the ABLA07 calculation shows a larger proton emission branching ratio in ^{92}Zr* than that in the GEM calculation. The branching ratios of other charged particle emission from ^{93}Nb* and ^{92}Y* are almost the same as those of proton emission. This tendency leads to the underestimation seen in the isotope-production cross sections of odd-atomic number isotopes. In the GEM calculation, the large proton emission branching ratio in Nb pre-fragment enhances the decays from Nb isotopes to Zr isotopes, but the decays from Zr isotopes to Y isotopes are suppressed due to the small proton emission branching ratio in Zr pre-fragments. As a result, the odd-atomic number isotopes have smaller yields in the evaporation stage in the GEM calculation, resulting in the underestimation in the neutron-deficient region of odd-atomic number isotopes.

Next, we investigate the reason why the differences are seen in the branching ratios calculated in GEM and ABLA07. In GEM and ABLA07, the decay width of

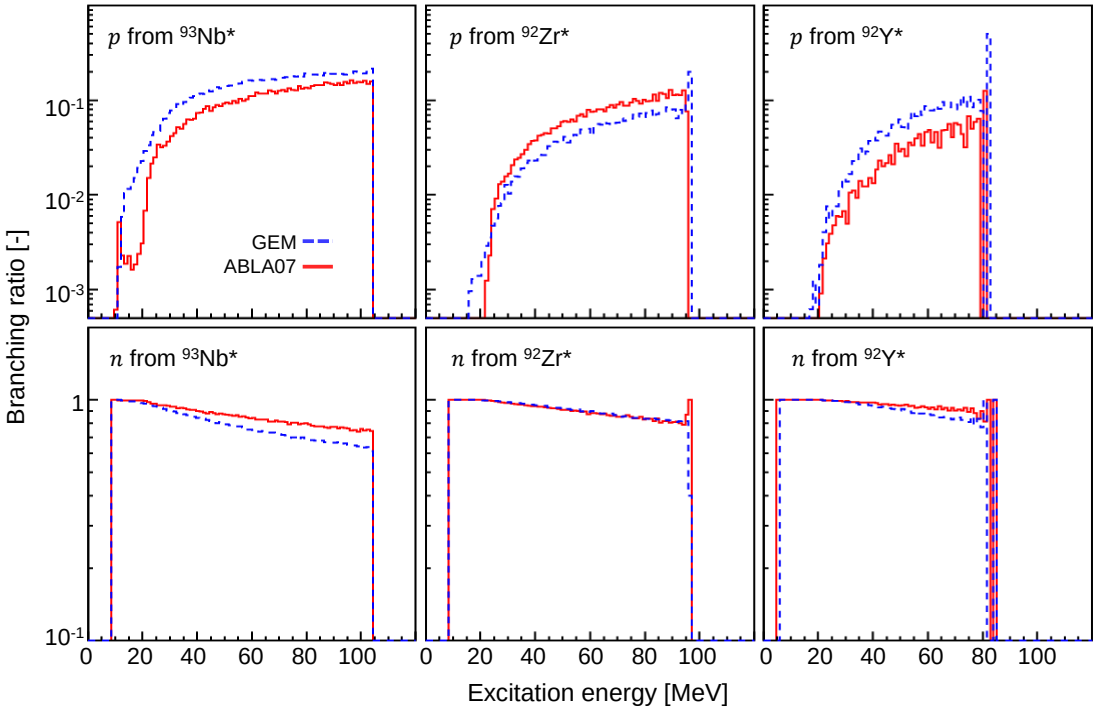

Figure 3.24: Branching ratios for proton (Upper) and neutron (Lower) emissions from ^{93}Nb* (Left), ^{92}Zr* (Center), and ^{92}Y* (Right) pre-fragments calculated by GEM and ABLA07 codes as a function of the excitation energy of pre-fragment. The blue dashed and red solid lines correspond to the GEM and ABLA07 calculations, respectively.

emitted particle j is calculated from the inverse cross section and the level density based on the Weisskopf-Ewing formalism [80] as described in Appendix A:

$$\Gamma_j \propto \int_V^{E_x-Q} \sigma_{\mathrm{inv}}(\varepsilon) \frac{\rho_{\mathrm{fin}}(E_x - Q - \varepsilon)}{\rho_{\mathrm{init}}(E_x)} \varepsilon d\varepsilon, \tag{3.12}$$

where E_x, Q, V, and ε represent the excitation energy of the parent nucleus, the Q-value of the reaction, the Coulomb barrier between the daughter nucleus and the emitted particle, and the kinetic energy of the emitted particle. Also, σ_{inv} denotes the inverse cross section corresponding to the cross section of the inverse process, that is, the incident of the emitted particle into the daughter nucleus. The variables ρ_{init} and ρ_{fin} correspond to the level densities of the parent and the daughter nucleus, respectively. Here, both or either σ_{inv} or ρ can be the cause of the underestimation. As the first step, we checked the behavior of σ_{inv} with attention to the difference between the odd- and even-atomic number isotopes. Figure 3.25 shows the $\sigma_{\mathrm{inv}}(\varepsilon)$ implemented in GEM and ABLA07. The

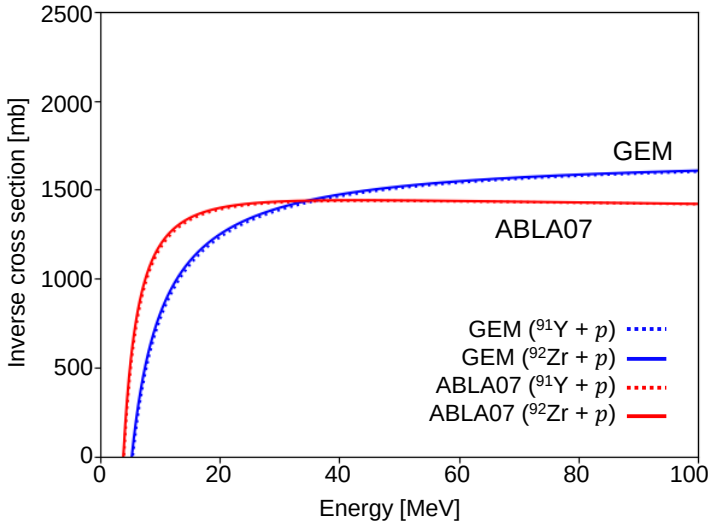

Figure 3.25: Inverse cross sections calculated by GEM and ABLA07 as a function of the kinetic energy of the emitted particle. The dotted and solid lines show the inverse reactions of proton emission from pre-fragments of ^{92}Zr* (^{91}Y + p) and ^{93}Nb* (^{92}Zr + p), respectively.

inverse cross section of the proton emission from ^{93}Nb*, which corresponds to the p-induced reaction on ^{92}Zr, is drawn by the dashed lines. That of proton emission from ^{92}Zr*, which corresponds to the p-induced reaction on ^{91}Y, is displayed by the dotted lines. We found that there is no appreciable odd-even effect on the inverse cross section used in both the calculations. Therefore, it is confirmed that the inverse cross section has no dependence on the even-odd of pre-fragment. This strongly implies that the level densities implemented in GEM is the cause of the remarkable underestimation in the Nb and Y isotopes, and should be reconsidered to resolve the underestimation as discussed in Ref. [81].

3.5 Conclusion

We have measured isotope-production cross sections for p- and d-induced reactions on long-lived fission product ^{93}Zr at approximately 50 MeV/nucleon at RIKEN RIBF. The energy dependences of the isotopic distribution of production cross sections were investigated for both reactions. In the d-induced reaction, three datapoints showed similar tendencies but different quantities from one another. In the p-induced reaction, by contrast, a narrower distribution was observed in the 51-MeV data compared with the higher-incident energy cases, due to there being

insufficient energy to knock out and/or emit many nucleons. Categorization of the half-lives of reaction products in the 50-, 105-, and 209-MeV/nucleon data indicates that a total reaction energy of approximately 200 MeV generates less long-lived products. Also, the measured isotope-production cross sections were compared with the calculations by PHITS version 3.10 employing INCL4.6 model plus GEM, by the CCONE code, and by the INCL++/ABLA07 code. The comparisons represented overall agreement even in the approximately 50-MeV/nucleon case. For the PHITS calculation, however, several discrepancies were seen in the present data, as well as in those measured at 105 and 209 MeV/nucleon. The calculation with ABLA07 shows fairly good agreement with the experimental data, especially in odd-Z isotopes in which the PHITS calculation failed to reproduce the experimental data. From the model analysis using INCL++/GEM and INCL++/ABLA07 data, it is apparent that the level density of GEM may cause the discrepancy. For more accurate simulation, validation of the level density used in GEM will be necessary in the future.

4 Summary and Conclusions

Nuclear transmutation of long-lived fission products (LLFPs) is an attractive means of treatment for high-level radioactive waste (HLW). For potential transmutation of ^{93}Zr, spallation reaction induced by light particles such as protons, deuterons, and neutrons is proposed. To study the feasibility of nuclear transmutation via spallation reaction, fundamental data have been accumulated as a part of the ImPACT Program. The measured data were used to benchmark the theoretical models and the evaluated nuclear data libraries. They were also used to understand the reaction mechanisms and behaviors of isotope-production cross sections by intercomparison among the present and previously measured data.

In Chapter 2, the study of isotope-production cross sections in ^{93}Nb + p, d, and C reactions at 113 MeV/nucleon was described. The measurement was performed using the inverse-kinematics method with a ^{93}Nb secondary beam and CH_2, CD_2, and C targets at RIKEN RIBF. The isotope-production cross sections were extracted from the data analysis via the TOF$-B\rho-\Delta E$ method. The measured data were consistent with the activation data within their statistical uncertainties, thereby validating the reliability of both the inverse-kinematics and activation methods. Next, the measured data were used for benchmark tests of several theoretical models (INCL4.6/GEM, CCONE, JQMD/GEM, and JQMD-2.0/GEM) and of evaluated nuclear data (JENDL-4.0/HE, JENDL/ImPACT-2018, TENDL-2017, and ENDF/B-VIII.0). For the p-induced reaction, the CCONE calculation shows the best reproducibility of $\chi^2 = 6.84$ among the models and libraries. Discrepancies are seen between the measured ^{93}Nb data and the PHITS calculation similar to the ^{93}Zr data, regardless of the changes of initial N and Z by one. These discrepancies included a one-mass-shift in the charge-exchange ($\Delta Z = +1$) reaction, overestimations of the production cross section near the target nucleus, underestimations in odd-Z isotopes, and exaggerated even-odd staggering. Finally, a comparison between the measured ^{93}Nb data and the previously measured ^{93}Zr data was performed paying particular attention to the jumps originating from the neutron magic number, $N = 50$. These jumps are seen both in the (p, pxn) and $(p, 2pxn)$ reactions in ^{93}Zr data; in contrast, the jump is not observed in the (p, pxn) reaction in ^{93}Nb. From the model analysis using INCL4.6/GEM imple-

mented in PHITS, it was revealed that the jumps can be seen depending on the balance of yields in the dynamic and evaporation processes. Also, the difference in the integrated distribution of production cross sections as a function of ΔZ for ^{93}Nb and ^{93}Zr data can be explained by the neutron- and proton-separation energies. Separation energies were confirmed to be significant in the distribution of production cross sections in spallation reactions.

In Chapter 3, the study of isotope-production cross sections in ^{93}Zr + p and d reactions at approximately 50 MeV/nucleon was described. The measurement was conducted using the inverse-kinematics method with a ^{93}Zr secondary beam and cooled gaseous H_2 and D_2 targets at RIKEN RIBF. The isotope-production cross sections were derived by the TOF$-B\rho-\Delta E$ method. First, the energy dependence of the production cross sections was investigated. In terms of nuclear transmutation, it was found that the p- and d-induced reactions at a total kinetic energy of around 200 MeV are the best choice in the energy range from 50 to 209 MeV/nucleon because they generate less long-lived products. Next, the measured data were used for benchmark tests of the theoretical models (INCL4.6/GEM, INCL++/ABLA07, and CCONE), as well as the newly evaluated nuclear data library JENDL/ImPACT-2018, together with the previously measured ^{93}Zr data at 105 and 209 MeV/nucleon. The calculations based on intranuclear cascade models, which are developed for nuclear reactions of several hundred MeV, show overall agreement with the experimental data even at low reaction energies. This benchmark demonstrates the applicability of the calculation by combination of the latest intranuclear and evaporation models for calculation of isotope-production cross sections in the several tens of MeV region. However, some of the discrepancies seen in the ^{93}Nb data are seen over incident energies ranging from 50 to 200 MeV/nucleon, including the one-mass-shift in a charge-exchange reaction and overestimations near the target nucleus. Finally, the cause of underestimation of the production cross sections in odd-Z isotopes in the GEM calculation is investigated based on the difference from the ABLA07 calculation, which successfully reproduces the production cross sections in odd-Z isotopes. From the model analysis of the INCL++/GEM and INCL++/ABLA07 calculations, the odd-Z isotopes emit more protons in the GEM calculation than in the ABLA07 calculation, resulting in underestimation in GEM calculation. This difference is believed to originate from the level density implemented in GEM and ABLA07 based upon a comparison of the inverse cross sections in GEM and ABLA07. It is expected that modification of the level density in GEM may improve this underestimation.

A great deal of fundamental data and a deep understanding are essential to develop more accurate and reliable reaction models and evaluated nuclear data libraries for nuclear-transmutation design, as well as other fields such as RI-beam production, ADS, and spallation-neutron sources. In this work, isotope-production

cross sections in spallation reactions were studied in terms of incident-energy and target-nucleus dependence, which are two main factors. Plenty of feed-back and insight for theoretical models was extracted over a broad energy range for two target nuclei. Thus, this work promotes the establishment of nuclear-transmutation technology as a basic elementary process. Moreover, our understanding of the isotopic distribution in spallation reactions is significantly advanced.

In the future, three works are expected. First, a further understanding of spallation reactions is necessary for more accurate prediction and wider application not only to nuclear transmutation but also other fields, *e.g.*, RI-beam production, ADS, and spallation-neutron sources. In the present experiment with ^{93}Nb, the secondary beam includes other isotopes such as ^{91,92}Y, ^{92}Zr, and ^{94}Nb. Therefore, systematic analysis of the many target isotopes can extend our findings. Second, OEDO has been newly constructed at RIBF and has started operation in 2017 [17]. New experimental data for lower incident energies such as 20- and 30-MeV/nucleon data can be measured using OEDO. Then, we can discuss the potential for nuclear transmutation using wider ranges of incident energies and incident particles in the future. Finally, correlation between reaction products and emitted particles measured by an exclusive measurement are significant. As mentioned in Ref. [25], the excitation energy can be deduced from the reaction product and the emitted charged particles. This may lead to a deeper understanding of spallation reactions, as well as improvement of the theoretical models. As a first step, an exclusive measurement of reaction products and emitted neutrons was performed using SAMURAI [15] at the RIBF in the ImPACT Program [9]. Analysis is expected to offer new insight for spallation reaction and highly tuned reaction models.

A Nuclear-reaction Models and Evaluated Nuclear Data Libraries

In this work, benchmark tests of the nuclear-reaction models implemented in Particle and Heavy Ion Transport code System (PHITS) [48], of CCONE code [55], of Liége Intranuclear Cascade ++ [77] plus ABLA07 code [78], and of the evaluated nuclear data libraries are performed. This appendix introduces the theoretical models and evaluated nuclear data libraries in comparison to the present experimental data in this thesis.

A.1 Nuclear-reaction Models

A.1.1 PHITS

Particle and Heavy Ion Transport code System (PHITS) [48] is a 3D Monte Carlo simulation code for the transport and interaction of radiation in matter. The PHITS code was mainly developed by the Japan Atomic Energy Agency (JAEA), the Research Organization for Information Science and Technology (RIST), and the High Energy Accelerator Research Organization (KEK). Its utilities are employed in a wide range of fields, such as the design of radiation facilities, radiation protection, medical physics, and planetary science. To calculated nuclear reactions in PHITS code, several models and evaluated nuclear data libraries are appropriately used for different incident particles, targets, and reaction energies. Figure A.1 shows a map of the physics models and data libraries recommended for use in PHITS for each condition quoted from Ref. [48]. Although PHITS version 3.10 is used for calculations, the map of the physics models is the same for version 3.02. In the PHITS calculation, nuclear reactions in the energy range of interest are basically described by a two-step process: pre-fragments are formed via the intranuclear cascade (INC) process, and the excited pre-fragments subsequently decay by the emission of light particles and gamma rays. The nuclear-reaction models concerning this work are the Liége Intranuclear Cascade model 4.6 (INCL4.6) [53] and the Generalized Evaporation Model (GEM) [54] for p- and d-induced reactions on

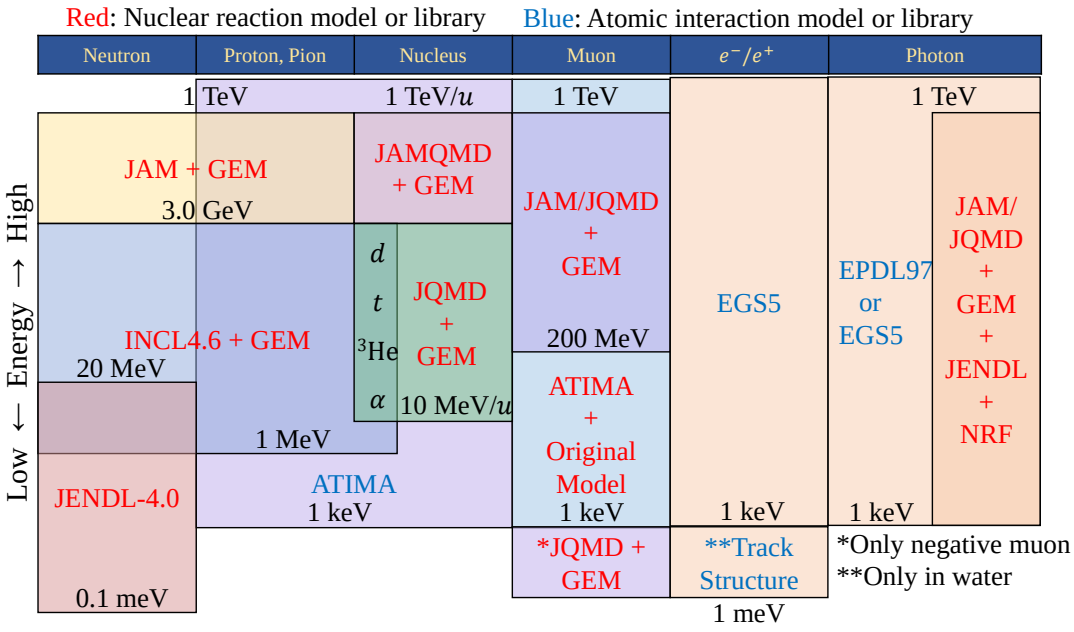

Figure A.1: Map of the physics models and data libraries recommended for use in PHITS3.02 to simulate the nuclear and atomic collisions quoted from Ref. [48].

^{93}Nb and ^{93}Zr at tens and several hundreds of MeV/nucleon, and the JAERI Quantum Molecular Dynamics (JQMD) model [56] and GEM for C-induced reactions on ^{93}Nb.

INCL4.6

INCL4.6 was developed by the French Alternative Energies and Atomic Energy Commission (CEA) and simulates nucleon-, pion-, and light-ion-induced reactions on nuclei for incident energies ranging from a few tens of MeV to a few GeV. In the PHITS code, INCL4.6 is implemented as a recommended reaction model for n-induced reactions ranging from 20 MeV to 3 GeV, p- and π-induced reactions ranging from 1 MeV to 3 GeV, and d-, t-, ^{3}He-, and α-induced reactions ranging from 10 MeV/nucleon to 3 GeV/nucleon, as mapped in Fig. A.1. At the beginning of the calculation, all nucleons are prepared in phase space. Their positions and momenta are determined depending on the Woods-Saxon and Fermi sphere distributions. Protons and neutrons move in the nuclear mean field and independent binary collisions occur in the cascade process. The scattered nucleons may pass through the surface of the potential or be reflected by the surface. The stopping

time of the cascade process $t_{\rm stop}$ is defined as

$$t_{\rm stop} = f_{\rm stop} t_0 \left(\frac{A_T}{208} \right)^{0.16}, \tag{A.1}$$

where $f_{\rm stop} = 1$, $t_0 = 70$ fm/c, and A_T denotes the mass number of the target nucleus. An excitation energy of a remnant after the cascade process E^* is calculated as the following equation with the total kinetic energy of nucleons in a remnant given by $\sum_{i \in A_{\rm rem}} \overline{T_i}$, the total kinetic energy of nucleons in the initial state given by $\sum_{i \in A_{\rm T}} T_i^0$, the mass number of the remnant given by $A_{\rm rem}$, and the Fermi kinetic energy given by T_F,

$$E^* = \sum_{i \in A_{\rm rem}} \overline{T_i} - \left[\sum_{i \in A_{\rm A_T}} T_i^0 - (A_T - A_{\rm rem}) T_F \right]. \tag{A.2}$$

GEM

GEM was developed by S. Furihata and simulates de-excitation of the remnant calculated by a cascade process with emission of light particles up to ^{28}Mg. In the PHITS code, GEM is implemented as a recommended reaction model for its evaporation process as mapped in Fig. A.1. The ejectile is determined by the distribution of emission probabilities calculated as

$$p_j = \frac{\Gamma_j}{\sum_k \Gamma_k}. \tag{A.3}$$

Here the total decay width Γ_j, for the emission of particle j from parent nucleus i with excitation energy E remaining in daughter nucleus d, is expressed by the integration of the decay probability between ϵ and $\epsilon + d\epsilon$ as

$$\Gamma_j = g_j \int_V^{E-Q} \sigma_{\rm inv} \frac{\rho_d (E - Q - \epsilon)}{\rho_i (E)} \epsilon d\epsilon, \tag{A.4}$$

where $\sigma_{\rm inv}$. ρ_x, V, Q, and ϵ denote the cross sections for the inverse reaction, the total level density of the x nucleus, the Coulomb barrier, the Q-value calculated by the Audi-Wapstra mass table, and the total kinetic energy of the particle, respectively. The coefficient g_j is expressed as $g_j = (2S_j + 1) m_j / \pi^2 \hbar^2$ with spin S_j and emitted particle mass m_j. The cross section for inverse reaction $\sigma_{\rm inv}$ is calculated as

$$\sigma_{\rm inv} (\epsilon) = \begin{cases} \sigma_g c_n (1 + b/\epsilon) & \text{for neutron,} \\ \sigma_g c_j (1 - V/\epsilon) & \text{for charged particles,} \end{cases} \tag{A.5}$$

where $\sigma_g = \pi R_b^2$ and $V = Z_j Z_d e^2 / R_c$ indicate the geometric cross section and the Coulomb barrier. The parameter set derived by Dostrovsky *et al.* is used for R_b, R_c, c_n, b, and c_j for neutron, proton, deuteron, triton, ^{3}He, and alpha-particle emission. For the other heavy ion emissions, the parameter set derived by Matsuse *et al.* is used. The total level density can be expressed according to the excitation energy as

$$\rho(E) = \begin{cases} \dfrac{\pi}{12} \dfrac{\exp\left[2\sqrt{a(E-\delta)}\right]}{a^{1/4}(E-\delta)^{5/4}} & \text{for} E \geq E_x \\ \dfrac{\pi}{12} \dfrac{1}{T} \exp\left(\dfrac{E-E_0}{T}\right) & \text{for} E < E_x \end{cases} \tag{A.6}$$

where $a = A_d/8$ is the level density parameter, and δ is the pairing energy of the daughter nucleus evaluated by Cook *et al.* The variable T is the nuclear temperature given by $1/T = \sqrt{a/U_x} - 1.5/U_x$, and E_0 is given by $E_0 = E_x - T(\log T - 0.25 \log a - 1.25 \log U_x + 2\sqrt{aU_x})$.

JQMD and JQMD-2.0

JQMD was developed by K. Niita *et al.* to simulate nucleon-nucleus, meson-nucleus, and nucleus-nucleus collision reactions with energies ranging from the Coulomb barrier to several GeV/nucleon via a semiclassical method. In the PHITS code, JQMD is implemented as a recommended reaction model for nucleus-induced reactions, except for *d*-, *t*-, ^{3}He-, and α-induced reactions, ranging from 10 MeV/nucleon to 1 TeV/nucleon, as shown in Fig. A.1. In the code, each nucleon state is expressed by

$$\phi_i(\mathbf{r}) = \frac{1}{(2\pi L)^{3/4}} \exp\left[-\frac{(\mathbf{r}-\mathbf{R_i})^2}{4L} + \frac{i}{\hbar}\mathbf{r}\cdot\mathbf{P_i}\right], \tag{A.7}$$

where L, $\mathbf{R_i}$, and $\mathbf{P_i}$ represent the width of the Gaussian wave function, the center position of the ith nucleon, and the center momentum of the ith nucleon, respectively. The total wave function Φ is calculated by taking the product of all wave functions:

$$\Phi(\mathbf{r}) = \prod_i \phi_i(\mathbf{r}). \tag{A.8}$$

Recently, JAERI Quantum Molecular Dynamics model 2.0 (JQMD-2.0) [69] was developed by modifying the original. In JQMD-2.0, the treatment of peripheral collisions is improved by modifying the treatment of neutron-proton scattering near the nuclear surface.

A.1.2 CCONE

The CCONE code [55] was developed by JAEA to evaluate of nuclear data and it plays a key role in the JENDL project. The CCONE code simulates nuclear reactions by combining several nuclear-reaction models: the optical model, the pre-equilibrium exciton model, and the Hauser-Feshbach statistical model with width-fluctuation correction.

A.1.3 INCL++

The Liége Intranuclear Cascade model ++ (INCL++) [77] is a redesign code of INCL4.6 as an object-oriented C++ code. In the INCL++ code used in this work, several additional improvements were made.

A.1.4 ABLA07

ABLA07 [78] was developed by A. Kelić *et al.* and is a code for calculating the de-excitation process of an excited remnant with simultaneous break-up, particle emission, and fission. The probability of a certain decay channel P_v is calculated by

$$P_v = \frac{\Gamma_v}{\sum_i \Gamma_i}, \tag{A.9}$$

where Γ_i indicates the decay width of the channel. According the Weisskopf-Ewing formalism, the decay width, from a parent nucleus i of excitation energy E_i to a daughter nucleus of excitation energy of E_f by emitting a particle v with a kinetic energy of ϵ_v, can be expressed by:

$$\Gamma_v\left(E_i\right) = \frac{2s_v+1}{2\pi}\frac{2m_v}{\pi\hbar^2}\int_0^{E_i-S_v-B_v}\sigma_c\left(\epsilon_v\right)\frac{\rho_f\left(E_f\right)}{\rho_i\left(E_i\right)}\left(\epsilon_v - B_v\right)dE_f, \tag{A.10}$$

where s_v, m_v, σ_c, ρ, and B_v are the spin of the emitted particle, the mass of the emitted particle, the cross section for the inverse reaction, the level density of the corresponding nucleus, and the Coulomb barrier, respectively. The inverse cross section σ_c is calculated as:

$$\sigma_c\left(\epsilon_v\right) = \pi R^2\left(1 - \frac{B_v}{\epsilon_v}\right), \tag{A.11}$$

where $R = R_{geom} + R_\lambda$. The radius R_{geom} and R_λ are calculated as

$$R_{geom} = 1.16\left(A_1^{1/3} + A_2^{1/3}\right), \tag{A.12}$$

$$R_\lambda = \sqrt{\frac{\hbar^2}{2\mu E_{cm}}}, \tag{A.13}$$

where A_1 and A_2 are the mass numbers of the daughter and emitting nuclei, respectively. The relative mass μ is calculated using the masses of the daughter nucleus M_1 and emitting particle M_2 as $\mu = M_1 M_2 / (M_1 + M_2)$, and $E_{cm} = \epsilon_v (A_1 - A_2) / A_1$. The Coulomb barrier B_v is calculated as the maximum value of the nuclear potential for $l = 0$, $V(r) = V_N(r) + V_C(r)$. The empirical nuclear potential as a function of the distance between the two surfaces $s = r - C_1 - C_2$ is expressed by R. Bass as:

$$-V_N(s) = \frac{C_1 C_2}{C_1 + C_2} \frac{1}{A \exp \frac{s}{d_1} + B \exp \frac{s}{d_2}} \tag{A.14}$$

where $A = 0.333$ MeV^{-1}fm, $B = 0.007$ MeV^{-1}fm, $d_1 = 3.5$ fm, and $d_2 = 0.65$ fm. The coefficients C_1 and C_2 are the half-density radii of the daughter nucleus and the emitted particle, respectively:

$$C_i = R_i \left(1 - \frac{(0.9984\text{fm})^2}{R_i^2}\right), \tag{A.15}$$

where R_1 for the daughter nucleus and R_2 for the emitted particle can be expressed as

$$R_1 = \left(1.28 A_1^{1/3} - 0.76 + \frac{0.8}{A_1^{1/3}}\right) \text{fm}, \tag{A.16}$$

$$R_2 = \left(1.28 A_2^{1/3} - 0.76 + \frac{0.8}{A_2^{1/3}} + d\right) \text{fm}. \tag{A.17}$$

The parameter d is determined by the kind of emitted particle, as d is 3 fm for p, 0 fm for d, t, and ^{3}He, and 1 fm for α. The Coulomb potential is calculated as:

$$V_C(r) = \begin{cases} 1.44 \dfrac{Z_1 Z_2}{r} & r > R_C \\ 1.44 \dfrac{Z_1 Z_2}{2 R_C} \left(3 - \dfrac{r^2}{R_C^2}\right) & r \leq R_C \end{cases} \tag{A.18}$$

where $R_C = 1.3 \left(A_1^{1/3} + A_2^{1/3}\right)$ fm, Z_1, and Z_2 correspond to the atomic numbers of the daughter nucleus and the emitted particle, respectively. The total level density is determined by the intrinsic level density ρ_{in}, corrected by the vibrational-enhancement factor $K_v ib$ and the rotational-enhancement factor $K_r ot$ as

$$\rho(E) = \rho_{in}(E) K_{vib}(E) K_{rot}(E). \tag{A.19}$$

The intrinsic level density ρ_{in} is formulated via the Fermi-gas model at middle or high excitation energies:

$$\rho_{in}(E) = \frac{\sqrt{\pi}}{12} \frac{\exp\left[2\sqrt{a\left(E_{eff} + \delta U k\left(E_{eff}\right) + \delta P h\left(E_{eff}\right)\right)}\right]}{a^{1/4} E_{eff}^{5/4}}, \tag{A.20}$$

where

$$a = 0.073A + 0.095 B_S A^{2/3}, \tag{A.21}$$

and A is the mass number of the nucleus, B_S is the ratio between the surface of the deformed nucleus and a spherical nucleus, and δU is the shell-correction energy. The functions $k\left(E_{eff}\right)$ and $h\left(E_{eff}\right)$ calculate the damping of the shell effect as $k\left(E_{eff}\right) = 1 - \exp -\gamma E_{eff}$ with $\gamma = a/\left(0.4A^{4/3}\right)$, and the superfluid-phase transition at the critical energy $E_{crit} = 10$ MeV as

$$h\left(E_{eff}\right) = \begin{cases} 1 - \left(1 - \dfrac{E_{eff}}{E_{crit}}\right)^2 & E_{eff} > E_{crit} \\ 1 & E_{eff} > E_{crit}. \end{cases} \tag{A.22}$$

The parameter δP is the pairing correction factor, which is calculated as

$$\delta P = -\frac{1}{4}\Delta^2 g + 2\Delta, \tag{A.23}$$

where the average pairing gap is $\Delta = 12/\sqrt{A}$ and the single-particle level density at the Fermi energy is $g = 6a/\pi^2$. The effective energy E_{eff} is calculated to consider different energies of combination of even and odd of proton and neutron numbers as:

$$E_{eff} = \begin{cases} E & \text{odd } Z - \text{odd } N \\ E - \Delta & \text{odd } Z - \text{even } N \text{ or even } Z - \text{odd } N \\ E - 2\Delta & \text{even } Z - \text{even } N. \end{cases} \tag{A.24}$$

For the intrinsic level density ρ_{in} at very low excitation energies, the constant-temperature level density is adopted:

A.2 Evaluated Nuclear Data Libraries

A.2.1 JENDL-4.0/HE

JENDL-4.0/HE [50] provided by JAEA is an extended library of JENDL-4.0 up to a reaction energy of 200 MeV for use in the accelerator related applications.

Cross section data, such as double-differential cross sections for emitted particles lighter than α, production cross sections of residual nuclei, total cross sections, total-reaction cross sections, and elastic scattering cross sections, in p- and n-induced reactions up to 200 MeV for 130 and 133 target nuclei are contained in JENDL-4.0/HE. The evaluation was performed based on model calculation by the CCONE code with systematic optimization of the model parameters. Also, a clustering pre-equilibrium model was employed for better reproducibility of the composite-particle-emission spectra.

A.2.2 JENDL/ImPACT-2018

Recently, JENDL/ImPACT-2018 was developed as a part of the ImPACT Project to study the transmutation of LLFPs. Cross sections data in p- and n-induced reactions up to 200 MeV for 163 target nuclei including four major LLFPs (^{79}Se, ^{93}Zr, ^{107}Pd, and ^{135}Cs) and important isotopes in their vicinity are stored in the library. Similar to JENDL-4.0/HE, the evaluation is based upon the model calculation by the CCONE code. The parameterization was performed based on the experimental isotope-production cross sections measured as a part of the ImPACT Project. In addition, recent knowledge concerning nuclear-structure theory is incorporated.

A.2.3 TENDL-2017

The TALYS Evaluated Nuclear Data Library 2017 (TENDL-2017) [51] was developed by the Paul Scherrer Institute (PSI) and the International Atomic Energy Agency (IAEA). It is the 9th version of TENDL. Nuclear data in n-, p-, d-, t-, ^{3}He-, α-, and γ-induced reactions with energies up to 200 MeV in approximately 2,800 isotopes with half-lives longer than 1 second are stored in TENDL-2017. The evaluation is performed by the TALYS nuclear model code system [82], adjusting its parameters.

A.2.4 ENDF/B-VIII.0

The Evaluated Nuclear Data File B-VIII.0 (ENDF/B-VIII.0) was developed by the Cross Section Evaluation Working Group (CSEWG), incorporating studies from across the United States and the international nuclear-science community. In addition to nuclear data for neutron and photonuclear reactions, the ENDF/B-VIII.0 includes nuclear data for p-induced reactions on 49 target isotopes with the reaction energies mostly up to 150 MeV.

References

1. *FEPC INFOBASE 2018* https://www.fepc.or.jp/library/data/infobase/. 2018.
2. Shibata, K. *et al.* JENDL-4.0: A New Library for Nuclear Science and Engineering. *Journal of Nuclear Science and Technology* **48,** 1–30 (2011).
3. Nishihara, K. Data for estimating potential radiotoxicity of spent nuclear fuel. *JAEA-Data/Code 2010-012* **2010,** 1 (2010).
4. Oigawa, H. *et al.* Role of ADS in the back-end of the fuel cycle strategies and associated design activities: The case of Japan. *Journal of Nuclear Materials* **415,** 229–236. ISSN: 0022-3115 (2011).
5. Bowman, C. D. ACCELERATOR-DRIVEN SYSTEMS FOR NUCLEAR WASTE TRANSMUTATION. *Annual Review of Nuclear and Particle Science* **48,** 505–556 (1998).
6. Wakabayashi, T. Transmutation characteristics of MA and LLFP in a fast reactor. *Progress in Nuclear Energy* **40,** 457–463. ISSN: 0149-1970 (2002).
7. Chiba, S. *et al.* Method to Reduce Long-lived Fission Products by Nuclear Transmutations with Fast Spectrum Reactors. *Scientific Reports* **7,** 13961 (2017).
8. Hermanne, A. Transmutation of Long Lived Fission Products: The Possibilities of Proton Induced Reactions. *Journal of Nuclear Science and Technology* **39,** 1202–1205 (2002).
9. *Impulsing Paradigm Change through Disruptive Technologies Program (ImPACT)* https://www.jst.go.jp/impact/en/program/08.html.
10. Blumenfeld, Y., Nilsson, T. & Duppen, P. V. Facilities and methods for radioactive ion beam production. *Physica Scripta* **T152,** 014023 (2013).
11. Maekawa, F. *et al.* First neutron production utilizing J-PARC pulsed spallation neutron source JSNS and neutronic performance demonstrated. *Nuclear Instruments and Methods in Physics Research Section A: Accelerators, Spectrometers, Detectors and Associated Equipment* **620,** 159–165. ISSN: 0168-9002 (2010).

12. Westfall, G. D. *et al.* Production of Neutron-Rich Nuclides by Fragmentation of 212-MeV/amu ^{48}Ca. *Phys. Rev. Lett.* **43,** 1859–1862 (1979).

13. Webber, W. R., Kish, J. C. & Schrier, D. A. Individual isotopic fragmentation cross sections of relativistic nuclei in hydrogen, helium, and carbon targets. *Phys. Rev. C* **41,** 547–565 (1990).

14. Kubo, T. *et al.* BigRIPS separator and ZeroDegree spectrometer at RIKEN RI Beam Factory. *Progress of Theoretical and Experimental Physics* **2012** (2012).

15. Kobayashi, T. *et al.* SAMURAI spectrometer for RI beam experiments. *Nuclear Instruments and Methods in Physics Research Section B: Beam Interactions with Materials and Atoms* **317,** 294–304. ISSN: 0168-583X (2013).

16. Uesaka, T. *et al.* The high resolution SHARAQ spectrometer. *Nuclear Instruments and Methods in Physics Research Section B: Beam Interactions with Materials and Atoms* **266,** 4218–4222. ISSN: 0168-583X (2008).

17. Michimasa, S. *et al.* OEDO, the energy-degrading beamline at RI Beam Factory. *Progress of Theoretical and Experimental Physics* **2019.** 043D01. ISSN: 2050-3911 (2019).

18. *RIKEN RIBF HomePage* `https://www.nishina.riken.jp/facility/RIBFfacility_e.html`.

19. Gloris, M. *et al.* Proton-induced production of residual radionuclides in lead at intermediate energies. *Nuclear Instruments and Methods in Physics Research Section A: Accelerators, Spectrometers, Detectors and Associated Equipment* **463,** 593–633. ISSN: 0168-9002 (2001).

20. Titarenko, Y. E. *et al.* Cross sections for nuclide production in 1 GeV proton-irradiated ^{208}Pb. *Phys. Rev. C* **65,** 064610 (2002).

21. Le Gentil, E. *et al.* Coincidence Measurement of Residues and Light Particles in the Reaction $^{56}\mathrm{Fe} + p$ at 1 GeV per Nucleon with the Spallation Reactions Setup SPALADIN. *Phys. Rev. Lett.* **100,** 022701 (2008).

22. Villagrasa-Canton, C. *et al.* Spallation residues in the reaction $^{56}\mathrm{Fe} + p$ at $0.3A, 0.5A, 0.75A, 1.0A$, and $1.5A$ GeV. *Phys. Rev. C* **75,** 044603 (2007).

23. Napolitani, P. *et al.* High-resolution velocity measurements on fully identified light nuclides produced in ^{56}Fe+hydrogen and ^{56}Fe+titanium systems. *Phys. Rev. C* **70,** 054607 (2004).

24. Giot, L. *et al.* Isotopic production cross sections of the residual nuclei in spallation reactions induced by 136Xe projectiles on proton at 500 AMeV. *Nuclear Physics A* **899,** 116–132. ISSN: 0375-9474 (2013).

25. Gorbinet, T. *et al.* Study of the reaction mechanisms of ^{136}Xe + p and ^{136}Xe + ^{12}C at 1 A GeV with inverse kinematics and large-acceptance detectors. *The European Physical Journal A* **55,** 11. ISSN: 1434-601X (2019).

26. Alcántara-Núñez, J. *et al.* Isotopic yields of spallation residues produced in ^{136}Xe-induced reactions on deuterium at 500A MeV. *Phys. Rev. C* **92,** 024607 (2015).

27. Napolitani, P. *et al.* Measurement of the complete nuclide production and kinetic energies of the system ^{136}Xe+hydrogen at 1 GeV per nucleon. *Phys. Rev. C* **76,** 064609 (2007).

28. Rejmund, F. *et al.* Measurement of isotopic cross sections of spallation residues in 800 A MeV ^{197}Au+p collisions. *Nuclear Physics A* **683,** 540–565. ISSN: 0375-9474 (2001).

29. Benlliure, J. *et al.* Signatures of fission dynamics in highly excited nuclei produced in ^{197}Au(800A MeV) on proton collisions. *Nuclear Physics A* **700,** 469–491. ISSN: 0375-9474 (2002).

30. Benlliure, J. *et al.* Isotopic production cross sections of fission residues in ^{197}Au-on-proton collisions at 800 A MeV. *Nuclear Physics A* **683,** 513–539. ISSN: 0375-9474 (2001).

31. Wang, S. *et al.* Light Fragment Production and Power Law Behavior in Au + Au Collisions. *Phys. Rev. Lett.* **74,** 2646–2649 (14 1995).

32. Wlazło, W. *et al.* Cross Sections of Spallation Residues Produced in 1AGeV ^{208}Pb on Proton Reactions. *Phys. Rev. Lett.* **84,** 5736–5739 (2000).

33. Audouin, L. *et al.* Evaporation residues produced in spallation of ^{208}Pb by protons at 500AMeV. *Nuclear Physics A* **768,** 1–21. ISSN: 0375-9474 (2006).

34. Enqvist, T. *et al.* Primary-residue production cross sections and kinetic energies in 1AGeV ^{208}Pb on deuteron reactions. *Nuclear Physics A* **703,** 435–465. ISSN: 0375-9474 (2002).

35. Enqvist, T. *et al.* Isotopic yields and kinetic energies of primary residues in 1 A GeV ^{208}Pb+p reactions. *Nuclear Physics A* **686,** 481–524. ISSN: 0375-9474 (2001).

36. Fernandez-Dominguez, B. *et al.* Nuclide cross-sections of fission fragments in the reaction ^{208}Pb + p at 500A MeV. *Nuclear Physics A* **747,** 227–267. ISSN: 0375-9474 (2005).

37. Taieb, J. *et al.* Evaporation residues produced in the spallation reaction ^{238}U+p at 1AGeV. *Nuclear Physics A* **724,** 413–430. ISSN: 0375-9474 (2003).

38. Bernas, M. *et al.* Fission-residues produced in the spallation reaction ^{238}U + p at 1AGeV. *Nuclear Physics A* **725,** 213–253. ISSN: 0375-9474 (2003).

39. Pereira, J., Armbruster, P., Benlliure, J. & Schmidt, K.-H. Comprehensive analysis of fission-reaction properties in the nuclear spallation of ^{238}U(1 GeV/nucleon) on deuterium. *Phys. Rev. C* **75,** 044604 (2007).

40. Casarejos, E. *et al.* Isotopic production cross sections of spallation-evaporation residues from reactions of ^{238}U(1A GeV) with deuterium. *Phys. Rev. C* **74,** 044612 (2006).

41. Ricciardi, M. V. *et al.* Light nuclides produced in the proton-induced spallation of ^{238}U at 1 GeV. *Phys. Rev. C* **73,** 014607 (2006).

42. Armbruster, P. *et al.* Measurement of a Complete Set of Nuclides, Cross Sections, and Kinetic Energies in Spallation of ^{238}U 1A GeV with Protons. *Phys. Rev. Lett.* **93,** 212701 (2004).

43. Wang, H. *et al.* Spallation reaction study for fission products in nuclear waste: Cross section measurements for ^{137}Cs and ^{90}Sr on proton and deuteron. *Physics Letters B* **754,** 104–108. ISSN: 0370-2693 (2016).

44. Kawase, S. *et al.* Study of proton- and deuteron-induced spallation reactions on the long-lived fission product ^{93}Zr at 105 MeV/nucleon in inverse kinematics. *Progress of Theoretical and Experimental Physics* **2017,** 093D03 (2017).

45. Kawase, S. *et al.* Measurement of isotopic production cross sections of proton- and deuteron-induced reactions on ^{93}Zr at 200 MeV/nucleon. *JAEA-Conf2018-001* **2018,** 111 (2018).

46. Wang, H. *et al.* Enhancement of element production by incomplete fusion reaction with weakly bound deuteron. *Communications Physics* **2,** 2399–3650 (2019).

47. Wang, H. *et al.* Spallation reaction study for the long-lived fission product ^{107}Pd. *Progress of Theoretical and Experimental Physics* **2017,** 021D01 (2017).

48. Sato, T. *et al.* Features of Particle and Heavy Ion Transport code System (PHITS) version 3.02. *Journal of Nuclear Science and Technology* **55,** 684–690 (2018).

49. Iwamoto, Y. *et al.* Benchmark study of the recent version of the PHITS code. *Journal of Nuclear Science and Technology* **54,** 617–635 (2017).

50. Kunieda, S. *et al.* Overview of JENDL-4.0/HE and Benchmark Calculations. *JAEA-Conf2016-004* **2016,** 41–46 (2016).

51. Koning, A. *et al.* TENDL: Complete Nuclear Data Library for Innovative Nuclear Science and Technology. *Nuclear Data Sheets* **155.** Special Issue on Nuclear Reaction Data, 1–55. ISSN: 0090-3752 (2019).

52. Brown, D. *et al.* ENDF/B-VIII.0: The 8th Major Release of the Nuclear Reaction Data Library with CIELO-project Cross Sections, New Standards and Thermal Scattering Data. *Nuclear Data Sheets* **148,** 1–142. ISSN: 0090-3752 (2018).

53. Boudard, A., Cugnon, J., David, J.-C., Leray, S. & Mancusi, D. New potentialities of the Liège intranuclear cascade model for reactions induced by nucleons and light charged particles. *Phys. Rev. C* **87,** 014606 (2013).

54. Furihata, S. Statistical analysis of light fragment production from medium energy proton-induced reactions. *Nuclear Instruments and Methods in Physics Research Section B: Beam Interactions with Materials and Atoms* **171,** 251–258. ISSN: 0168-583X (2000).

55. Iwamoto, O., Iwamoto, N., Kunieda, S., Minato, F. & Shibata, K. The CCONE Code System and its Application to Nuclear Data Evaluation for Fission and Other Reactions. *Nuclear Data Sheets* **131,** 259–288. ISSN: 0090-3752 (2016).

56. Niita, K. *et al.* Analysis of the (N,xN') reactions by quantum molecular dynamics plus statistical decay model. *Phys. Rev. C* **52,** 2620–2635 (1995).

57. Kumagai, H., Ozawa, A., Fukuda, N., Summerer, K. & Tanihata, I. Delay-line PPAC for high-energy light ions. *Nuclear Instruments and Methods in Physics Research Section A: Accelerators, Spectrometers, Detectors and Associated Equipment* **470,** 562–570. ISSN: 0168-9002 (2001).

58. Kimura, K. *et al.* High-rate particle identification of high-energy heavy ions using a tilted electrode gas ionization chamber. *Nuclear Instruments and Methods in Physics Research Section A: Accelerators, Spectrometers, Detectors and Associated Equipment* **538,** 608–614. ISSN: 0168-9002 (2005).

59. Fukuda, N. *et al.* Identification and separation of radioactive isotope beams by the BigRIPS separator at the RIKEN RI Beam Factory. *Nuclear Instruments and Methods in Physics Research Section B: Beam Interactions with Materials and Atoms* **317,** 323–332. ISSN: 0168-583X (2013).

60. Makino, K. & Berz, M. COSY INFINITY Version 9. *Nuclear Instruments and Methods in Physics Research Section A: Accelerators, Spectrometers, Detectors and Associated Equipment* **558,** 346–350. ISSN: 0168-9002 (2006).

61. *RIKEN RIBF Homepage* `http://ribf.riken.jp/BigRIPSInfo/optics/fig/bStandard.txt`.

62. Tarasov, O. & Bazin, D. LISE++: Exotic beam production with fragment separators and their design. *Nuclear Instruments and Methods in Physics Research Section B: Beam Interactions with Materials and Atoms* **376,** 185–187. ISSN: 0168-583X (2016).

63. Folden, C. M. *et al.* New neutron-rich microsecond isomers observed among fission products of ^{238}U at 80 MeV/nucleon. *Phys. Rev. C* **79,** 064318 (2009).

64. Ohnishi, T. *et al.* Identification of 45 New Neutron-Rich Isotopes Produced by In-Flight Fission of a ^{238}U Beam at 345 MeV/nucleon. *Journal of the Physical Society of Japan* **79,** 073201 (2010).

65. Ohnishi, T. *et al.* Identification of New Isotopes ^{125}Pd and ^{126}Pd Produced by In-Flight Fission of 345 MeV/nucleon ^{238}U: First Results from the RIKEN RI Beam Factory. *Journal of the Physical Society of Japan* **77,** 083201 (2008).

66. Titarenko, Y. E. *et al.* Measurement and simulation of the cross sections for nuclide production in ^{93}Nb and ^{nat}Ni targets irradiated with 0.04- to 2.6-GeV protons. *Physics of Atomic Nuclei* **74,** 537. ISSN: 1562-692X (2011).

67. Wang, M. *et al.* The AME2016 atomic mass evaluation (II). Tables, graphs and references. *Chinese Physics C* **41,** 030003 (2017).

68. Kunieda, S. *et al.* JENDL/ImPACT-2018: a new nuclear data library for innovative studies on transmutation of long-lived fission products. *Journal of Nuclear Science and Technology* **0,** 1–19 (2019).

69. Ogawa, T. *et al.* Energy-dependent fragmentation cross sections of relativistic ^{12}C. *Phys. Rev. C* **92,** 024614 (2015).

70. Niita, K., Takada, H., Meigo, S. & Ikeda, Y. High-energy particle transport code NMTC/JAM. *Nuclear Instruments and Methods in Physics Research Section B: Beam Interactions with Materials and Atoms* **184,** 406–420 (2001).

71. Sihver, L. *et al.* Current status of the "Hybrid Kurotama model" for total reaction cross sections. *Nuclear Instruments and Methods in Physics Research Section B: Beam Interactions with Materials and Atoms* **334,** 34–39. ISSN: 0168-583X (2014).

72. Iida, K., Kohama, A. & Oyamatsu, K. Formula for Proton Nucleus Reaction Cross Section at Intermediate Energies and Its Application. *Journal of the Physical Society of Japan* **76,** 044201 (2007).

73. Koning, A. & Delaroche, J. Local and global nucleon optical models from 1 keV to 200 MeV. *Nuclear Physics A* **713,** 231–310. ISSN: 0375-9474 (2003).

74. An, H. & Cai, C. Global deuteron optical model potential for the energy range up to 183 MeV. *Phys. Rev. C* **73,** 054605 (2006).

75. Mancusi, D. *et al.* Improving the description of proton-induced one-nucleon removal in intranuclear-cascade models. *Phys. Rev. C* **91,** 034602 (2015).

76. Rodrıéguez-Sánchez, J. L. *et al.* Improvement of one-nucleon removal and total reaction cross sections in the Liège intranuclear-cascade model using Hartree-Fock-Bogoliubov calculations. *Phys. Rev. C* **96,** 054602 (2017).

77. Mancusi, D. *et al.* Extension of the Liège intranuclear-cascade model to reactions induced by light nuclei. *Phys. Rev. C* **90,** 054602 (2014).

78. Kelic, A., Ricciardi, M. V. & Schmidt, K.-H. *ABLA07 - towards a complete description of the decay channels of a nuclear system from spontaneous fission to multifragmentation* 2009. arXiv: 0906.4193.

79. Ryuto, H. *et al.* Liquid hydrogen and helium targets for radioisotope beams at RIKEN. *Nuclear Instruments and Methods in Physics Research Section A: Accelerators, Spectrometers, Detectors and Associated Equipment* **555,** 1–5. ISSN: 0168-9002 (2005).

80. Weisskopf, V. F. & Ewing, D. H. On the Yield of Nuclear Reactions with Heavy Elements. *Phys. Rev.* **57,** 472–485 (1940).

81. Sato, S. & Watanabe, Y. Effect of the level density on odd-even staggering in proton- and deuteron-induced spallation reactions on ^{93}Zr and ^{107}Pd. *JAEA-Conf2019-001* **2019,** 103 (2019).

82. Koning, A. & Rochman, D. Modern Nuclear Data Evaluation with the TALYS Code System. *Nuclear Data Sheets* **113,** 2841–2934. ISSN: 0090-3752 (2012).

Acknowledgements

This work was carried out at the Department of Advanced Energy Engineering Science, Interdisciplinary Graduate School of Engineering Sciences, Kyushu University, under the supervision of Professor Yukinobu Watanabe. I would like to express a lot of thanks to many people for their help in the present work.

First and foremost, I would like to express my sincere gratitude to Professor Yukinobu Watanabe. Without his guidance and persistent help, this thesis would not have been possible. I have learnt a lot from him not only nuclear physics itself but also logical thinking and sincere attitude towards physics and scientific research. His comments and supports are always valuable and precious.

My great thanks are also expressed to Professors Tomotsugu Wakasa, Hironao Sakaki, and Associate Professor Tadahiro Kin for careful reading of this manuscript and valuable comments.

I would like to thank Assistant Professor Shoichiro Kawase. I could not have completed this work without his helpful comments and supports on data analysis. His insightful comments made enormous contribution to this work.

I would like to express my great thanks to Dr. He Wang (Titech) and Dr. Hideaki Otsu (RIKEN Nishina Center) for their precious advice, comments, and support on the experiments.

I also wish to thank very much Professor Hiroyoshi Sakurai (University of Tokyo) for his support and contribution on ImPACT Project.

I would like to address my thanks to all the ImPACT-RIBF collaborators; Professors Susumu Shimoura, Takashi Nakamura, Masayuki Aikawa, Associate Professor Yukie Maeda, Assistant Professors Yosuke Kondo, Maya Takechi, Shin'ichiro Michimasa, Megumi Niikura, Yasuhiro Togano, Drs. Nobuyuki Chiga, Toshiyuki Sumikama, Satoshi Takeuchi, Deuk Soon Ahn, Hidetada Baba, Sidong Chen, Martha Liliana Cortes, Pieter Doornenbal, Naoki Fukuda, Tadaaki Isobe, Sigeru Kubono, Ian Murray, Hiromi Sato, Yohei Shimizu, Pär-Anders Söderström, Daisuke Suzuki, Hiroyuki Takeda, Koichi Yoshida, Takashi Ichihara, Toshiyuki Kubo,

Meiko Uesaka, Ayano Makinaga, Masafumi Matsushita, Teiichiro Matsuzaki, Satoru Momiyama, Yoshiaki Shiga, Hiroshi Suzuki, Ryo Taniuchi, Yasushi Watanabe, Kathrin Wimmer, Mr. Junki Suwa, Mr. Kazuya Chikaato, Mr. Shunpei Koyama, Mr. Akihiro Hirayama, Mr. Ryohei Hosoda, Mr. Shunsuke Kawakami, Mr. Shoichiro Masuoka, Mr. Ryo Nakajima, Mr. Tomoyuki Ozaki, Ms. Atsumi Saito, Mr. Takeshi Saito, Mr. Yoshiki Soudo, Ms. Xiaohui Sun, Mr. Takato Tomai, Mr. Hiroki Yamada, Mr. Masahiro Yasuda, Ms. Mizuki Shikata, Mr. Junichi Tsubota, and Mr. Tatsuya Yamamoto.

Insightful comments given by Dr. Shinsuke Nakayama (JAEA) has been a great help in discussion related to theoretical models and evaluated nuclear data libraries.

I would like to thank Dr. Shouhei Araki (JAEA) for his valuable comments.

I would like to thank Professor Stephan Pomp, Drs. Alexander Prokofiev, Diego Tarrío, Ali Al-Adili, Mattias Lantz, and Andreas Solders for their great hospitality during my stay in Uppsala University.

Furthermore, I would like to thank all other members studied in the Watanabe-Kin laboratory for their warmhearted helps, especially, Ms. Hikaru Sato, Mr. Seiya Manabe, Mr. Shunsuke Sato, Mr. Kawchar Patwary, Mr. Katsumi Aoki, Mr. Hayato Takeshita, Mr. Junya Kuroda, Mr. Tomohiro Komori, Mr. Keiichirou Shiokawa, Mr. Takumi Mahara, Mr. Kosuke Yoshinami, Ms. Miyuki Uematsu, Mr. Naoya Okamoto, Mr. Yuji Shinjo, Mr. Yu Horai, Mr. Tatsuhiko Miyatake, Mr. Takuya Murota, Mr. Masaya Yamaguchi, Ms. Misaki Saitsu, Mr. Ryohei Takahashi, and Mr. Hiroya Fukuda. My thanks are also given to Ms. Rumiko Koga and Ms. Megumi Ogami for their help about office work.

I would like to thank the accelerator staff of the RIKEN Nishina center for providing high-quality ^{238}U primary beam.

This work was funded by ImPACT Program of Council for Science, Technology and Innovation (Cabinet Office, Government of Japan).

This work was supported by JSPS KAKENHI Grant Number JP18J11378.

Finally, I would like to thank my family and my girlfriend. Without their supports, I could not finish this work.